Nonequilibrium Relaxation and Aging Scaling Properties of the Coulomb Glass and Bose Glass

Matthew T. Shimer

Dissertation submitted to the Faculty of the

Virginia Polytechnic Institute and State University

in partial fulfillment of the requirements for the degree of

Doctor of Philosophy

in

Physics

Uwe Täuber, Chair

Michel Pleimling

Rahul Kulkarni

Hans Robinson

August 26, 2011

Blacksburg, Virginia

Keywords: Aging, Disordered Semiconductors, Coulomb Glass, Bose Glass

Nonequilibrium Relaxation and Aging Scaling Properties of the Coulomb Glass and Bose Glass

Matthew T. Shimer

(ABSTRACT)

We use Monte Carlo simulations in order to investigate the density of states and the two-time density autocorrelation function for the two- and three-dimensional Coulomb glass as well as the Bose glass phase of flux lines in type-II superconductors. We find a very fast forming gap in the density of states and explore the dependence of temperature and filling fraction. By studying two scaling methods, we find that the nonequilibrium relaxation properties can be described sufficiently by a full-aging scaling analysis. The scaling exponents depend on both temperature and filling fraction, and are thus non-universal. We look at the trends of these exponents and found that as either the temperature decreases or the filling fraction deviates more from half-filling, the exponents reflect slower relaxation kinetics. With two separate interaction potentials, a comparison of relaxation rates and the gap in the density of states is made.

This work was supported by the U.S. Department of Energy, Office of Basic Energy Sciences (DOEBES) under grant no. DE-FG02-09ER46613.

Contents

List of Figures

Chapter 1

Introduction

1.1 Background and Motivation

The power of equilibrium statistical mechanics is hard to ignore. The ability for physicists to calculate observables from only a handful of state variables has led to an extraordinary understanding of equilibrium systems. However nice this may be, we live in a world dominated by nonequilibrium systems. Tremendous progress has been made in the area of nonequilibrium statistical mechanics; however, the theoretical foundation is still not fully understood. The description of these nonequilibrium systems beyond the steady state becomes time dependent and, often times, the relaxation from a large perturbation is no longer time translation invariant. With this, interesting relaxation phenomena, such as aging, can occur. Aging (which will be detailed in Chapter 4) in nonequilibrium systems has some enticing

prospects. For one, aging appears to be a universal effect [1]. Aging may also provide a way to classify different systems by looking at how the relaxation rates compare. In order to be able to observe the aging effects, the system has to be undergoing slow relaxation. Disordered systems provide such a situation. The disorder – either from an effective random potential or random spatial disorder – deters the particle transport process, thus slowing down relaxation rates. Often this will lead to a system with many metastable states which further slows the relaxation rate and provides a large window to observe the aging process.

One such nonequilibrium system which provides many intriguing aspects is the disordered semiconductor. Disordered semiconductors near the metal–insulator transition (MIT) have been a subject of theoretical [2–4] and experimental [5, 6] analysis. By looking at disordered systems where the electronic states near the Fermi level, due to strong disorder, are localized (also known as a Coulomb glass), Efros and Shklovskii predicted that a "gap" would form in the density of states near the chemical potential (see Figure 1.1 for an example of the Coulomb gap and Figure 1.2 for an example layout of a Coulomb glass). Research into the non-trivial equilibrium properties [7–14] and non-equilibrium relaxation phenomena [15–24] of the Coulomb glass over the past two decades have considerably advanced our understanding of this paradigmatic model system for highly correlated disordered materials.

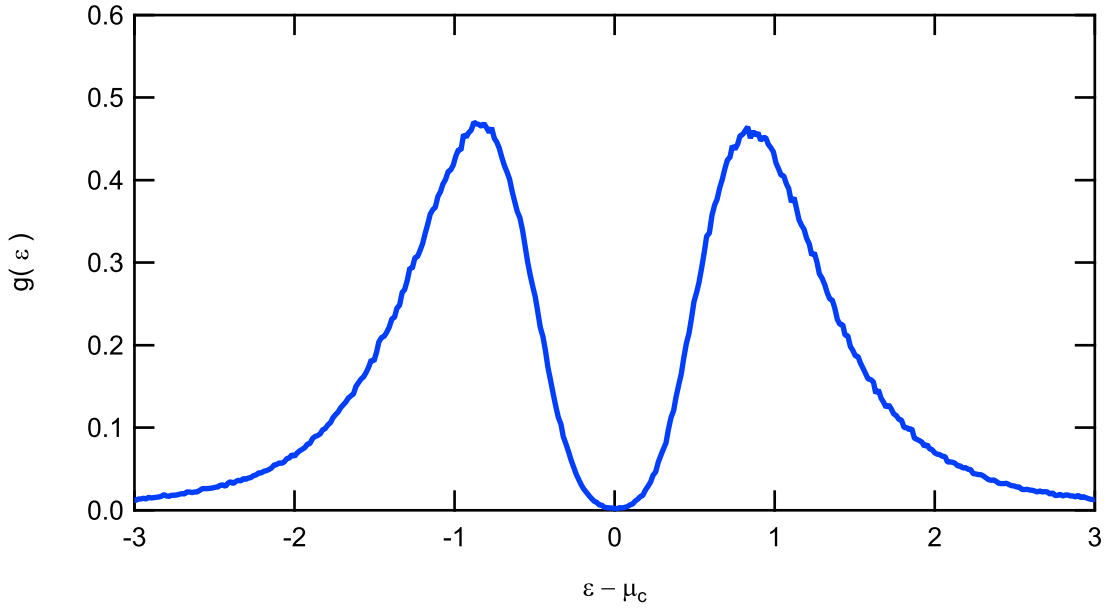

Figure 1.1: Example from our simulations of the Coulomb gap in a three-dimensional Coulomb glass.

1.1.1 Metal–Insulator Transition

The metal–insulator transition (MIT) has been the subject of tremendous research for many years. Mott, in his classic papers [25, 26] investigated how electron correlation affect electron localization. One first considers, Mott argued, a lattice with neutral hydrogen atoms. If the electron wavefunctions overlap, due to the lattice spacing being too small (smaller than the Bohr radius), then in the ground state the $1s$ electron state would be half-filled. This would correspond to a metal at $T = 0$. However, if one instead considers a system where the spacing is larger, or a smaller density, then the electron wavefunctions no longer overlap. This would lead to a finite energy requirement on electron hops (due to electron-electron repulsion), and the system would then be an insulator at $T = 0$. Thus a density dependent

transition from metal to insulator. Anderson showed that disorder can also have an impact on electron localization [27]. Instead of placing the hydrogen atoms from before on a regular lattice, one could randomly distribute the atoms. This would then create an effective random potential and influence the motion of the electrons. The interaction of the electrons plays a vital role in DC and AC hopping conduction.

1.1.2 Coulomb Glass

Efros and Shlovskii proposed a model for the Coulomb glass by thinking of a lightly doped, n-type semiconductor [2–4]. In their model each site could be one of the following: positively charged donors, neutral donors, or negatively charged acceptors. They found that due to spatial disorder within the system, a gap would form in the density of states. The existence of this gap would affect electron transport in the system, effectively lowering the conductivity.

Via Monte Carlo simulations, the Coulomb gap theorized by Efros and Shlovskii was confirmed [7] as well as a possible glass transition [8]. The gap was predicted by Efros and Shlovskii to follow a power law; however, Möbius, Richter, and Drittler measured deviations from the predicted results [10]. By following the temporal creation of the Coulomb gap, it was found that due to electron rearrangement and hopping the production of the gap could involve very long time scales [16]. This creation rate could be further reduced by applying a magnetic field which would impede the electron hopping rate even more [16].

Very intriguing relaxation phenomena were also found [9] in that the single site autocorrela-

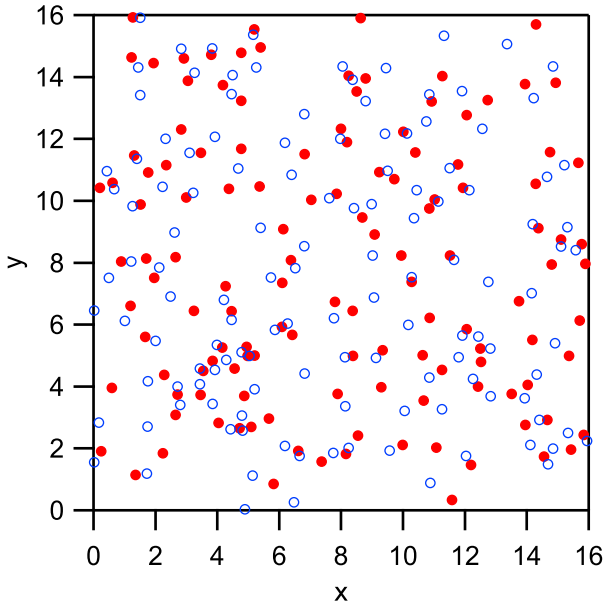

Figure 1.2: An example layout from one of our simulations of a two-dimensional Coulomb glass. The open circles denote unoccupied pinning sites and the filled circles denote occupied sites.

tion function for various temperatures could be scaled onto one master curve. Xue and Lee also noted that there was no unique relaxation time for the system; instead, the relaxation time depended on the temperature [9]. Also, a power-law description of the energy relaxation was measured and found to be independent of temperature, size, and localization radius [15]. Experiments into the relaxation of the conductivity revealed two distinct time scales [18]. Tsigankov, Pazy, Laikhtman, and Efros stated that the short relaxation time scale occurs due to the relaxation of the system within one pseudo-ground state; whereas the long relaxation time scale derives from transitions between different pseudo-ground states [18]. If the system is allowed to proceed for a set time, known as the *waiting time*, before measurements of the autocorrelation function are made, one finds that the autocorrelation function

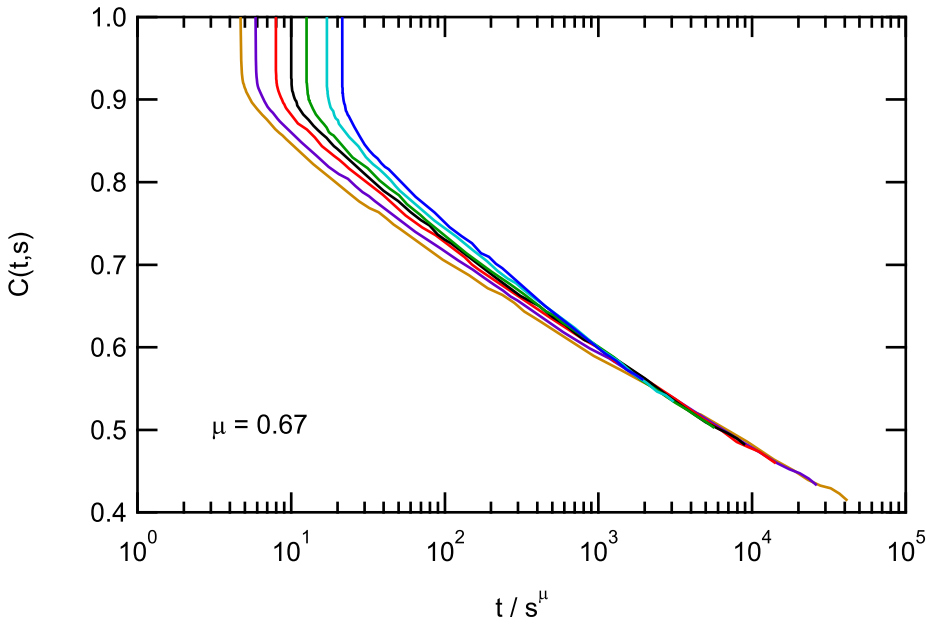

Figure 1.3: An example from our simulations of the scaling of the autocorrelation function for the Coulomb glass. Each line describes a different waiting time, s. From left to right the values of s are 100, 200, 500, 1000, 2000, 5000, and 10000.

for various waiting times can be scaled onto a master curve [19, 20] (see Figure 1.3 as an example). This is an example of dynamical scaling and aging phenomena [1]. This was done by Grempel *et al.* for various temperatures where they found similar scaling behavior for all operating temperatures. Using local mean-field predictions Amir, Oreg, and Imry found the relaxation to be logarithmic in nature with deviations occurring at long time-scales [21–24]. They also found that the system undergoes what is known as full-aging (explained in more detail in Chapter 4); however, with a large enough change in the gate voltage, they found slight deviations from full-aging.

Relaxation measurements for the conductivity of a two-dimensional silicon sample showed

evidence for aging effects [5, 6]. By altering the gate voltage, Jaroszyński and Popovíc were able to force the system out of equilibrium and then measure the resulting relaxation of the conductivity. They found that the relaxation rate depended on the waiting time, a hallmark of aging effects.

1.1.3 Bose Glass

Turning away from semiconductors and looking at type-II superconductors provides some intriguing similarities. When the applied magnetic field is greater than the lower critical field (which depends on the London penetration depth), the field penetrates the superconductor producing flux lines (or vorticies). The flux lines can be moved via the Lorentz force by applying an external current density. This motion creates a parallel electric field which dissipates the power in the system. This means no dissipation-free current flow. However, by pinning the flux lines (suppressing their motion), one can recover dissipation-free current flow. This puts increasing importance on pinning strengths in order to maintain dissipation-free current flow, a technologically crucial property of superconductors.

One way to achieve the pinning of the flux lines is by adding columnar defects to the system. These columnar defects can be introduced to the system by placing columns of nonsuperconducting material into the superconductor. At low enough temperatures (below the "melting" point) the flux lines become pinned to the defects as the structural disorder within the system gives rise to a localization of the flux lines to the defect sites. This *Bose glass* phase is

remarkably similar to the Coulomb glass model [28–32].

One can map the Bose glass to the Coulomb glass by thinking of the flux lines pinned to columnar defects as particles pinned to point defects on a two-dimensional plane. The flux line then becomes the world line of the boson (with the original z-direction mapping to an imaginary time axis). The elasticity constant of the flux line maps to the boson particle mass, the temperature of the Bose glass maps to $\hbar$, and the thickness of the Bose glass maps to $\hbar/T$ (which would result in a finite thickness mapping on to a finite temperature) [30].

The interacting flux lines are able to "reach" out to unoccupied defect sites creating what are known as double kink or double-superkink excitations. A double kink is simply the flux line extending to a neighbor defect site while a double-superkink is when the extension is to a distant pinning site (see Figure 1.4). The flux lines are thus not confined to nearest neighbor hopping. This is analogous to the variable-range hopping transport seen in the Coulomb glass.

Working from this mapping of the Bose glass onto the Coulomb glass, one would expect similar properties. The Bose glass has spatial disorder and long-range interacting "particles", thus it has been found to have a gap form in the density of states [30, 31] (see Figure 1.5 for an example of the "gap" in the density of states for the Bose glass). As can be seen in Figure 1.6, the Bose glass also displays intriguing aging phenomena.

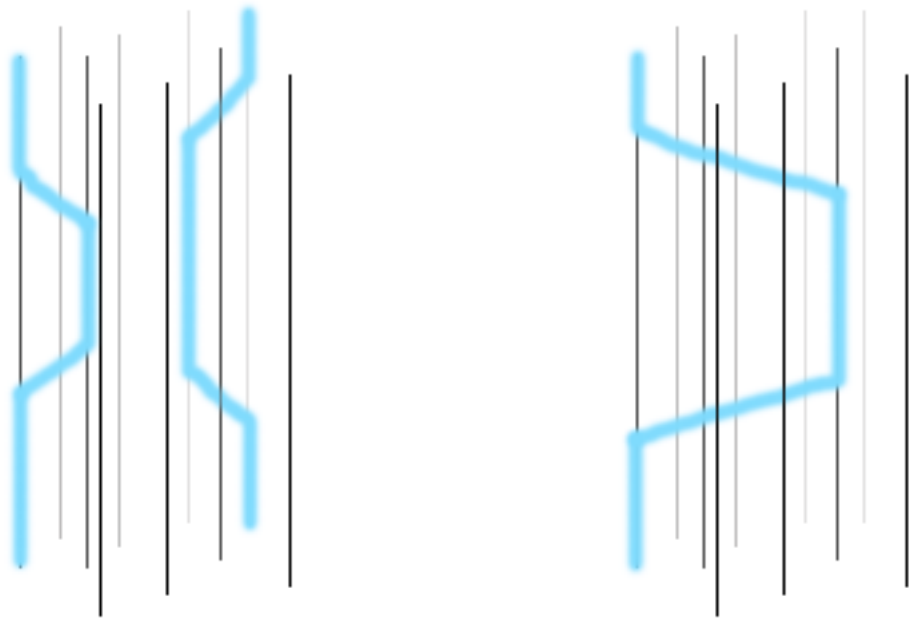

Figure 1.4: Black thin lines represent columnar defects while the thick blue lines represent the flux lines. Left: Doublekink excitation. Right: Double-superkink excitation.

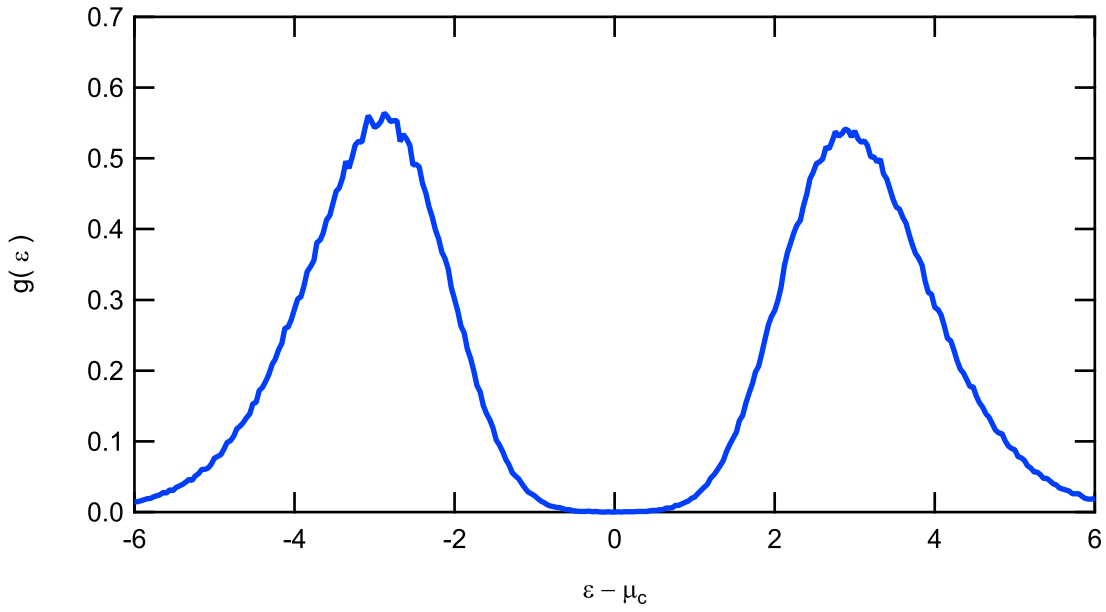

Figure 1.5: Example from our simulations of the "Coulomb gap" in the Bose glass system.

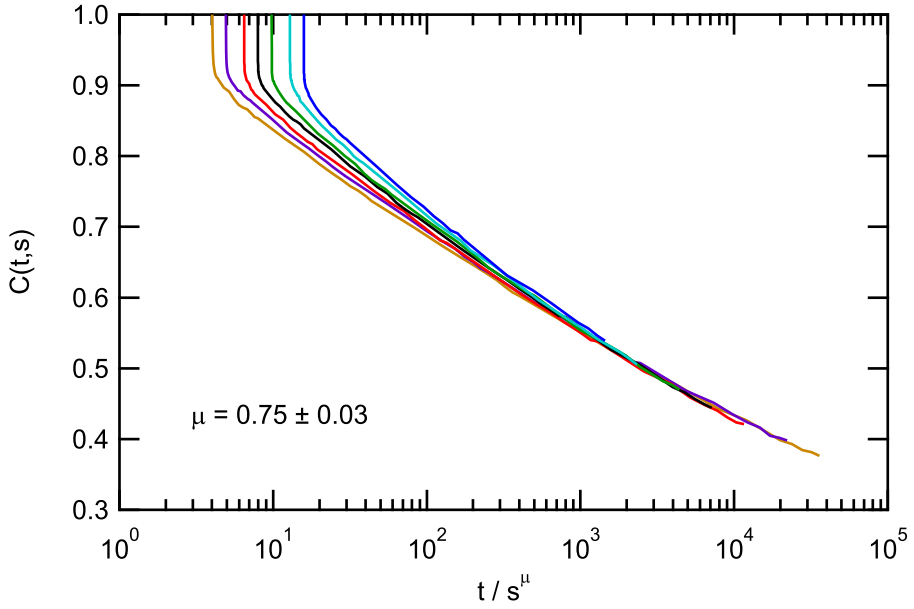

Figure 1.6: An example from our simulations of the scaling of the autocorrelation function for the Bose glass system. Each line describes a different waiting time, s. From left to right the values of s are 100, 200, 500, 1000, 2000, 5000, and 10000.

1.2 Outline

This dissertation will be structured in the following way. In Chapter 2, I will describe the model that we will employ for both the Coulomb glass system as well as the Bose glass phase system. The Monte Carlo algorithm and parameters for the simulations will also be detailed. Chapter 3 will begin with a discussion of the formation of a "gap" in the density of states of these systems. An investigation into a possible power law description of the gap will then follow. I will then show the measurements of the speed of formation of the gap. Chapter 4 deals with aging kinetics and scaling forms of the two-time carrier density autocorrelation function. I will detail the two scaling forms that we used as well as the method to measure the scaling exponents. The results of the simulations will be given in Chapter 5.

Chapter 2

Model and Simulations

In Section 2.1, I will describe the Coulomb glass model that we employ, first introduced by Efros and Shklovskii [3]. A Monte Carlo algorithm was used to simulate the relaxation kinetics of this model. The algorithm will be detailed in Section 2.2 and the parameters of these simulations will be given in Section 2.3. The Coulomb glass model can be adapted to describe a Bose glass phase of magnetic flux lines in type-II superconductors that are pinned to columnar defects by essentially replacing the Coulomb potential with a logarithmic repulsion, as explained in Section 2.4.

2.1 Coulomb Glass Model

The Coulomb glass model introduced by Efros and Shklovskii [3] consists of multiple localized pinning sites available to the charge carriers. Because of the strong intra-site correlations

these sites can only contain a single charge carrier at most. The system is dominated by long-range repulsive Coulomb interactions $V(r) \sim 1/r$ and the spatial disorder is induced by the randomly located available sites. Our model does not have these sites on a lattice, but rather on a continuum. The Hamiltonian of the Coulomb glass model reads [2–4]

$$H = \sum_i n_i \varphi_i + \frac{e^2}{2\kappa} \sum_{i \neq j} \frac{(n_i - K)(n_j - K)}{|\mathbf{R}_i - \mathbf{R}_j|} \,, \tag{2.1}$$

where e is the electron charge, κ is the dielectric constant, and where $\mathbf{R}_i$, φ_i, and n_i respectively denote the position vector, (bare) site energy, and occupancy of the ith site, $i = 1, \ldots, N$. The occupancy n_i can only take on the values 0 or 1. The first term corresponds to (random) site energies assigned to each accessible location; since the system is dominated by the long-range forces, we chose $\varphi_i = 0$ to further simplify the model, while still allowing the positions $\mathbf{R}_i$ to be continuous and random [9, 16, 19, 20]. (Alternatively, one could allow φ_i to take on random values while the positions $\mathbf{R}_i$ would be discrete and set on a lattice.) The second contribution encapsulates the repulsive Coulomb interactions (with dielectric constant κ).

In order to maintain global charge neutrality, a uniform relative charge density K is inserted;

$$K = \sum_i \frac{n_i}{N} \,. \tag{2.2}$$

K can also be described as the total carrier density per site, or filling fraction. We note that with $\varphi_i = 0$ the Hamiltonian (2.1) displays particle–hole symmetry, i.e., systems with

$K = 0.5 + k$ and $K = 0.5 - k$ are equivalent.

Upon replacing the occupation numbers with spin variables $\sigma_i = 2n_i - 1 = \pm 1$, one sees that the Coulomb glass maps onto a random-site random-field antiferromagnetic Ising model with long-range exchange interactions [7].

A snapshot of a particular simulation cell of a two-dimensional Coulomb glass can be seen in Figure 2.1. In this snap shot the filled circles are occupied sites, while open circles are empty sites. Because of periodic boundary conditions, this cell is mirrored on each side.

2.2 Monte Carlo Algorithm

The Monte Carlo simulations were initiated by randomly placing sites within a square (cube in three dimensions). We simulate the initial high temperature quench by preparing the system in a completely random initial condition. The charge carriers can then attempt hops to unoccupied sites — say from occupied site a to unoccupied site b. Two factors determine the success rate of this hop, namely a strongly distance-dependent tunneling process (in semiconductors mediated through phonons) and thermally activated jumps over energy barriers [19], i.e.,

$$\Gamma_{a\to b} = \tau_0^{-1} e^{-2R_{ab}/\xi} \min[1, e^{-\Delta E_{ab}/T}], \tag{2.3}$$

where τ_0 represents a microscopic time scale, $R_{ab} = |\mathbf{R}_a - \mathbf{R}_b|$ is the distance between sites

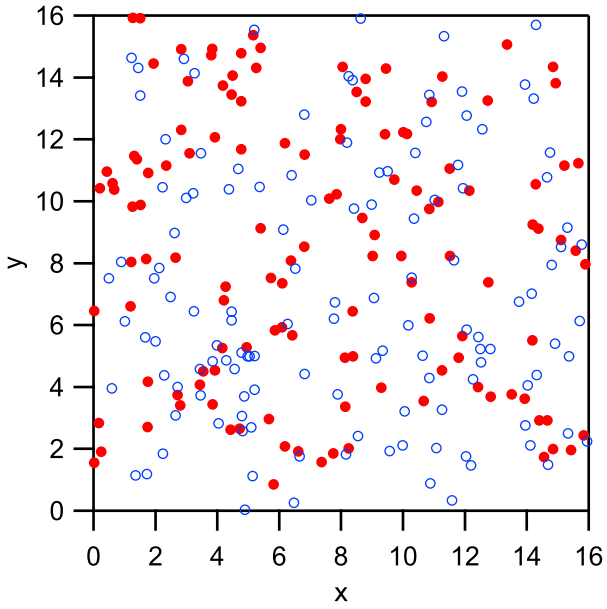

(a)

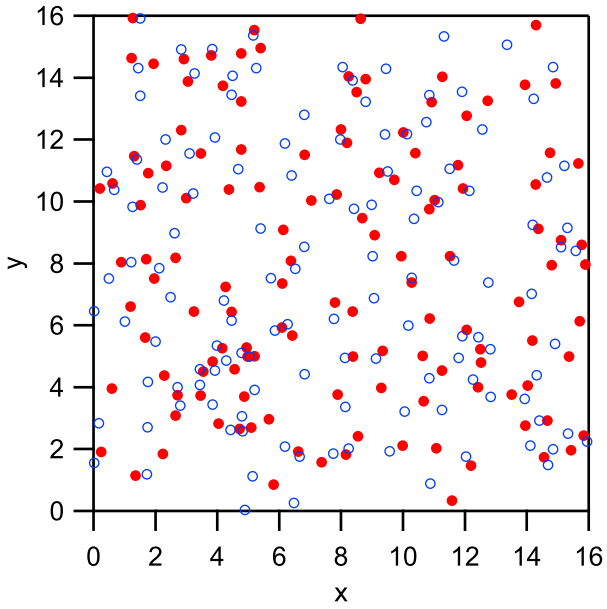

(b)

Figure 2.1: An example of the simulation cell of a two-dimensional Coulomb glass with $K = 0.5$. The red, filled circles represent occupied sites; while the blue, open circles represent unoccupied sites. (a) is a snapshot of the initial conditions. (b) is a snapshot after 10^6 Monte Carlo steps.

a and b, ξ characterizes the spatial extension of the localized carrier wave functions, and we have set $k_B = 1$. The first, spatially exponential term in (2.3) is derived from quantum tunneling, while the second exponential term is due to thermodynamics: A thermally activated hop from sites a to b entails the energy difference

$$\Delta E_{ab} = \epsilon_b - \epsilon_a - \frac{e^2}{\kappa R_{ab}}\,, \tag{2.4}$$

with the (interacting) site energies

$$\epsilon_a = \frac{e^2}{\kappa} \sum_{b \neq a} \frac{n_b - K}{R_{ab}}\,. \tag{2.5}$$

Each Monte Carlo time-step (MCS) consists of the following:

1. Choose a random occupied site a.

2. Choose an unoccupied site b from the probability distribution given by the tunneling term in equation (2.3).

3. Attempt a hop with a probability of success given by the Metropolis term in equation (2.3). If hop attempt fails, return to step one.

4. Move charge carrier from site a to site b.

Notice that there is no step to recalculate the pair potentials. This is due to the fact that all possible pair potentials are calculated at the very beginning of the simulation run. Only

the site energies of sites a and b need to be calculated — and this only requires a summation of the pre-calculated pair potentials, see equation (2.5). Through the calculation of these interacting site energies, we are able to measure the evolution of the density of states. This will be further discussed in Chapter 3. Also, with all the occupation numbers, n_i, known, the two-time carrier density autocorrelation can be measured (see Chapter 4).

We also explored a slightly different protocol where we would add or remove charge carriers from the system as an additional perturbation. This was done in two ways: randomly adding/removing the charge carriers or by removing the charge carriers from left to right. This was an attempt to model the experiments closer. In order to math up with experiments, we tried to measure the conductivity in the system with the aforementioned protocol. This was done by applying an electric field and measuring the motion of the charge carriers; however, this did not work out. The system seemed to be too sensitive to the electric field in that the system either behaved as if there was no electric field (no current in the system) or a very large current where the system had no dependence on temperature or filling fraction. We could not find a middle ground which would allow us to effectively measure the conductivity and more research would need to be done.

2.3 Simulation Parameters

In the following, distances are measured relative to the average separation between sites a_0, and energies as well as temperature scales are measured relative to the typical Coulomb

energy $E_C = e^2/\kappa a_0$ [19]. We set the spatial extension of the localized wave functions, ξ, to a_0, as in Refs. [19, 20]. We have explored other values for ξ as well – between $0.5a_0$ and $2a_0$, and (within the applicability range of the model) found the ensuing results to simply scale with τ_0; hence $\xi = a_0$ was chosen for simplification.

We performed simulations for systems with $8 \leq L \leq 32$; with temperatures in the range of $0.01 \leq T \leq 0.1$; and carrier densities in the range of $0.25 \leq K \leq 0.5$ (also equivalent to $0.5 \leq K \leq 0.75$ due to particle–hole symmetry). Running the simulations with various system sizes L, we noticed no measurable finite-size effects (see Figure 2.2). Temperatures larger than 0.03 turned out not to be useful for our study of aging processes since equilibrium was then reached far too quickly. In contrast, for $T < 0.01$, the kinetics slowed down too much for gathering statistically significant data within computationally reasonable time frames. As will be discussed in more detail below, the dynamics also freezes out within the numerically accessible simulation times for $K < 0.4$ (or $K > 0.6$).

Periodic boundary conditions were used and the potential due to charges outside the cell was calculated by mirroring the simulation cell on each side. The charge carriers were initially placed randomly at available sites to mimic a quench from very high temperatures. Then the system was evolved at temperature T with the dynamics described by the generalized Metropolis rate (2.3).

For each simulation configuration (length, filling fraction, etc.) 1000 - 3000 simulation runs were completed. A typical simulation run took anywhere from 6 hours to 20 hours to complete depending on the length and number of dimensions.

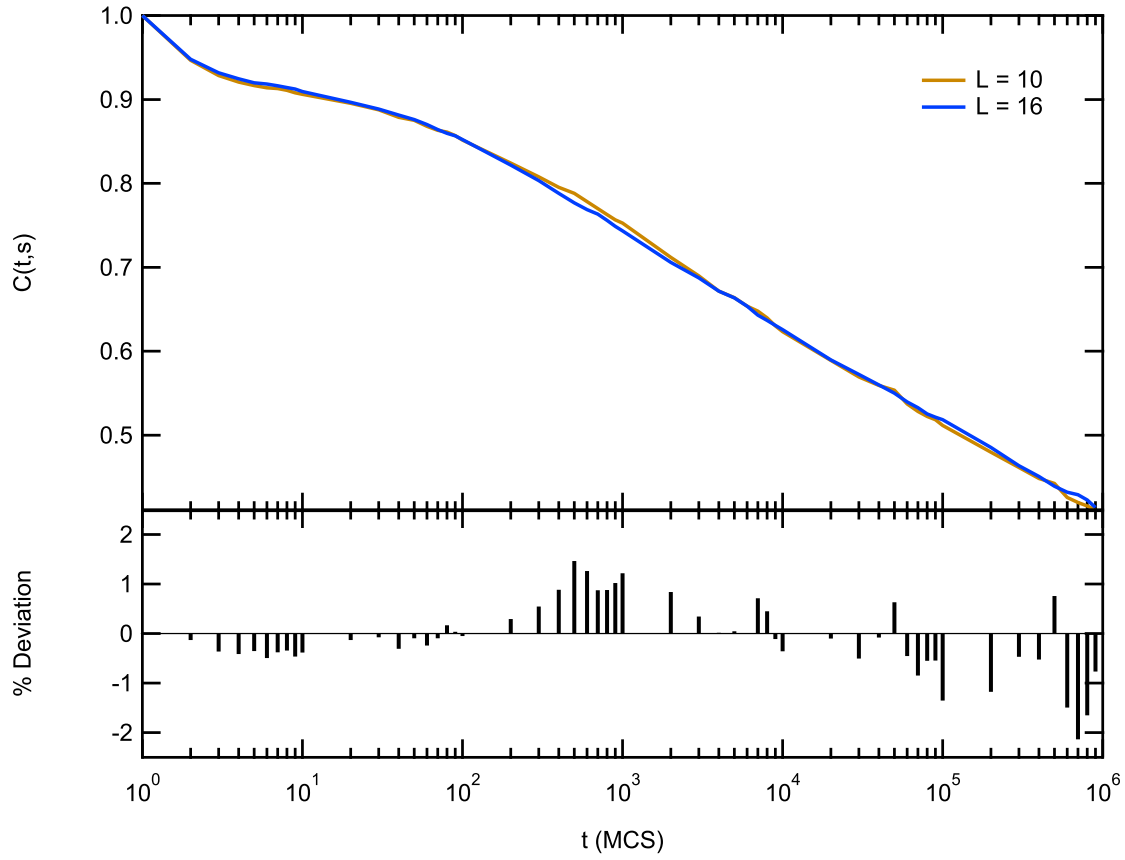

Figure 2.2: A comparison between two different simulation lengths. The top graph shows the autocorrelation function for systems of $L = 10$ and $L = 16$. The bottom graph shows the percent that the system with $L = 10$ deviates from the system with $L = 16$.

2.4 Adaptation for Logarithmic Potential

In order to adapt our Coulomb glass model to the Bose glass model, we start with the two-dimensional Coulomb glass model described above. Instead of charge-carriers occupying pinning sites, the Bose glass model consists of magnetic flux lines pinned to columnar defects. The simulation cell then becomes a cross-section of the superconductor where the pinning sites are just the location of the intersection of this "slice" and the defect. The interaction potential, $V(r)$, no longer being the Coulomb interaction$(1/r)$, becomes a screened logarithmic potential, i.e. [31]

$$V(r) = 2\epsilon_0 K_0(r/\lambda)\,, \tag{2.6}$$

where $K_0(r/\lambda)$ is the modified Bessel function – $K_0(x) \propto -ln(x)$ as $x \to 0$ and $K_0(x) \propto x^{-1/2}e^{-x}$ as $x \to \infty$ – and λ defines the interaction range. The Hamiltonian of this model is effectively the same as the Coulomb glass model, i.e. [31]

$$H = \sum_i n_i\varphi_i + \frac{1}{2}\sum_{i\neq j} n_i n_j V(r_{ij})\,, \tag{2.7}$$

where, as before, n_i represents the occupation number, φ_i is the random site energy (which is again set to zero), and $V(r)$ is the interaction potential defined in equation (2.6). No changes are made to the Monte Carlo algorithm for this model.

Chapter 3

Coulomb Gap

In thermal equilibrium, long-range Coulomb interactions and spatial disorder within the system create a soft gap in the (interacting) density of states (DOS), $g(\epsilon)$, as famously first noted by Efros and Shklovskii [3]. The suppression of availability of states with energies near the chemical potential, μ_c, separates occupied and unoccupied energy levels at $T = 0$. This gap plays an important role in electron transport of disordered semiconductors and vortex transport of type-II superconductors in the Bose glass phase, namely the temperature dependence on conductivity in the variable range hopping regime [4]. The existence of the Coulomb gap, or a non-constant DOS, means the system is no longer described by Mott variable range hopping. Due to this modification to the DOS, the conductivity is on the order of $\exp(-T^{-1/2})$, instead of Mott's $\exp(-T^{-1/3})$ or $\exp(-T^{-1/4})$ for two or three dimensions respectively [4, 33] — an overall lowering of the conductivity. These effects, as well as the Coulomb gap itself, have been directly observed experimentally in nonmetallic doped

semiconductors in both two- [34] and three dimensions [35].

Via Monte Carlo simulations, we studied the emergence of and the shape of the Coulomb gap under various interacting potentials, temperatures, filling fractions, and dimensions. In Section 3.1, I will summarize the arguments given by Efros and Shklovskii [3] for the formation of the Coulomb gap. Mean field calculations predict that the shape of the DOS around the chemical potential should follow a power law, linear for two dimensions and parabolic for three dimensions. This will be discussed in Section 3.2 along with some of our results for the validity of the mean field claim of a power law. These simulations allowed us to also measure the formation of the Coulomb gap over time. Section 3.3 will show the remarkable speed by which the Coulomb gap forms. The Coulomb gap is not limited to just Coulomb interactions, it also exists for our logarithmic potential model. We found a very broad Coulomb gap in the Bose glass model which also displayed a power law-like decay near the chemical potential, illustrated in Section 3.4.

3.1 Gap Formation

The following is a self-consistency argument for the suppression of the density of states at the chemical potential, first proposed by Efros and Shklovskii [3].

Begin with a system in equilibrium at $T = 0$. The energy required for a charge carrier to hop from site a to site b is given by

$$\Delta E_{ab} = \epsilon_b - \epsilon_a - \frac{1}{R_{ab}} > 0\,, \tag{3.1}$$

where ϵ_i is the energy of a charge carrier at site i and R_{ab} is the distance between sites a and b. This energy difference, ΔE_{ab}, must be positive as the system is in equilibrium.

Now, assume the DOS at the chemical potential, $g(\mu_c)$, is finite. Let us also only look at the site energies within an interval of ϵ around the chemical potential; or, more specifically, $\epsilon_b - \epsilon_a < 2\epsilon$. The number of sites within this interval is

$$N = 2\epsilon g(\mu_c)\,. \tag{3.2}$$

If we then choose two nearby sites, one occupied and one unoccupied (still within the same energy interval), with a separation on the order of $R_{ab} \sim (N/V)^{-1/d}$, the energy inequality in (3.1) becomes

$$\epsilon_b - \epsilon_a - A\left(\frac{\epsilon g(\mu_c)}{V}\right)^{1/d} > 0\,, \tag{3.3}$$

where d is the dimensionality of the system and A is a constant of proportionality. This can be further reduced by recalling the fact that $\epsilon_b - \epsilon_a < 2\epsilon$. The inequality then reads

$$A\left(\frac{\epsilon g(\mu_c)}{V}\right)^{1/d} < 2\epsilon\,. \tag{3.4}$$

One must remember that ϵ is an arbitrary number, thus (3.4) can be violated with a small

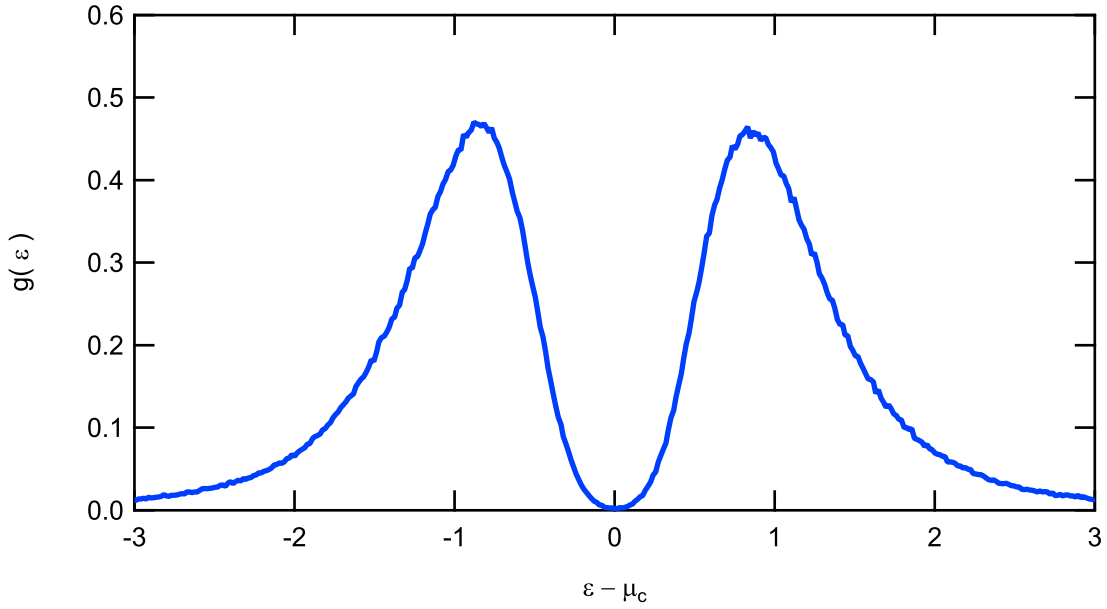

Figure 3.1: Example from our simulations of the Coulomb gap in a three-dimensional Coulomb glass ($L = 8$, $N = 512$ sites) at temperature $T = 0.02$.

enough value for ϵ. The only assumption made was that of a finite DOS at the chemical potential, $g(\mu_c)$. This contradiction means that $g(\mu_c)$ must be suppressed and a gap is formed in the DOS. An example of the Coulomb gap can be seen in Figure 3.1.

The above argument for the suppression of $g(\mu_c)$ assumes both equilibrium and $T = 0$, neither of which is true in the systems that we studied. However, as will be discussed in §3.3, the Coulomb gap becomes well-established very rapidly. So, even though thermal equilibrium has not yet been reached, the gap is still very pronounced. Deviating away from the zero temperature limit has the effect of "washing out" — or a reduction in the suppression of — the Coulomb gap, as illustrated in Figure 3.2, which shows the DOS under different operating temperatures. As can be seen, after the temperature becomes high enough, on the order

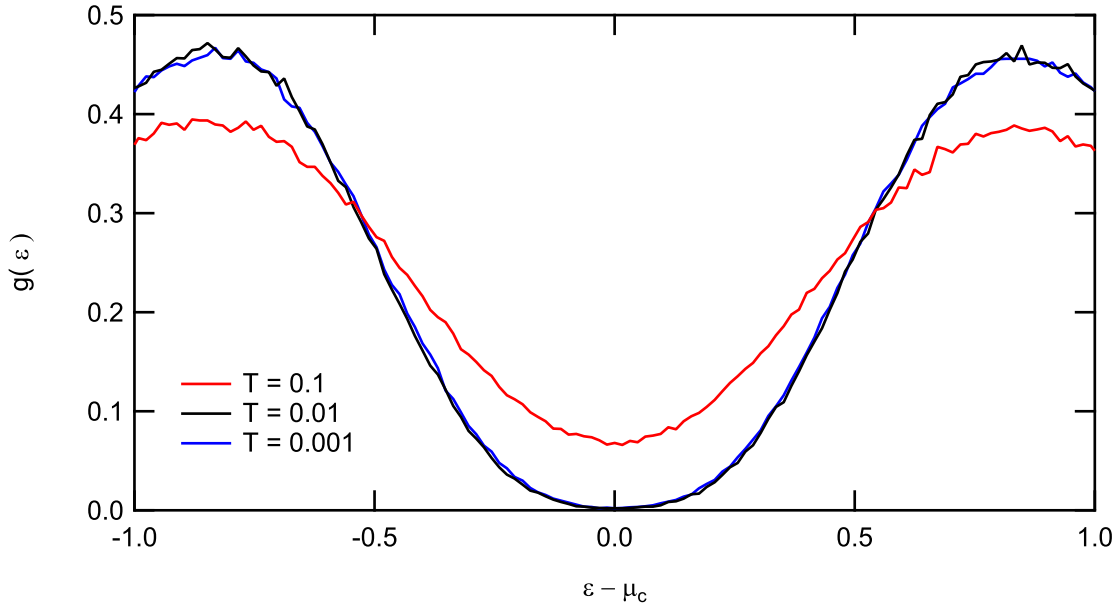

Figure 3.2: Density of states for various operating temperatures. Three-dimensional Coulomb glass with $L = 8$ and $N = 512$ sites.

of the width of the gap, the states around the chemical potential become accessible. If the gap, however, is broad enough, one would need a very high temperature before this effect is noticed; as is the case for the Bose glass model in §3.4, where the highest of the temperatures that we probed had no measurable effect on the Coulomb gap.

3.2 Gap Exponent

The Coulomb gap can be described further by investigating the asymptotic behavior of the density of states near the chemical potential ($\epsilon \to \mu_c$). As the energy approaches the chemical potential the DOS appears to diminish via a power law $g(\epsilon) \sim |\epsilon - \mu_c|^s$ [2–4, 7–14]. This

can be seen by the following mean field argument [4, 31]:

If, instead of limiting ourselves to the Coulomb potential, we assume an arbitrary potential $\Phi(R_{ab})$, then equation (3.1) becomes

$$\Delta E_{ab} = \epsilon_b - \epsilon_a - \Phi(R_{ab}) > 0\,. \tag{3.5}$$

As before, we only consider sites within an energy interval of ϵ around the chemical potential which implies $\Phi(R_{ab}) < \epsilon_b - \epsilon_a < 2\epsilon$. Energetically favorable hops would then occur over a distance

$$R_{ab} \propto \tilde{\Phi}(\epsilon)\,, \tag{3.6}$$

where $\tilde{\Phi}(\epsilon)$ is the inverse of the potential function. The number of sites that are energetically favorable would then be given by $(N/V) = n \propto {R_{ab}}^{-d}$, where d is the dimensionality of the system, as before. Because ϵ is small, we can derive an expression for the density of states by evaluating $g(\epsilon) \propto dn/d\epsilon$. This leads to the expression

$$g(\epsilon) = A\,\frac{|\tilde{\Phi}'(x)|}{\tilde{\Phi}(x)^{d+1}}\bigg|_{x=\epsilon}\,, \tag{3.7}$$

where A is a constant of proportionality (as well as any constants from the derivative). For a system with long-range repulsive potential $\Phi(R_{ab}) \sim 1/{r_{ab}}^{\sigma}$, equation (3.7) offers a value for the gap exponent, s, given by

$$s = \left(\frac{d}{\sigma}\right) - 1\,. \tag{3.8}$$

This gap exponent, s, alters the temperature dependence of the conductivity and variable range hopping length of the system. In three dimensions, the conductivity is on the order of $\exp(-T^{-p})$ where $p = (s+1)/(s+4)$ [4, 33]. For a constant DOS, $s = 0$, one recovers Mott's variable range hopping exponent of $p = 1/4$. However, equation (3.8) would give a larger value of $p = 1/2$. This would correspond to a lower conductivity in the system. Similarly, for two dimensions, equation (3.8) would also give a value of $p = 1/2$ which, again, is larger then Mott's predicted $p = 1/3$.

We investigated the asymptotic behavior of the Coulomb gap in both two- and three dimensions under differing operating temperatures and filling fractions. Figure 3.3 shows that the DOS does appear to follow a power law; however, there also appears to be deviations as the energy approaches the chemical potential.

The value of s was measured under different temperatures within the range $0.001 \leq T \leq 0.1$. These results are displayed in Figure 3.4 for both two-, (a), and three dimensions, (b). The dashed line shows the value of s as predicted by equation (3.8). Changing the filling fraction has the effect of "shifting" the DOS — the peak on the left, or the occupied sites, reduces in size while the opposite peak raises. This is shown in Figure 3.5. However, there appears to be no significant change to the gap exponent, s (Figure 3.6), at least for the filling fraction range that we studied.

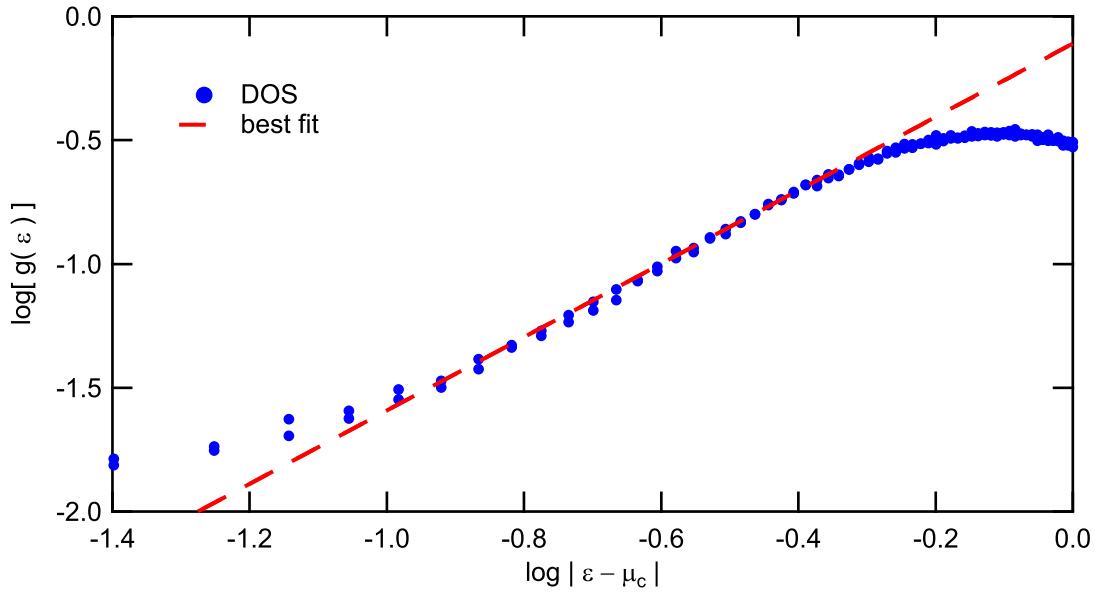

(a)

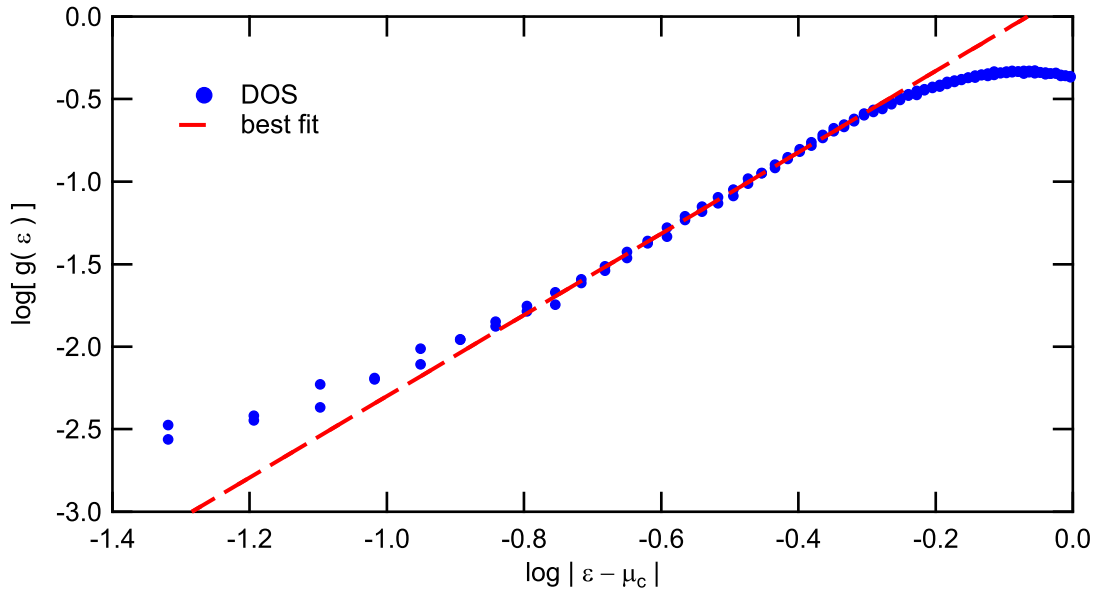

(b)

Figure 3.3: Logarithmic plot of the density of states. The dashed line represents the best power law fit. (a) $d = 2$, $L = 16$, $N = 256$ sites, $K = 0.5$, and $T = 0.02$. (b) $d = 3$, $L = 8$, $N = 512$ sites, $K = 0.5$, and $T = 0.02$.

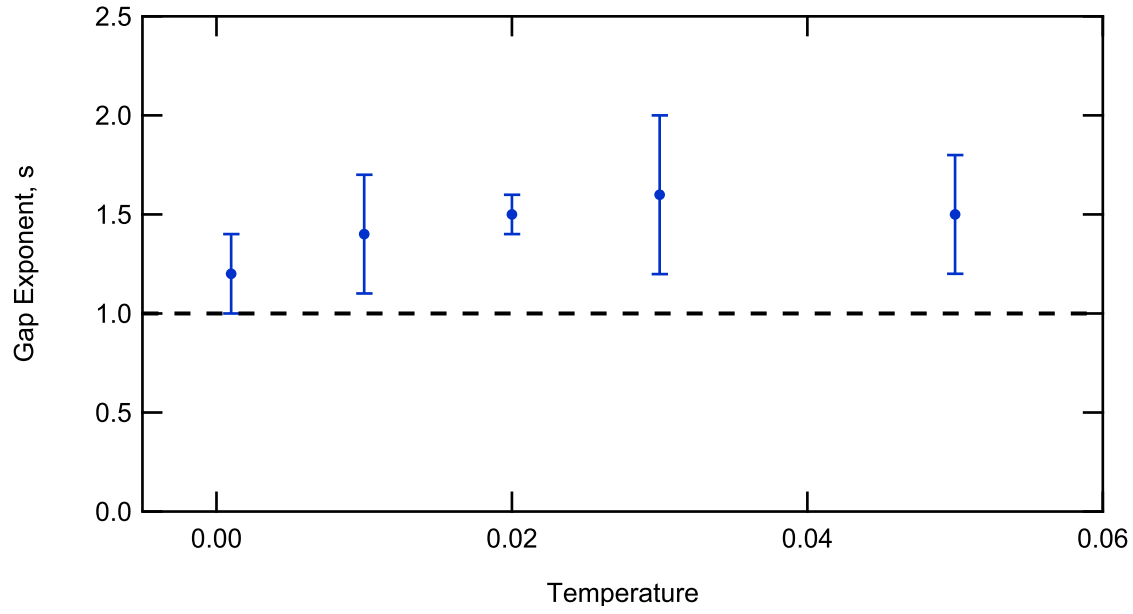

(a)

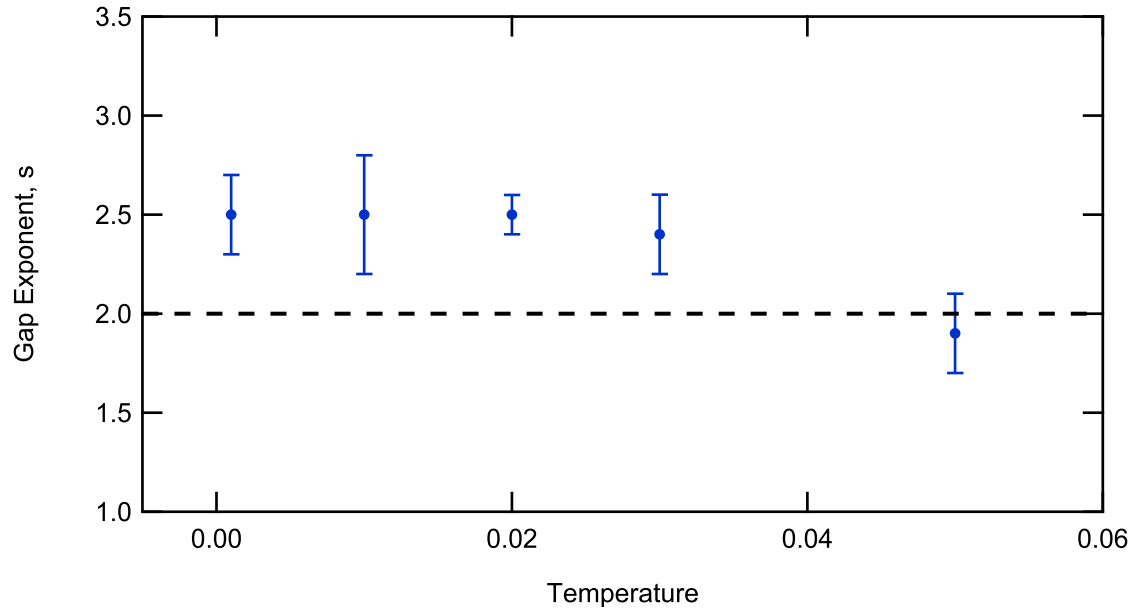

(b)

Figure 3.4: Values for the gap exponent, s, for different operating temperatures. The dashed line is for $s = d - 1$, the value that mean field predicts. (a) $d = 2$, $L = 16$, and $N = 256$ sites. (b) $d = 3$, $L = 8$, and $N = 512$ sites.

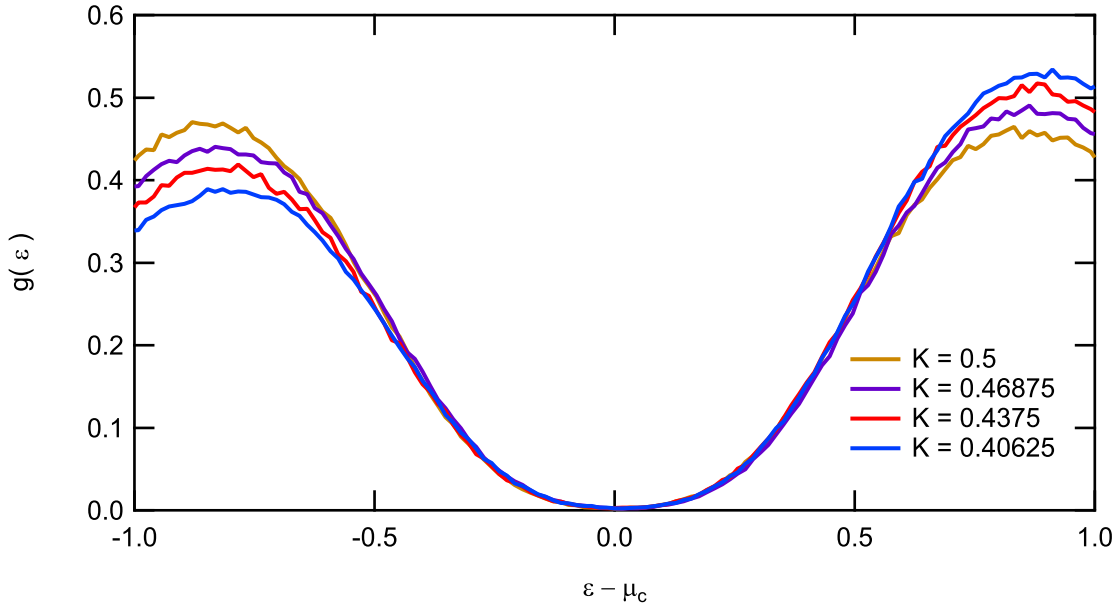

Figure 3.5: Density of states for various filling fractions. Three-dimensional Coulomb glass with $L = 8$, $N = 512$ sites, and $T = 0.02$.

The previous argument leading to equation (3.8) has multiple assumptions built in. One such assumption is of single-particle hops, where multi-particle hops may play an important role in transport. Also, it considered all sites within the interval ϵ were distributed evenly, whereas the sites actually cluster [7]. For these reasons, it is not surprising that the values of s differ from those predicted by the mean field arguments. Previous studies of the Coulomb gap [7, 10] also saw deviations from the mean field values. For the three-dimensional system (where mean field theory predicts $s = 2$), Möbius, Richter, and Drittler [10] found $s \approx 2.6$; while Massey and Lee [35] experimentally found $s \approx 2.2$. Our value of $s \approx 2.5$ agrees quite well with these previous authors. The disagreement with the values of s also have an impact on the predictions for the variable range hopping exponent p. The analytical theory offered

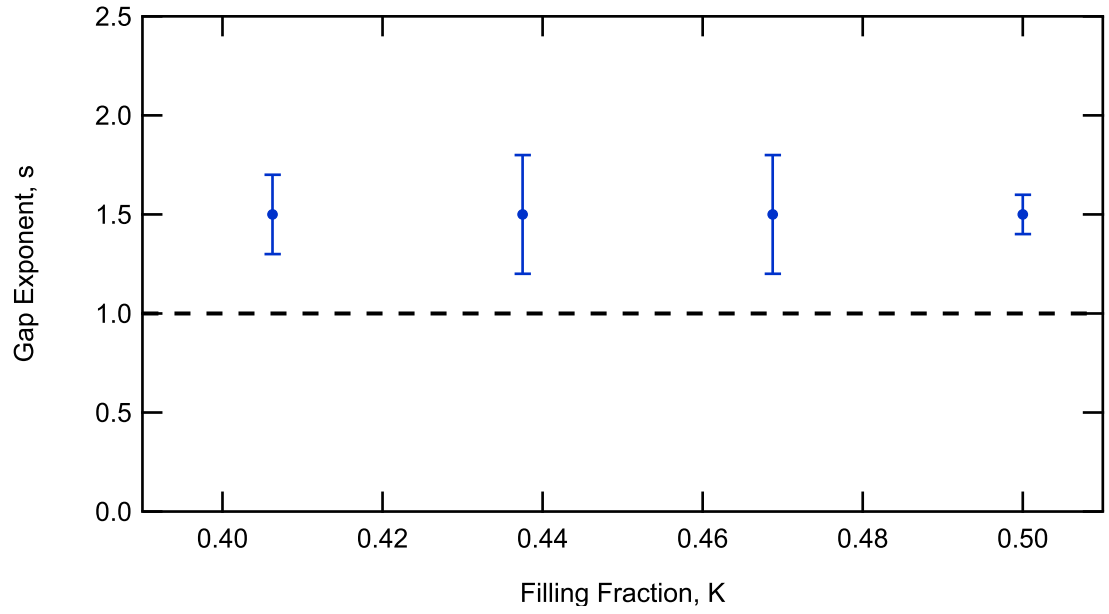

(a)

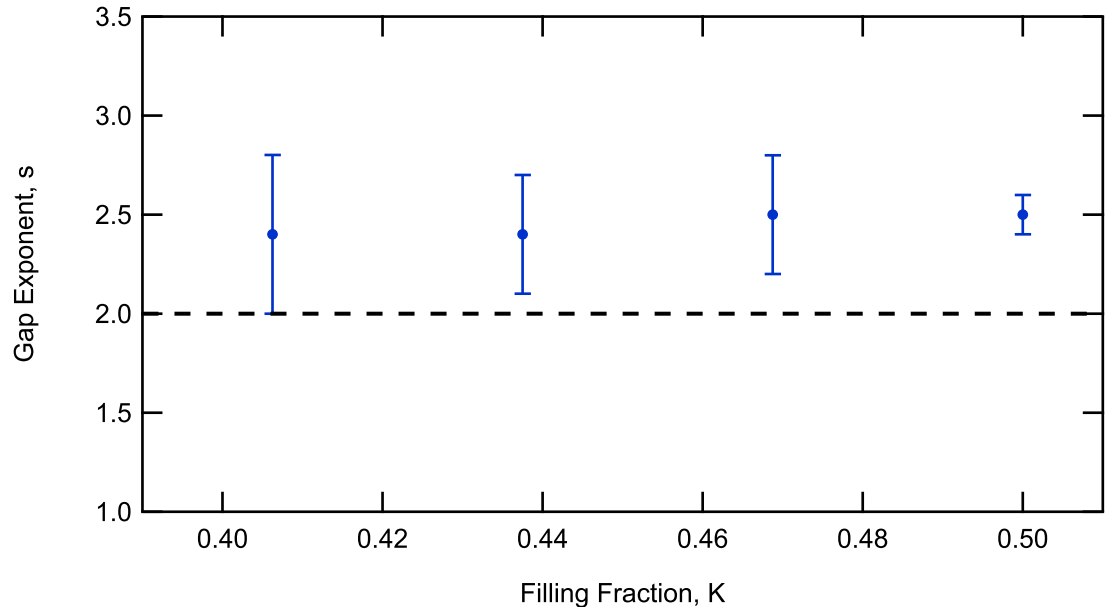

(b)

Figure 3.6: Values for the gap exponent, s, for different filling fractions at $T = 0.02$. The dashed line is for $s = d - 1$, the value that mean field predicts. (a) $d = 2$, $L = 16$, and $N = 256$ sites. (b) $d = 3$, $L = 8$, and $N = 512$ sites.

above would give a value of $p = 1/2$ for both two- and three dimensions; however, Möbius, Richter, and Drittler [10] found a measurable difference for the values of p (our system was not large enough to see a measurable difference).

A power law may not even be the best description for the DOS near the chemical potential. With the system sizes in use here, it becomes increasingly difficult to study the behavior of the DOS near the chemical potential due to the small number of sites. One would most likely need a much larger system to completely explore this energy regime. Even with very large systems — such as in Ref [10] which had system sizes up to 125,000 sites — deviations from the mean field estimates and from the power law fit persist. However, for our system sizes, a power law appears to be a fair description of the shape of the DOS near the chemical potential. Experimental results [34, 35] have also seen the power law to be a reasonable fit.

3.3 Formation Speed

We monitored the density of states over time and found the Coulomb gap forms remarkably fast, as seen in Figure 3.7. The Coulomb gap in three dimensions is already quite pronounced after around 10 Monte Carlo time steps (MCS) and clearly established after as few as 100 MCS. This rapid formation of the gap is important to note since later discussions will be dealing with time periods far exceeding 100 MCS as we will be looking at the slow decay of local density correlations.

Temperature does not appear to have much of an impact on how quickly the Coulomb gap

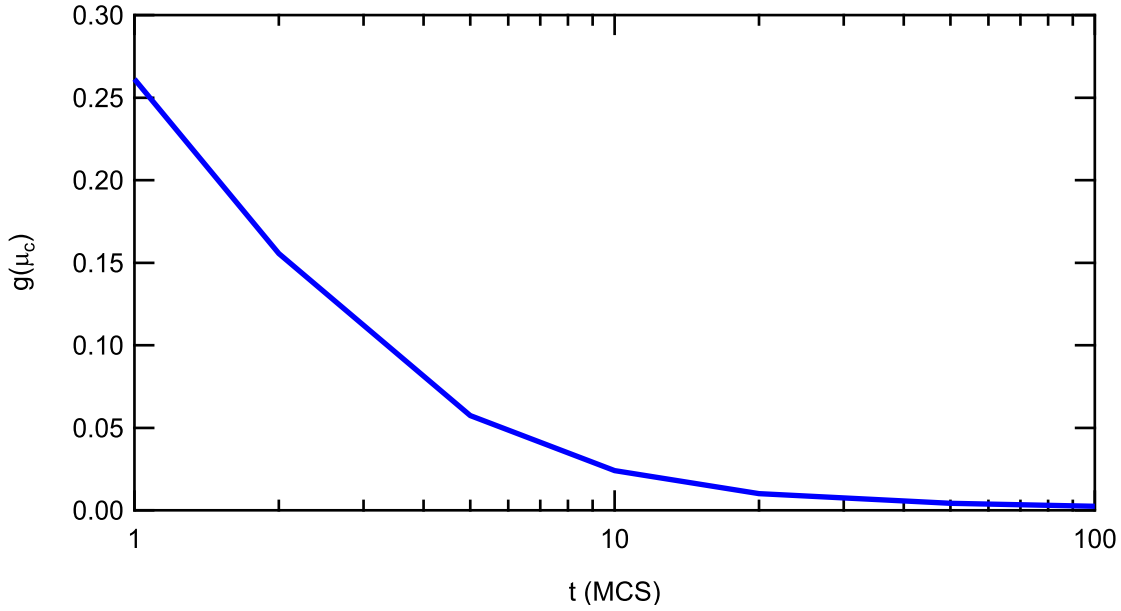

Figure 3.7: Coulomb gap formation over time in a three-dimensional Coulomb glass. The plot shows how quickly $g(\mu_c)$ gets suppressed. $L = 8$, $N = 512$ sites, and $T = 0.02$.

forms as evident in Figure 3.8. The higher temperature system reaches a steady value for $g(\mu_c)$ at around 20 MCS, the same as the lower temperature systems. The only difference is that the value of $g(\mu_c)$ is higher, as expected (see §3.1).

The Coulomb gap forms much quicker in three dimensions as illustrated in Figure 3.9. It should also be noted that it appears, for the three-dimensional case, there is complete suppression of the DOS at the chemical potential, $g(\mu_c) = 0$, within the time scales we measured, even at non-zero temperatures. This does not seem to be true in two dimensions as our temperatures are probably too high to see a complete suppression.

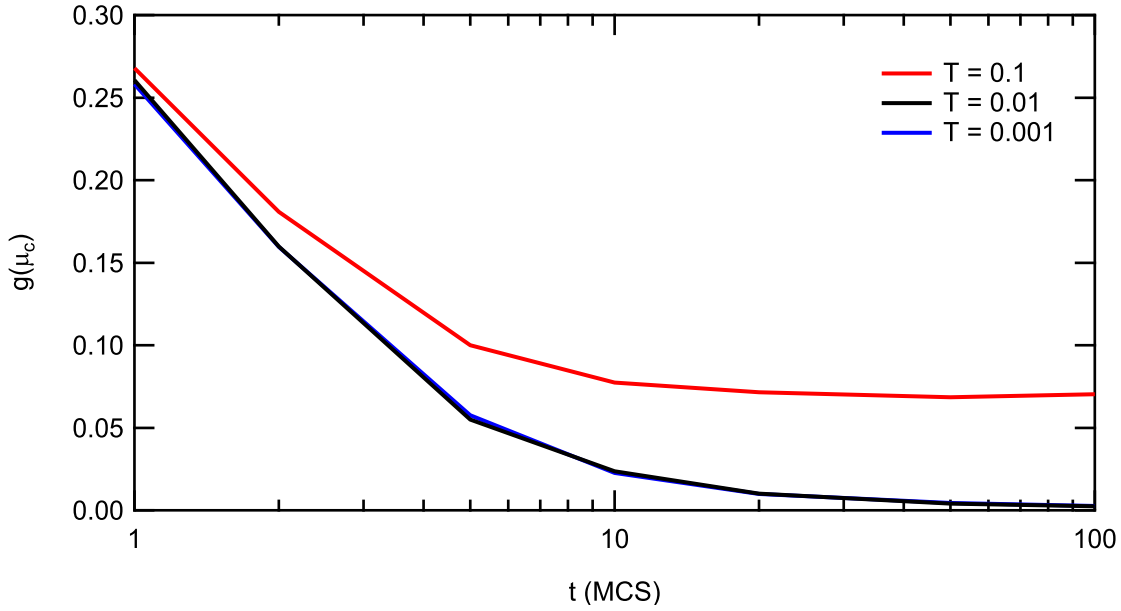

Figure 3.8: Coulomb gap formation over time with different operating temperatures. $d = 3$, $L = 8$, and $N = 512$ sites.

3.4 Bose glass

For a system subject to a logarithmic interaction potential, equation (3.7) predicts the density of states should also display a gap. In fact, the Coulomb gap formed is remarkably broad, as evident in Figure 3.10.

Comparing the speed of gap formation between the two interaction potentials — Coulomb potential and logarithmic potential — displays how much faster the gap forms in the Bose glass (Figure 3.11). It is important to note, however, that due to the two different forms of potential, the two systems are not on the same energy scale. This means that a true quantitative comparison would be very difficult.

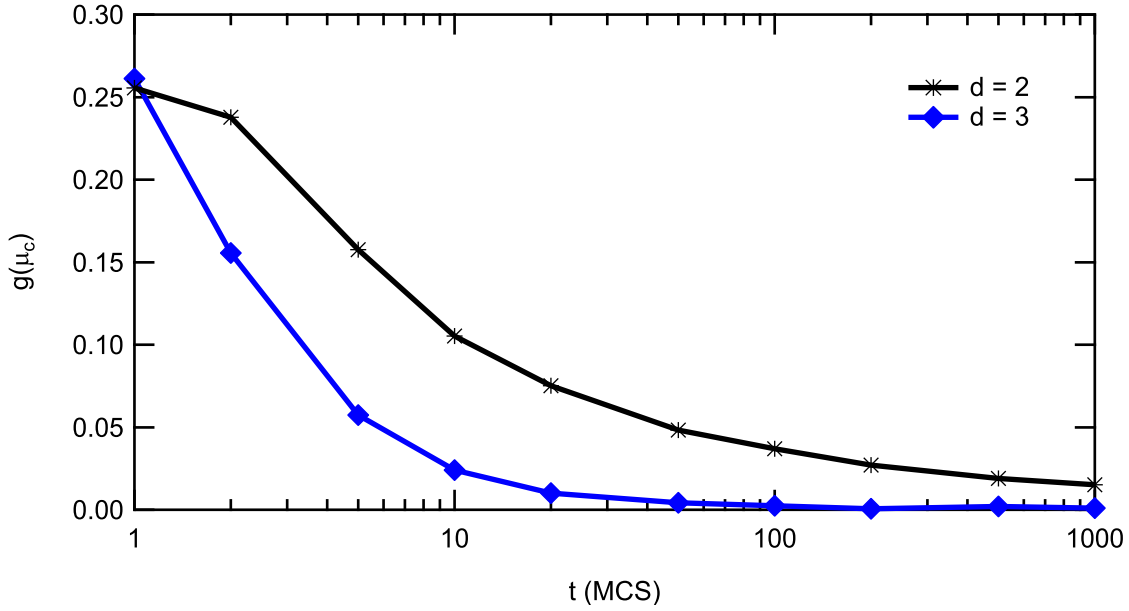

Figure 3.9: Comparison between the formation of the Coulomb gap in two and three dimensions. $L = 16$, $N = 256$ sites, and $T = 0.02$ for the two-dimensional case. $L = 8$, $N = 512$ sites, and $T = 0.02$ for the three-dimensional case.

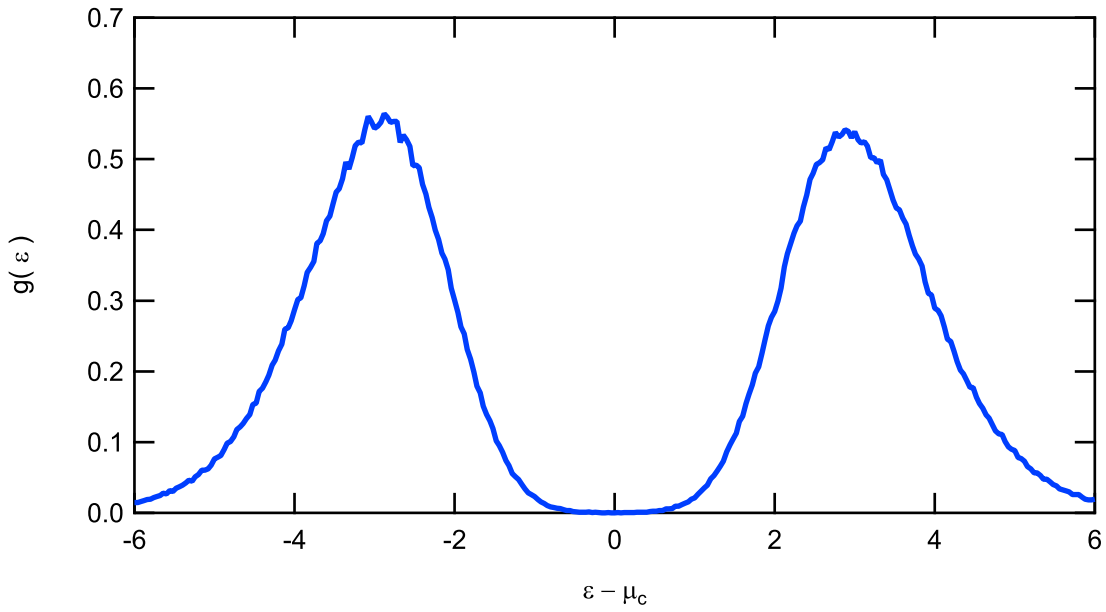

Figure 3.10: Example of the Coulomb gap in the two-dimensional Bose glass ($L = 16$, $N = 256$ sites) at temperature $T = 0.02$.

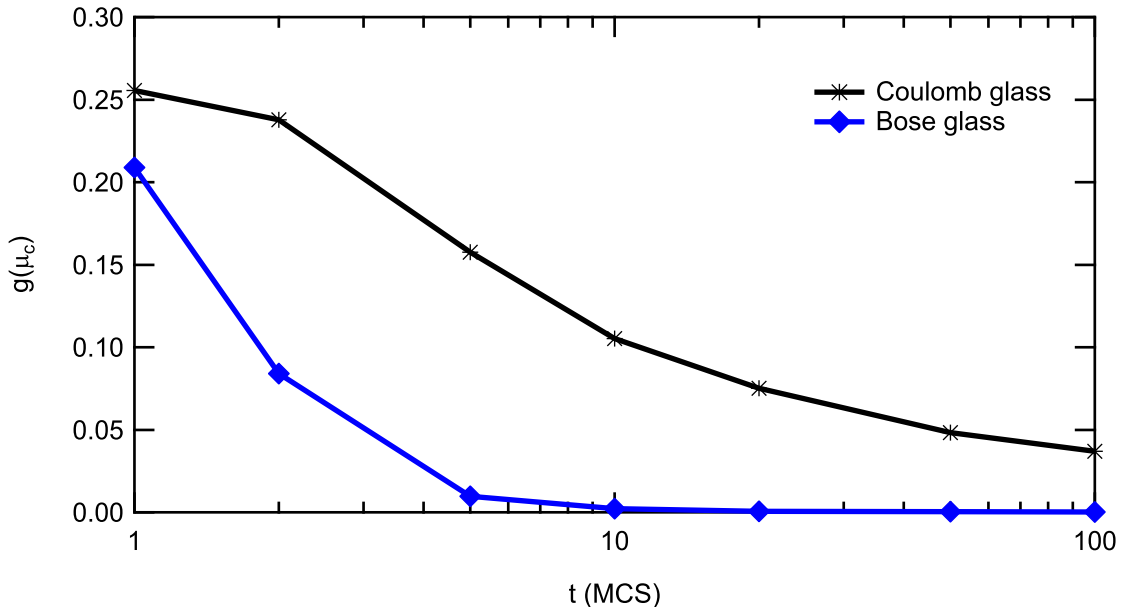

Figure 3.11: Comparison between the formation of the Coulomb gap with differing potentials. $L = 16$, $N = 256$ sites, and $T = 0.02$.

Another interesting aspect of the Bose glass system is the apparent lack of dependence on temperature for the DOS. There is no perceptible difference of the DOS for the various temperatures we measured (Figure 3.12). Likewise, the speed of formation of the Coulomb gap is unaffected by temperature within the interval $0.001 \leq T \leq 0.1$ as illustrated in Figure 3.13. This is most likely due to the broadness of the Coulomb gap. A temperature of $T = 0.1$ may not be sufficient to overcome the gap in the Bose glass system, whereas it would be enough in the Coulomb interacting system. As a side note, it will be shown later (Chapter 5) that the relaxation rate of the correlation function for this system *does* depend on temperature, even within a smaller temperature interval then the one discussed here. Filling fraction has the same effect on the density of states that it had on the Coulomb glass model, namely a shifting of the peaks (Figure 3.14).

Motivated by the power law fit for the Coulomb glass model (see §3.2), we checked the Bose glass model for a power law in the density of states. As evident in Figure 3.15, a power law is justifiable. The measurements for the gap exponent are given in Figures 3.16 and 3.17 for varying temperatures and filling fractions respectively. We saw a very large gap exponent (compared to the two-dimensional Coulomb glass) for the Bose glass, and one that has very little dependence on temperature and filling fraction within the configuration space that we probed. The value found here is higher than the value found in Ref [31] where they found a maximum effective exponent of approximately 3. Even though the power law may not be quantitatively the most accurate fit, qualitatively we would expect suppressed motion within the Bose glass system leading to very slow relaxation given such a large gap exponent.

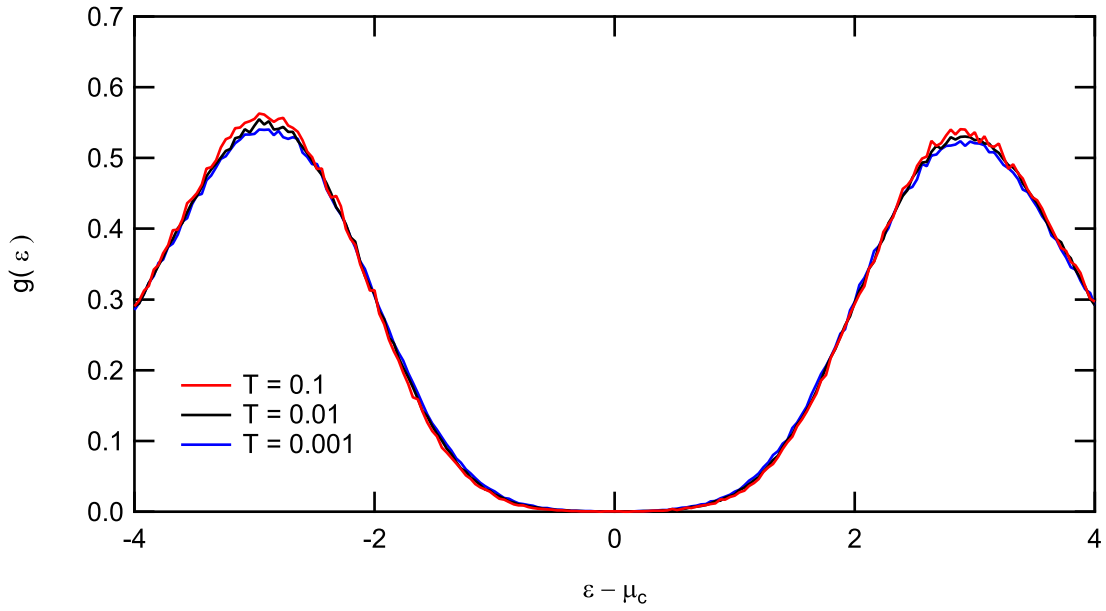

Figure 3.12: Density of states for various operating temperatures. Bose glass model with $L = 16$ and $N = 256$ sites.

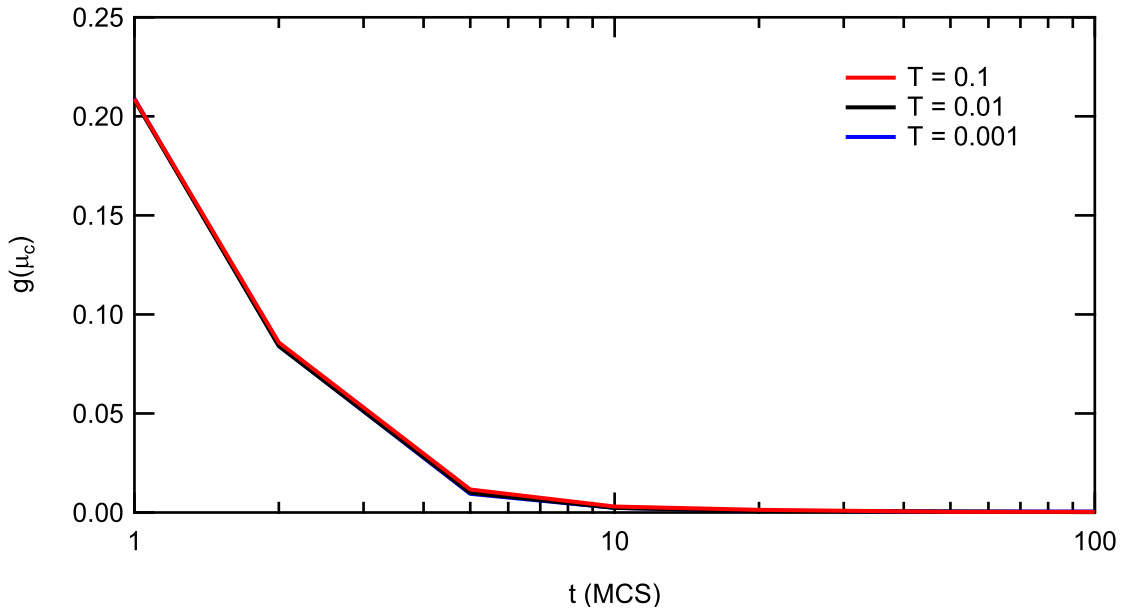

Figure 3.13: Coulomb gap formation over time with different operating temperatures. Bose glass model, $d = 2$, $L = 16$, and $N = 256$ sites.

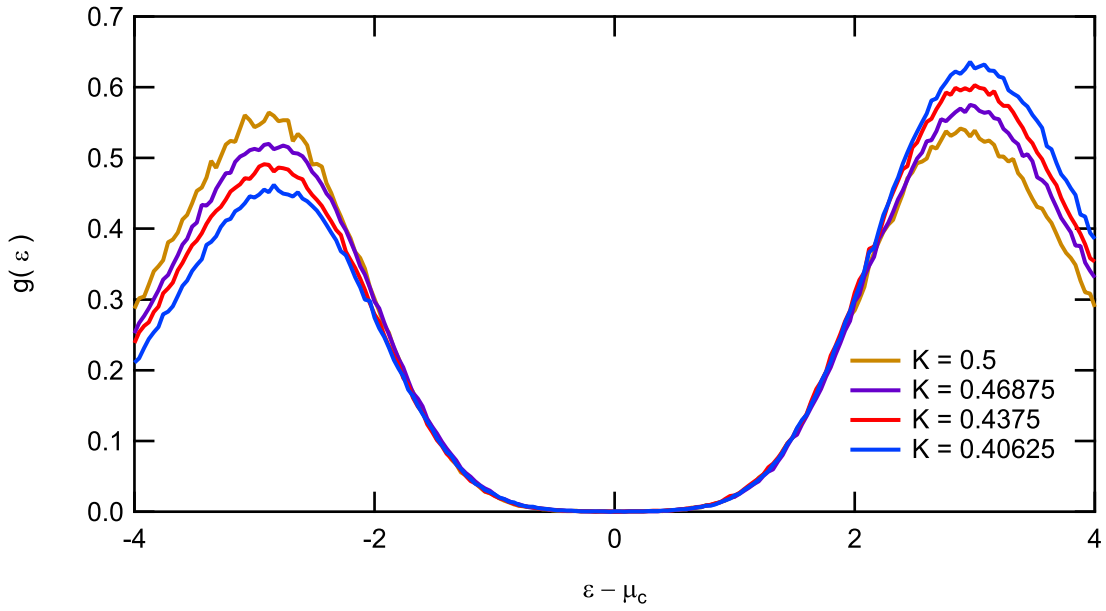

Figure 3.14: Density of states for various filling fractions. Bose glass model with $T = 0.02$, $L = 16$, and $N = 256$ sites.

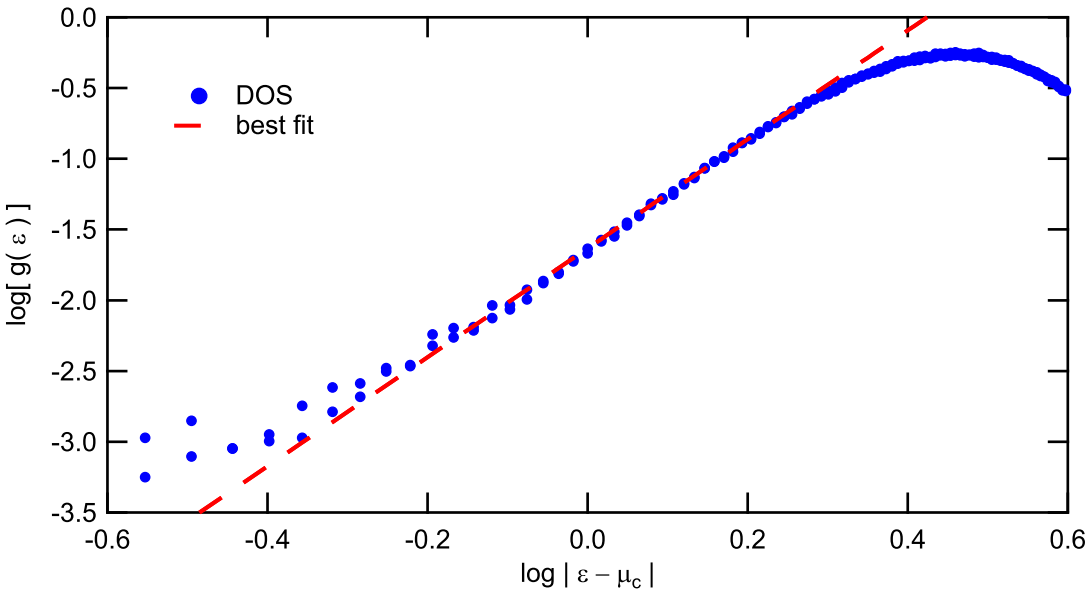

Figure 3.15: Logarithmic plot of the density of states for the Bose glass model, $d = 2$, $L = 16$, $N = 256$ sites, and $T = 0.02$. The dashed line represents the best power law fit.

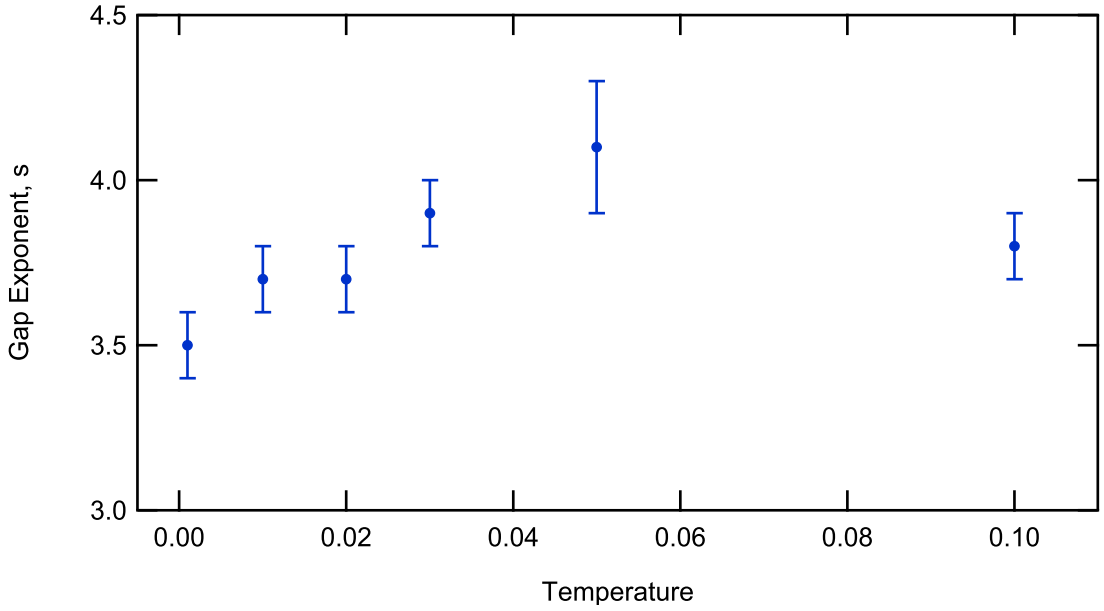

Figure 3.16: Values for the gap exponent, s, for different operating temperatures of the Bose glass model. $d = 2$, $L = 16$, and $N = 256$ sites.

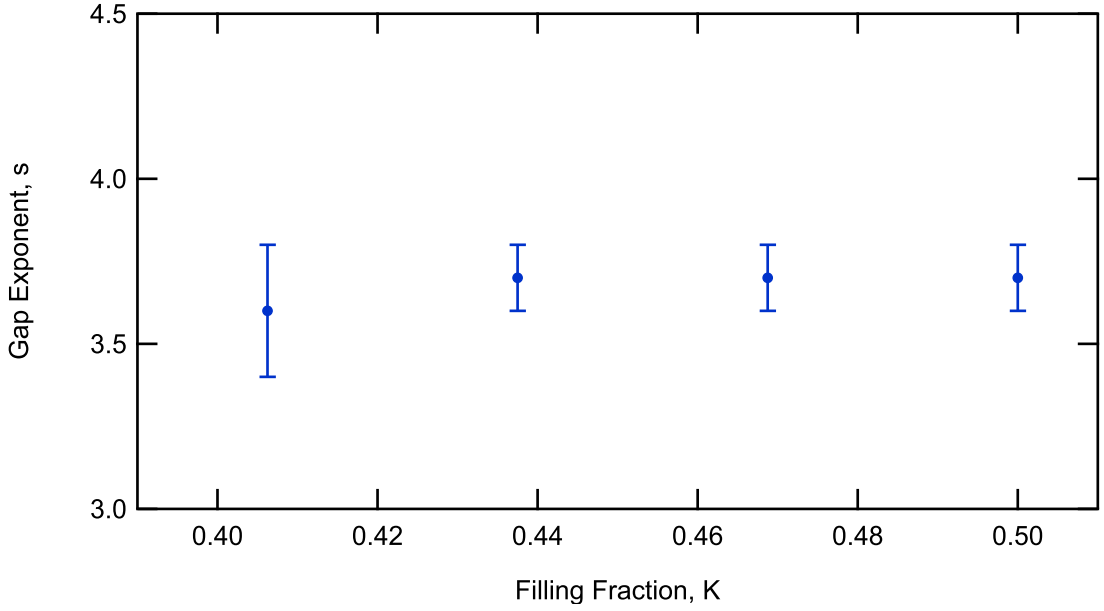

Figure 3.17: Values for the gap exponent, s, for different filling fractions of the Bose glass model. $d = 2$, $L = 16$, and $N = 256$ sites.

Chapter 4

Aging and Scaling Forms

When discussing aging phenomena, we are referring to a change of properties over time. The first experiment that showed that aging effects can be fully reproducible were done in 1978 by Struik [36]. First, Struik quenched glass-forming PVC from the liquid phase into a glassy state and out of equilibrium. He then applied mechanical stress after waiting a period of time, s and the linear response was measured. This was repeated with various values of s. What Struik found was *very* slow relaxation as well as the relaxation depending on the value of s. More specifically, the longer the time between the quench and the applied stress, the slower the relaxation. This meant that time-translation invariance was broken. Amazingly, Struik also showed that by scaling the relaxation curves for various values of s, he was able to collapse all curves on top of each other.

To summarize, if a system is swiftly perturbed (quench in the above example), a high level

of disorder may prevent rapid relaxation towards the stationary state. This system would be undergoing *aging* behavior. The key aspects to aging are slow relaxation dynamics, two-time dependence on response (no time-translation invariance), and dynamical scaling (collapse of all relaxation curves in the above example).

This chapter deals with the aging kinetics and scaling forms of the two-time carrier density autocorrelation function. I will first define the autocorrelation function and then use it to demonstrate the relaxation dynamics of the model in Section 4.1. Two important characteristics of aging will also be shown in Section 4.1, namely slow relaxation dynamics and time-translational invariance. Two proposed scaling forms will be detailed in Section 4.2 — subaging scaling and full-aging scaling. I will illustrate the fact that both scaling forms show dynamical scaling in the scaling regime. Three scaling exponents can be derived from the scaling forms. The method I used in order to measure these scaling exponents will be discussed in Section 4.3.

4.1 Relaxation Dynamics

In order to measure the response from the high-temperature quench we employ the (normalized) two-time carrier density autocorrelation function [19],

$$C(t,s) = \frac{\langle n_i(t) n_i(s) \rangle - K^2}{K(1-K)} = \frac{\sum_i n_i(t) n_i(s) - NK^2}{NK(1-K)}\,, \tag{4.1}$$

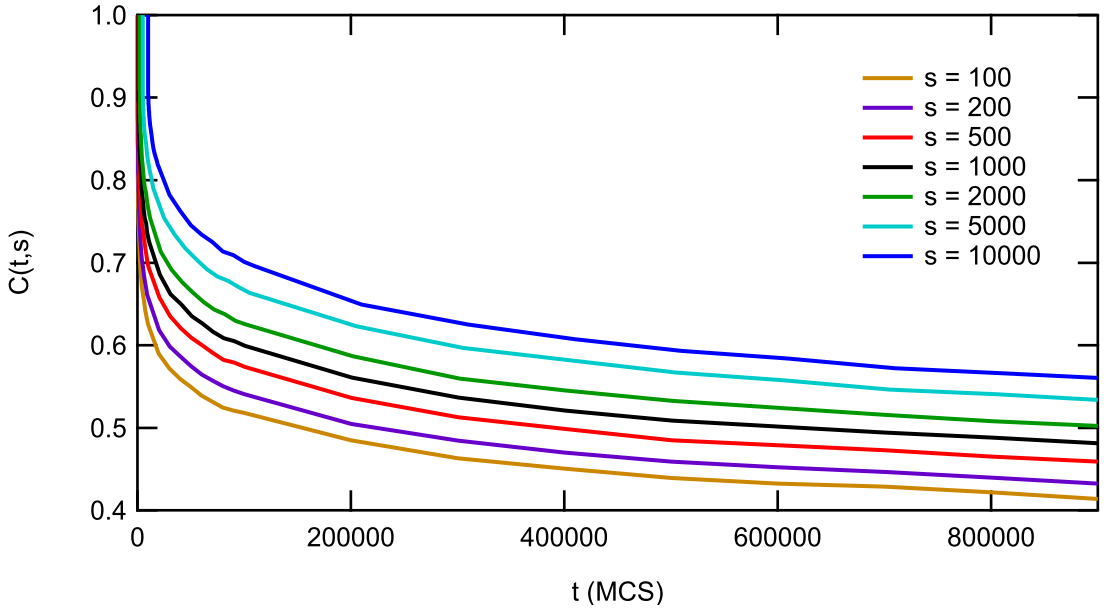

Figure 4.1: Two-time autocorrelation function versus operating time t with various waiting times s. Two-dimensional Coulomb glass system with $L = 16$, $K = 0.5$, and $T = 0.02$.

where s is the waiting time, n_i is the occupation number of site i, N is the total number of sites, and K is the filling fraction given in equation (2.2). It should also be noted that $t > s$, and both times, t and s, refer to the time elapsed since the high-temperature quench (initiation of the Monte Carlo simulations). A sample plot from our simulations of the autocorrelation function, $C(t, s)$, versus time can be seen in Figures 4.1 and 4.2.

The slow relaxation of the system should be very apparent in Figures 4.1 and 4.2 as after 10^6 Monte Carlo time-steps (MCS) the system has not reached any type of steady state. Figure 4.2 also illustrates the different relaxation regimes. The first regime, which corresponds to "vibrations" of the charge carriers around their initial positions as well as the group motion of charge carrier clusters, is reminiscent of β *relaxation* in structural glasses [37, 38]. This

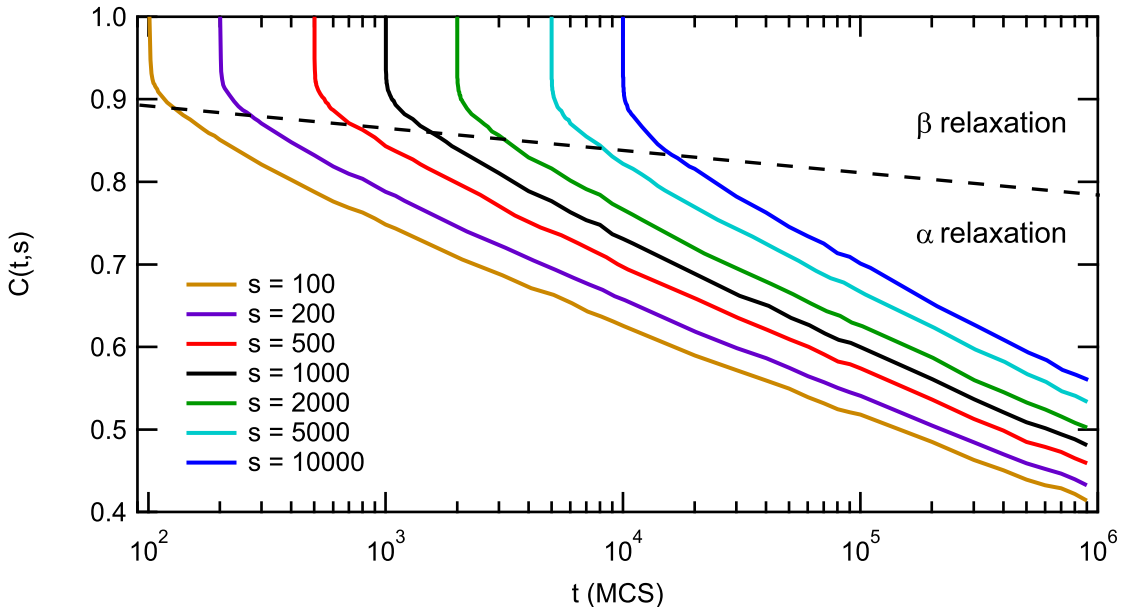

Figure 4.2: Two-time autocorrelation function versus operating time t with various waiting times s. Two-dimensional Coulomb glass system with $L = 16$, $K = 0.5$, and $T = 0.02$. Two relaxation regions that resemble so called β and α relaxation in structural glasses are labeled.

period is dominated by high-energy hops from charge carriers that were initially very near each other. The charge carriers quickly become confined by neighboring pockets, or clusters, of charge carriers. A snapshot of the energy landscape during this relaxation mode is shown in Figure 4.3(a). After some time the pockets break down and allow the charge carriers to relax towards an equilibrium steady state. This period, which resembles α *relaxation* and will be referred to as the scaling regime, will be our primary focus (see Figure 4.3(b) for a snapshot of the energy landscape for this relaxation mode). For more information on these different relaxation time regimes, especially the β *relaxation* mode which is outside the scope of this dissertation, see Ref. [37, 38]. It is important to note that we see relaxation that bears resemblance to α and β relaxation; however, it is difficult to tell whether these relaxation modes are actually present within our system. The change in relaxation rates possibly has more to do with the long range correlations than the structure of the system. I mention α and β relaxations here as the resemblance is strong and it allows for easier designation of the aforementioned scaling regime.

Going back to eq. (4.1) another aspect of aging can be observed. If both t and s are large compared to microscopic time scales, τ_0, and also well separated, i.e., if

$$t \gg \tau_0\,, \quad s \gg \tau_0\,, \quad t - s \gg \tau_0\,, \tag{4.2}$$

time-translational invariance is broken and $C(t, s)$ depends on both t and s separately. This can be seen in Figure 4.4 (along with the relaxation modes) since different values of s produce

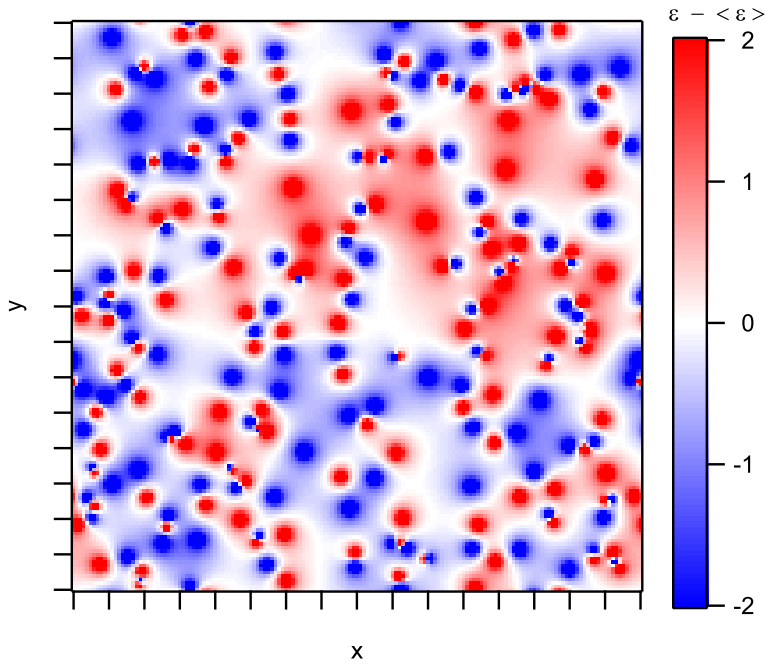

(a)

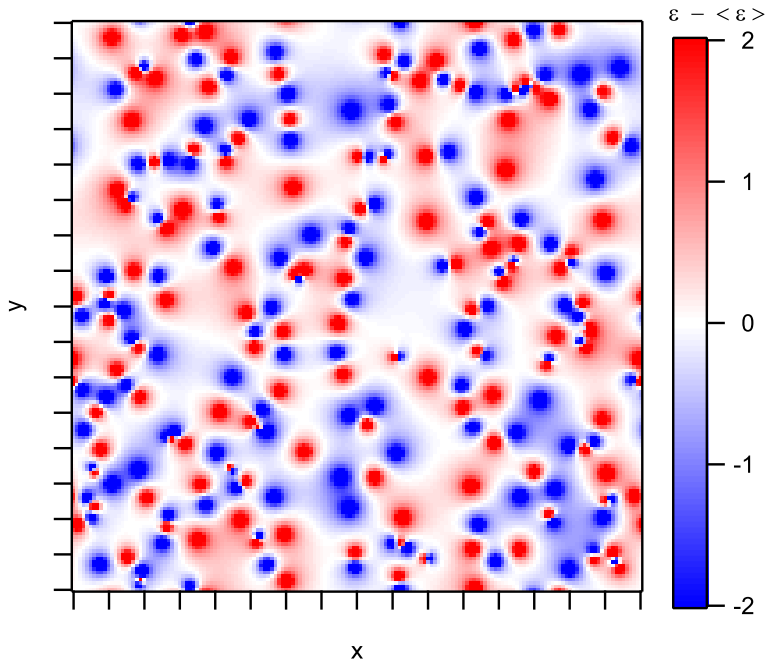

(b)

Figure 4.3: Energy landscape of the two-dimensional Coulomb glass after (a) 10 MCS and (b) 10^6 MCS with $L = 16$, $K = 0.5$, and $T = 0.02$.

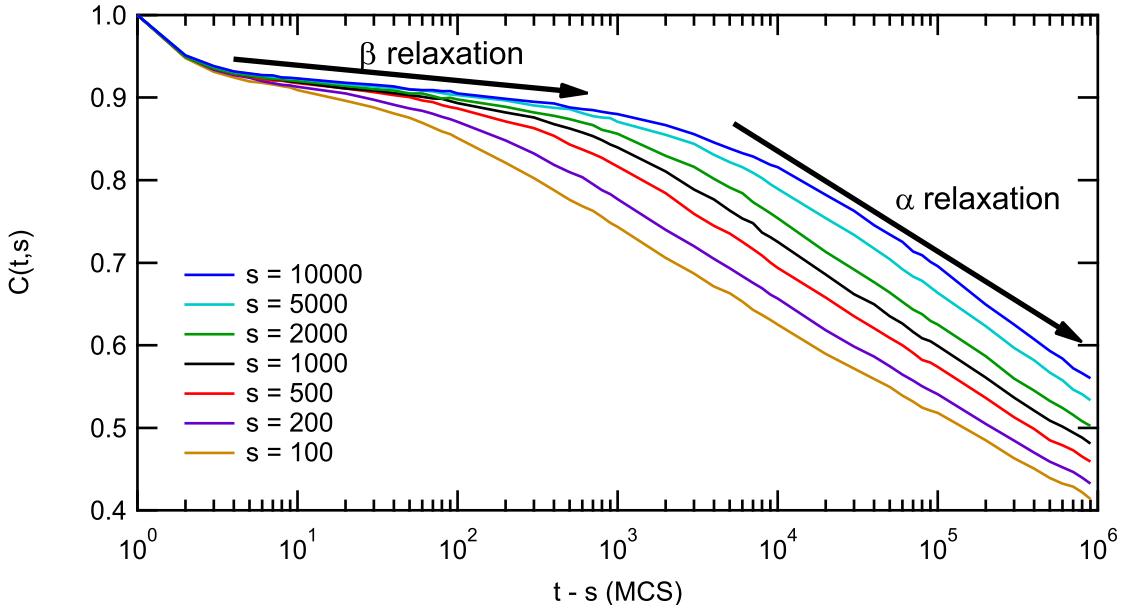

Figure 4.4: Two-time autocorrelation function versus $t-s$. Two-dimensional Coulomb glass system with $L = 16$, $K = 0.5$, and $T = 0.02$. Two relaxation regimes that resemble β and α relaxation are labeled.

distinctive curves.

We also attempted to measure the correlation length of the system and how it changed with time via the spatial correlation function; however, this yielded results that showed no change in the correlation length after just a few MCS. We believe the four-point autocorrelation function may provide better results and needs to be explored further.

4.2 Dynamical Scaling

Figure 4.4 also shows the possibility of shifting — either horizontally or vertically — the curves on top of one another to form a master curve [1]. This is known as *dynamical scaling* and is a hallmark of systems undergoing aging kinetics. This allows for a way to analyze the relaxation behavior of this system even though it is dependent on two times. The following are two proposed scaling forms for the master curve. It should be noted that both scaling forms offer (qualitatively) the same level of data collapse.

4.2.1 Subaging Scaling Form

The autocorrelation function is often "split" into a stationary and an aging part [1], i.e.

$$C(t,s) = C_{st}(t-s) + C_{age}(t,s)\,, \tag{4.3}$$

where $\lim_{t-s\to\infty} C_{st}(t-s) = 0$. The *aging* part of the autocorrelation function is then assumed to follow the scaling form [1]

$$C_{age}(t,s) \approx F_C\left(h(t)/h(s)\right)\,. \tag{4.4}$$

The time-reparametrization function, $h(t)$, in equation (4.4) is of the form [1]

$$h(t) = h_0 \exp\left[\frac{1}{A}\frac{t^{1-\mu}-1}{1-\mu}\right], \tag{4.5}$$

where μ is a free parameter and h_0 and A are constants. Experimental analysis of glassy systems will generally simplify (4.4) to

$$C_{age}(t,s) \approx F_C\left(t/s^{\mu}\right). \tag{4.6}$$

This stems from the fact that equation (4.4) suggests a time scale growing as s^{μ} [1, 20].

Equation (4.6) offers us one scaling exponent, μ. Also, μ can be used to classify the aging behavior of the system — subaging when $0 < \mu < 1$, full-aging when $\mu = 1$, and superaging when $\mu > 1$. Figure 4.5 shows an example of dynamical scaling using the subaging scaling form.

4.2.2 Full-Aging Scaling Form

In the aging scaling regime expressed in equation (4.2), one expects the autocorrelation function to obey the general scaling form [1],

$$C(t,s) = s^{-b} f_C(t/s^{\mu}), \tag{4.7}$$

For systems obeying purely relaxational dynamics, such as the one-dimensional kinetic Ising model [39, 40], the time-dependent Ginzburg–Landau models quenched to a critical point

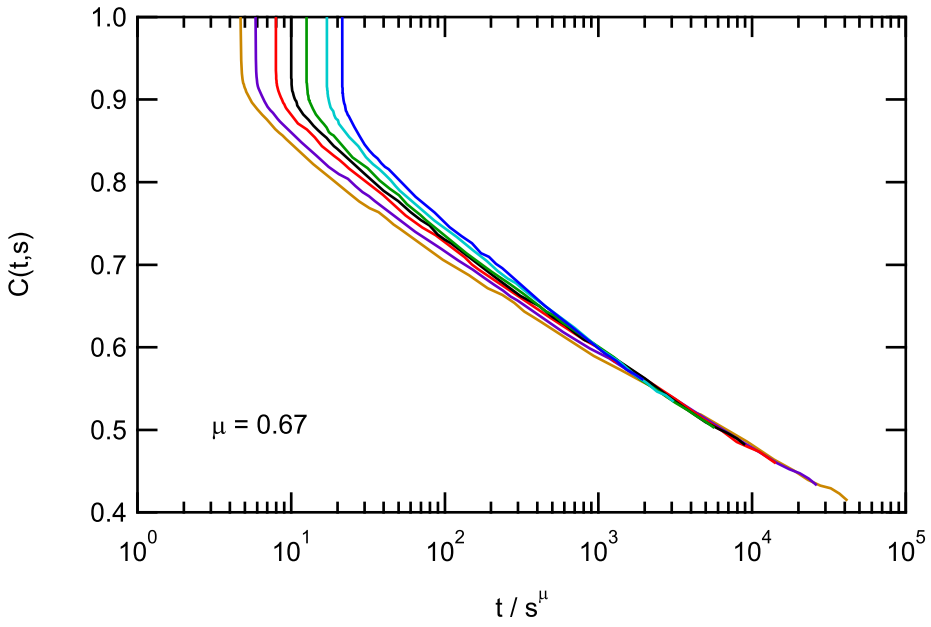

Figure 4.5: Subaging scaling of the two-dimensional Coulomb glass system with $L = 16$, $K = 0.5$, and $T = 0.02$. Best fit was found with a value of $\mu = 0.67$.

[41, 42], and the spherical model A coarsening dynamics in the low-temperature phase, with short-range [43, 44] or long-range [45–47] interactions, the aging scaling regime can be treated analytically. In these cases full-aging scaling, or setting $\mu = 1$ in equation (4.7), is sufficient to fully describe the relaxation dynamics. Also, for $\mu = 1$ and $t/s \to \infty$ the full-aging scaling function follows a power law [1],

$$f_C(t/s) \sim (t/s)^{-\lambda_C/z}\,, \tag{4.8}$$

with the autocorrelation exponent λ_C and the dynamic exponent z. Equations (4.7) and (4.8) present us with two more scaling exponents; namely b and λ_C/z. Figure 4.6 shows an

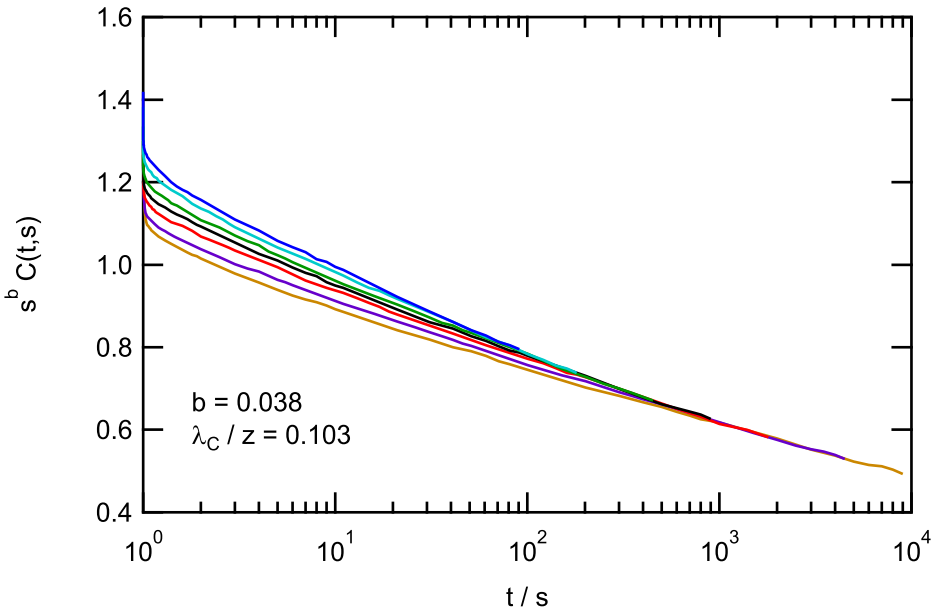

Figure 4.6: Full-aging scaling of the two-dimensional Coulomb glass system with $L = 16$, $K = 0.5$, and $T = 0.02$. Best fit was found with a value of $b = 0.038$ and $\lambda_C/z = 0.103$.

example of dynamical scaling using the full-aging scaling form.

4.3 Measurement of Scaling Exponents

Sections 4.2.1 and 4.2.2 offered three scaling exponents that describe the relaxation of the system. From the averaged charge density autocorrelation function (4.1) we extracted these scaling exponents using an interpolation method motivated by Ref. [48]. The first part of this method is to select a scaling "window" (or subset) of data to collapse as illustrated in Figure 4.7. This is important as we are only interested in the asymptotic scaling regime. In certain system configurations this becomes vitally important because of the presence of

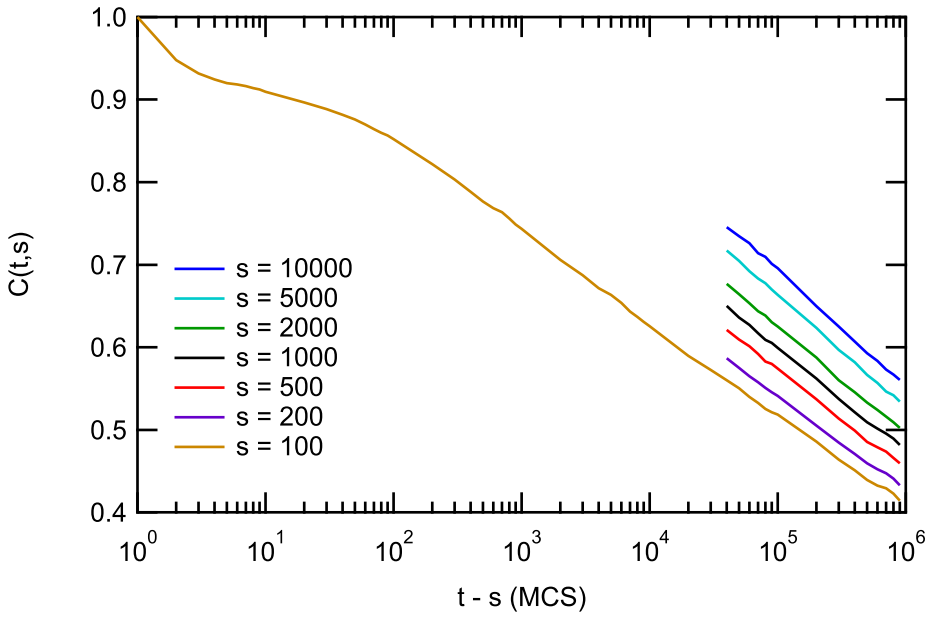

Figure 4.7: An example of a subset of data used for data collapse.

plateau regions (regions where the relaxation curves flatten out). These regions can occur just before the scaling regime and also just after. The total variance of the data is then calculated by comparing the data points of a specific curve to polynomial interpolations of all other curves within this window. This process is repeated for each of the different waiting time curves. By scanning through the scaling exponent in question (either μ or b), a minimum value for the variance can be found which corresponds to the best scaling fit. We have chosen to either assume subaging scaling (§4.2.1) by setting $b = 0$ in Eq. (4.7) and applied the polynomial interpolation method to obtain the subaging exponent $\mu < 1$; or to set $\mu = 1$ and alternatively determine the full-aging scaling exponent $b > 0$ (§4.2.2). This allows for a quantitative way to measure the best fit exponents for both scaling methods.

Chapter 5

Results

We ran simulation runs at various values of T and K to explore the dependence of the scaling exponents on the temperature and filling fraction. I will first display all the plots for our measurements on the autocorrelation function in Section 5.1. In Section 5.2, I will list our results from the subaging scaling analysis (Equation 4.6). Section 5.3 will describe the trends found in our results from the full-aging scaling analysis (Equation 4.7 and Equation 4.8). Then I will compare these two scaling methods in Section 5.4.

5.1 Autocorrelation Results

The following are the plots for the autocorrelation function. All two-dimensional Coulomb glass plots will have a system size of $L = 16$ ($N = 256$), three-dimensional Coulomb glass will have a system size of $L = 8$ ($N = 512$), and the Bose glass will have a system size

of $L = 24$ ($N = 576$). The other relevant system configurations will be provided in the captions.

5.1.1 2D Coulomb Glass

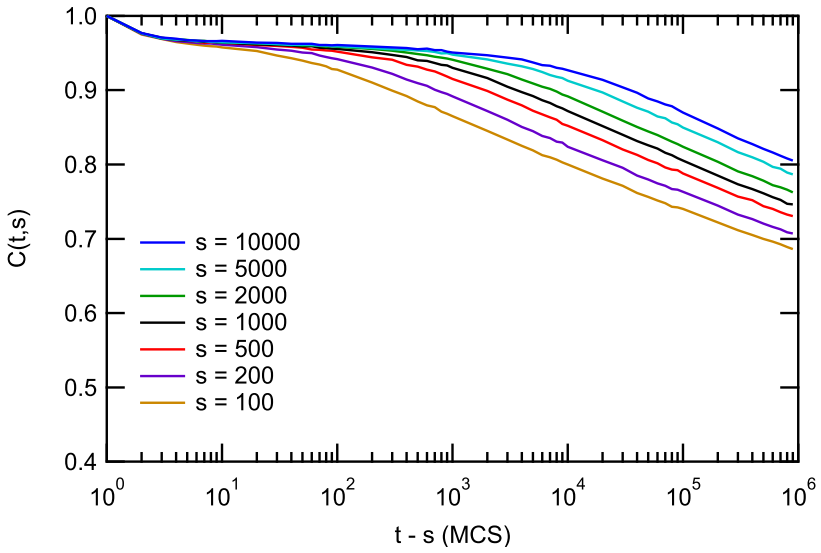

Figure 5.1: Two-time carrier density autocorrelation function for the two-dimensional Coulomb glass. $K = 0.5$ and $T = 0.01$.

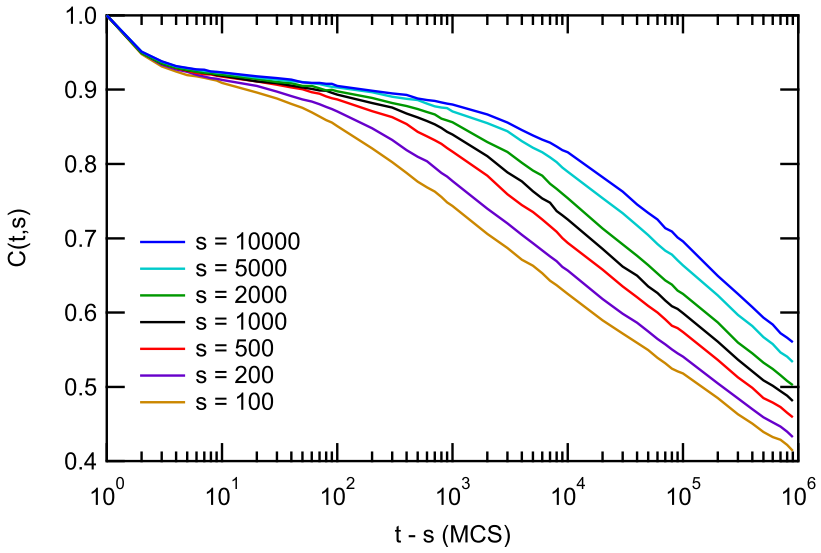

Figure 5.2: Two-time carrier density autocorrelation function for the two-dimensional Coulomb glass. $K = 0.5$ and $T = 0.02$.

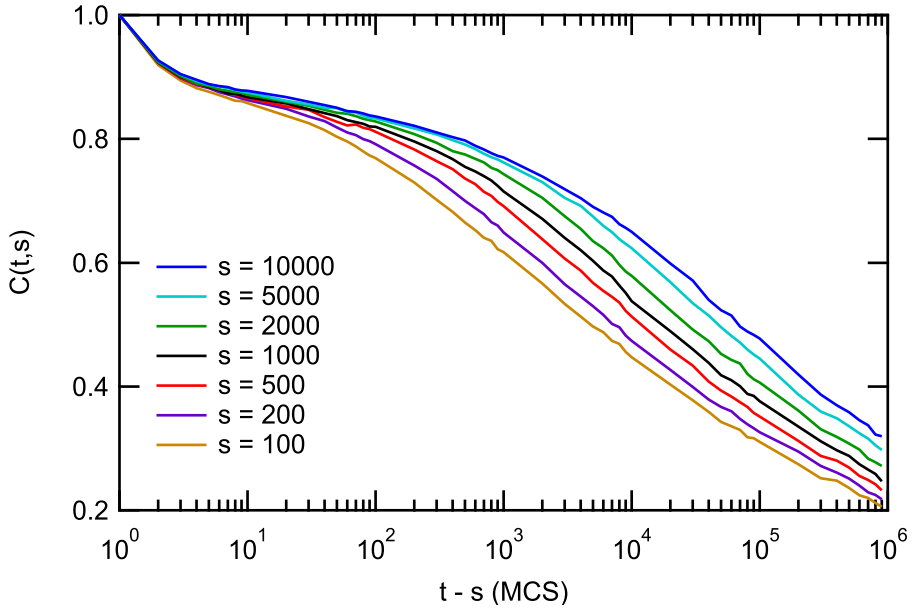

Figure 5.3: Two-time carrier density autocorrelation function for the two-dimensional Coulomb glass. $K = 0.5$ and $T = 0.03$.

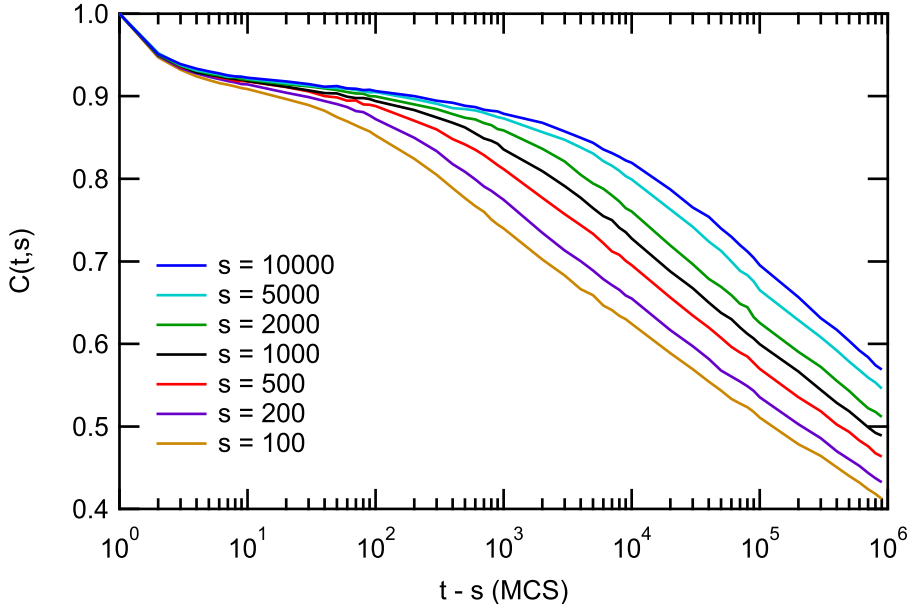

Figure 5.4: Two-time carrier density autocorrelation function for the two-dimensional Coulomb glass. $K = 0.46875$ and $T = 0.02$.

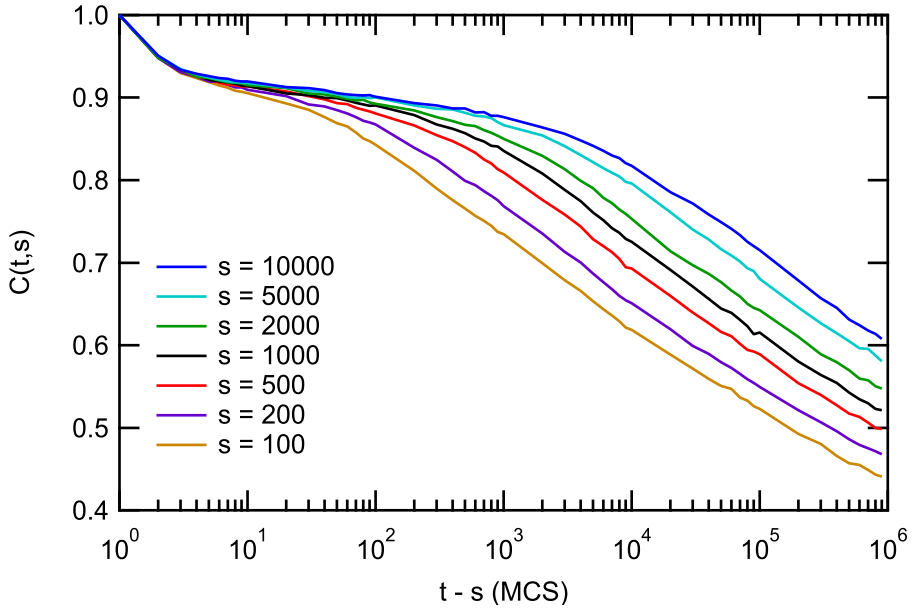

Figure 5.5: Two-time carrier density autocorrelation function for the two-dimensional Coulomb glass. $K = 0.4375$ and $T = 0.02$.

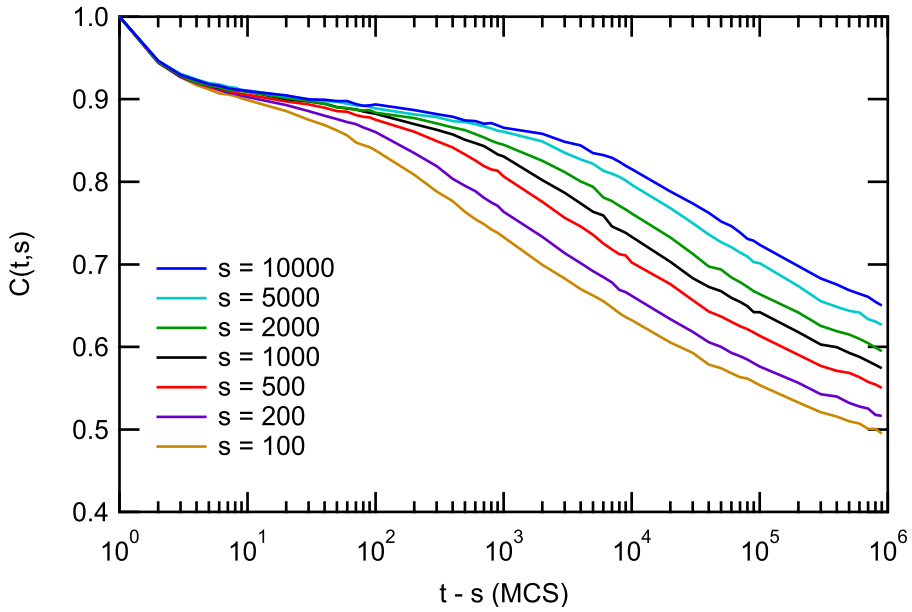

Figure 5.6: Two-time carrier density autocorrelation function for the two-dimensional Coulomb glass. $K = 0.40625$ and $T = 0.02$.

5.1.2 3D Coulomb Glass

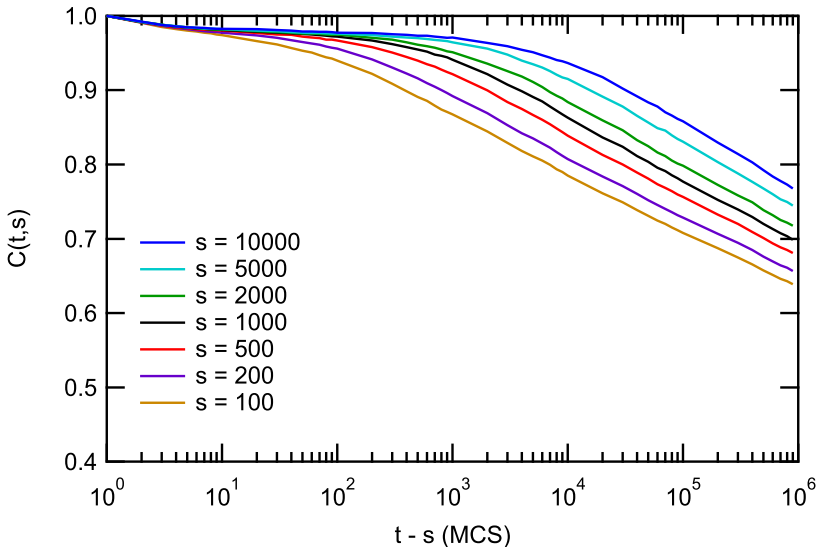

Figure 5.7: Two-time carrier density autocorrelation function for the three-dimensional Coulomb glass. $K = 0.5$ and $T = 0.01$.

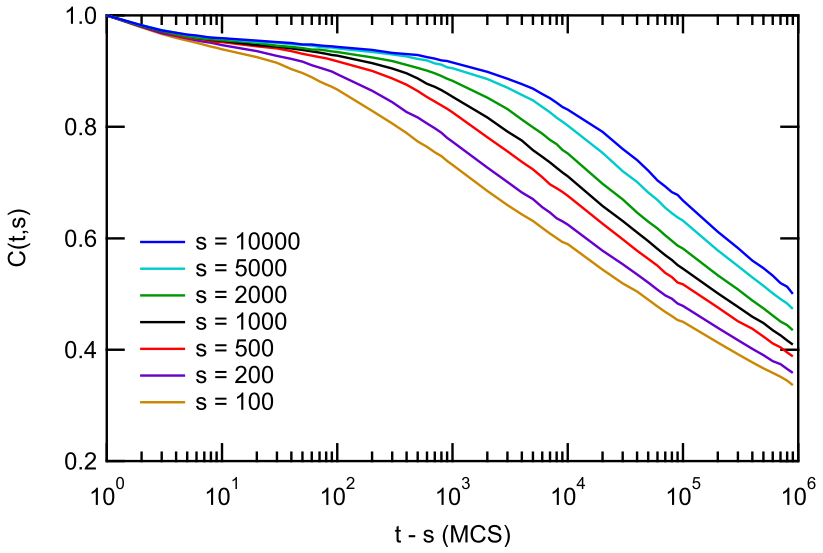

Figure 5.8: Two-time carrier density autocorrelation function for the three-dimensional Coulomb glass. $K = 0.5$ and $T = 0.02$.

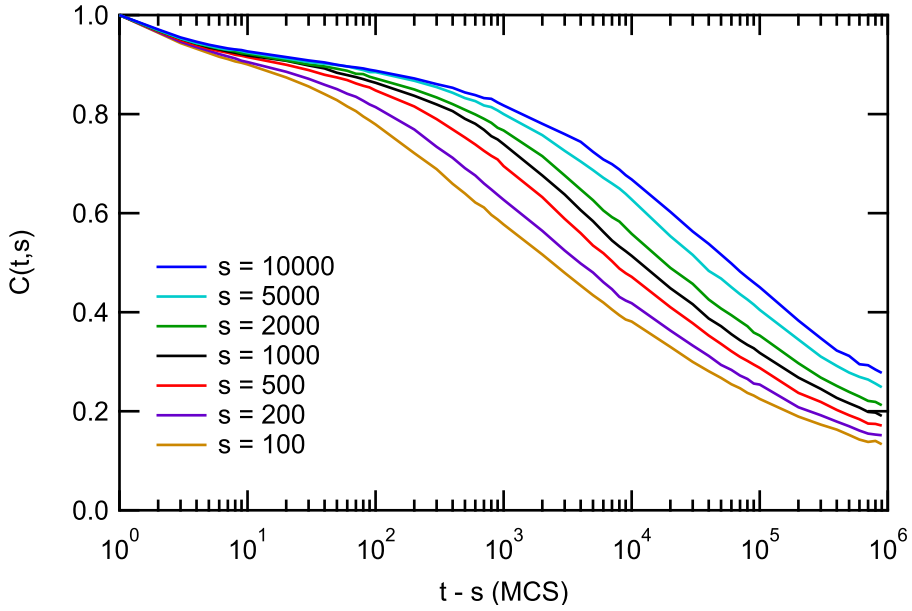

Figure 5.9: Two-time carrier density autocorrelation function for the three-dimensional Coulomb glass. $K = 0.5$ and $T = 0.03$.

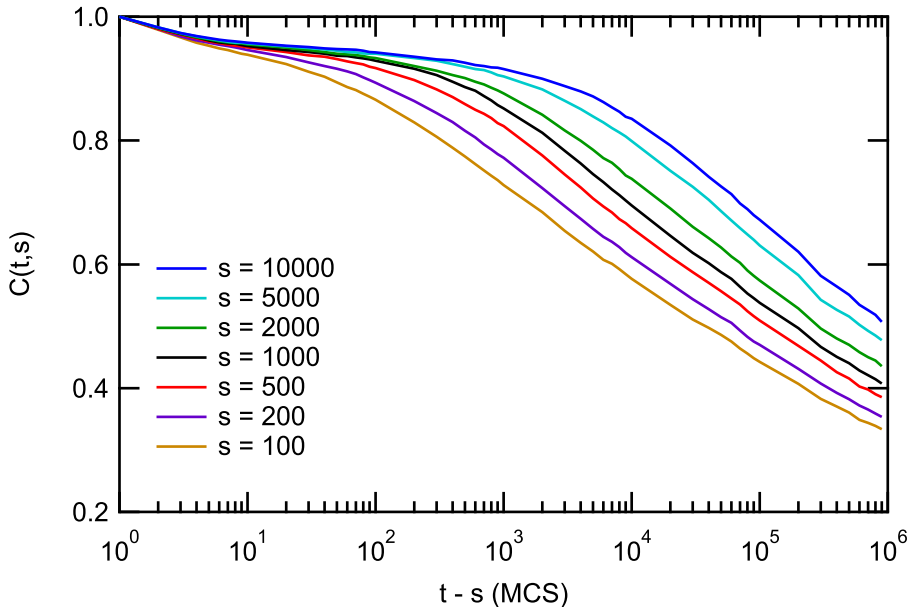

Figure 5.10: Two-time carrier density autocorrelation function for the three-dimensional Coulomb glass. $K = 0.46875$ and $T = 0.02$.

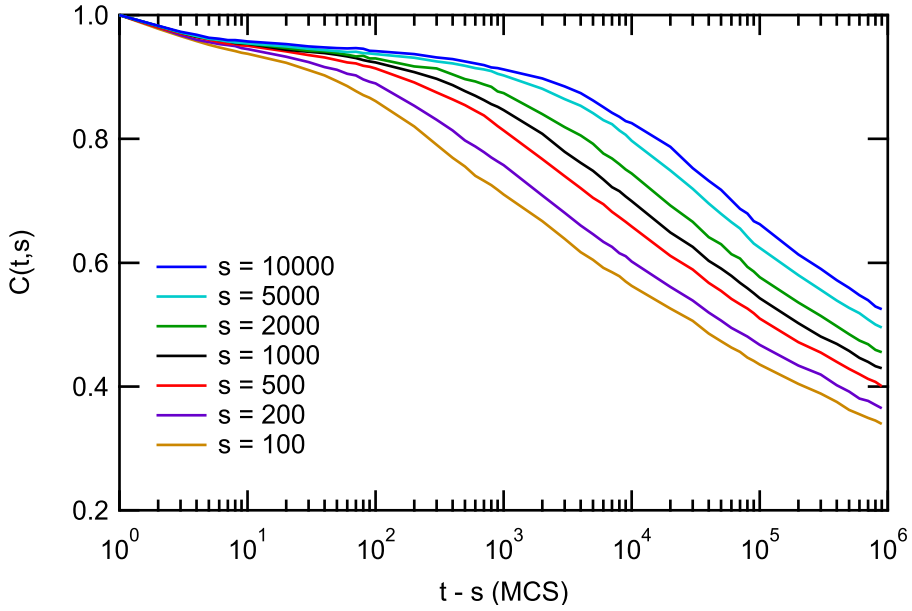

Figure 5.11: Two-time carrier density autocorrelation function for the three-dimensional Coulomb glass. $K = 0.4375$ and $T = 0.02$.

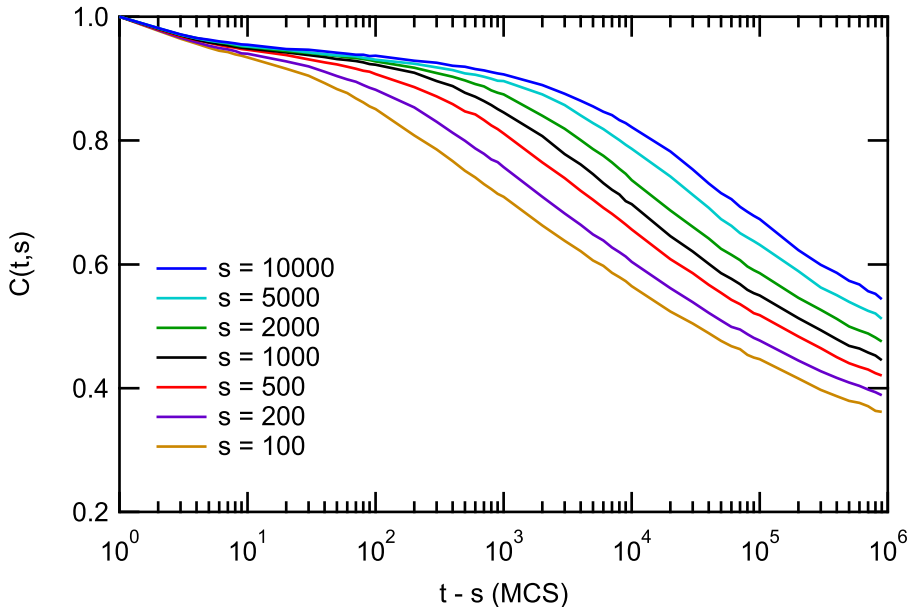

Figure 5.12: Two-time carrier density autocorrelation function for the three-dimensional Coulomb glass. $K = 0.40625$ and $T = 0.02$.

5.1.3 2D Bose Glass

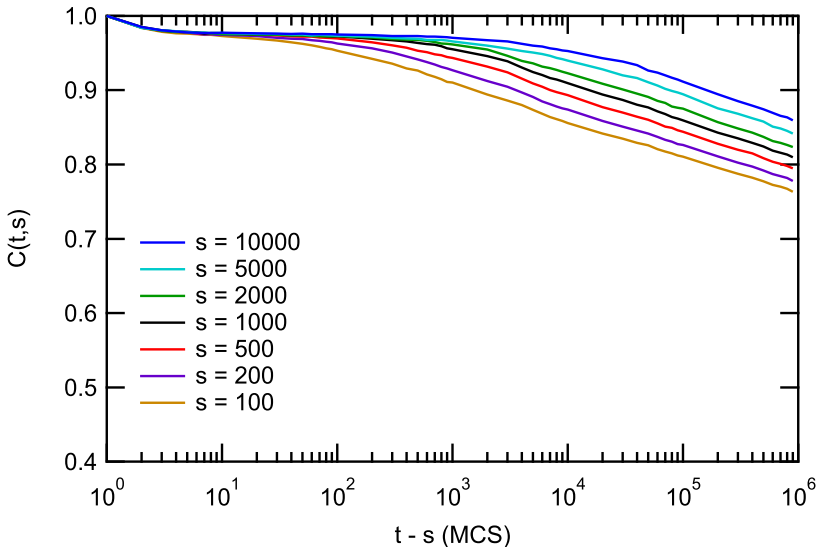

Figure 5.13: Two-time carrier density autocorrelation function for the Bose glass. $K = 0.5$ and $T = 0.01$.

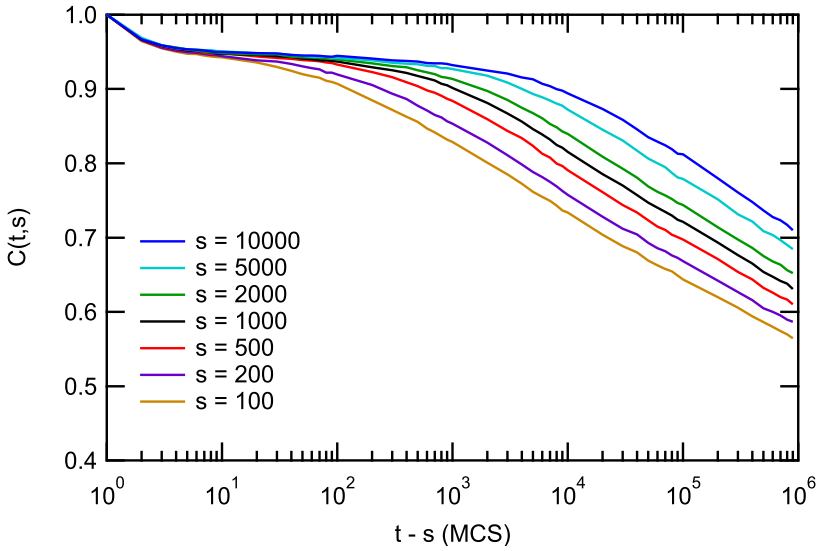

Figure 5.14: Two-time carrier density autocorrelation function for the Bose glass. $K = 0.5$ and $T = 0.02$.

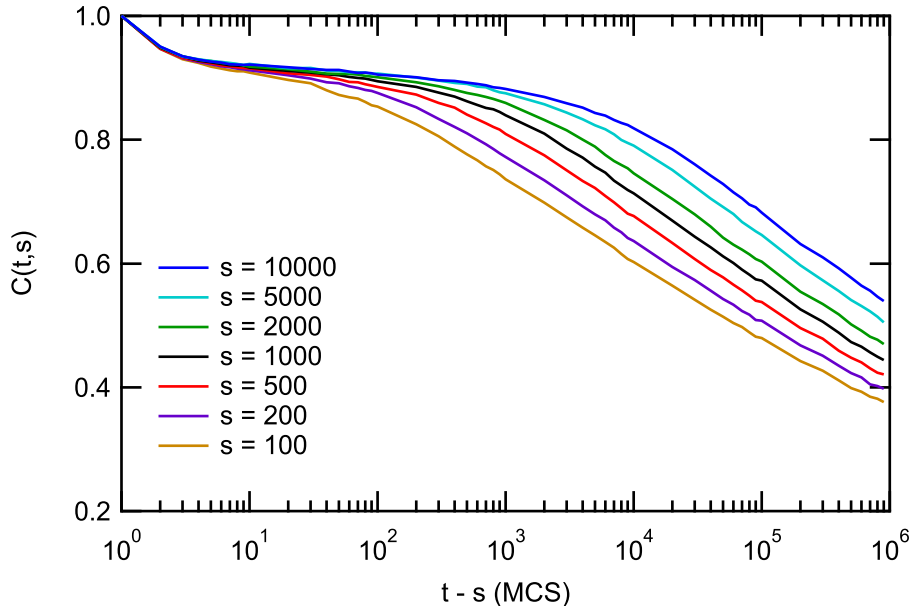

Figure 5.15: Two-time carrier density autocorrelation function for the Bose glass. $K = 0.5$ and $T = 0.03$.

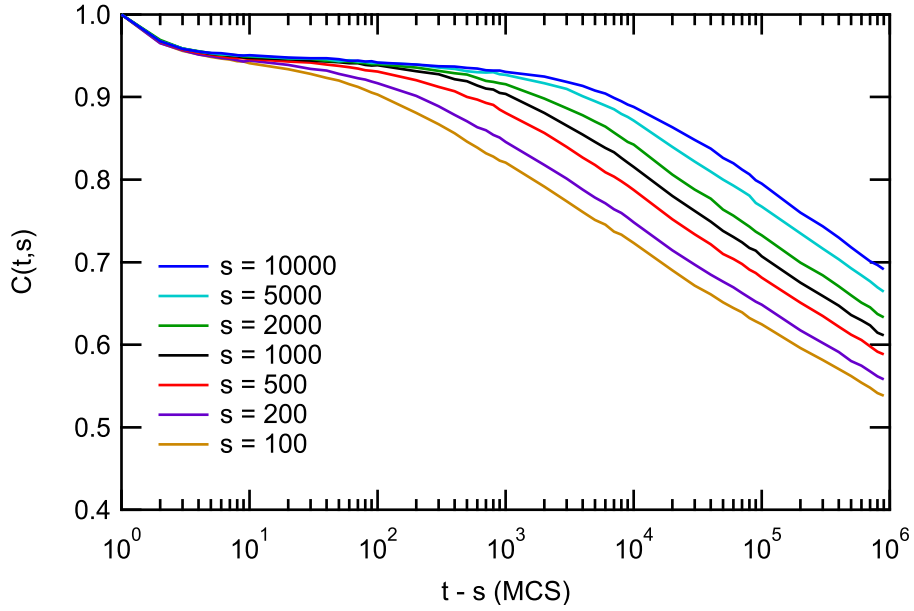

Figure 5.16: Two-time carrier density autocorrelation function for the Bose glass. $K = 0.46875$ and $T = 0.02$.

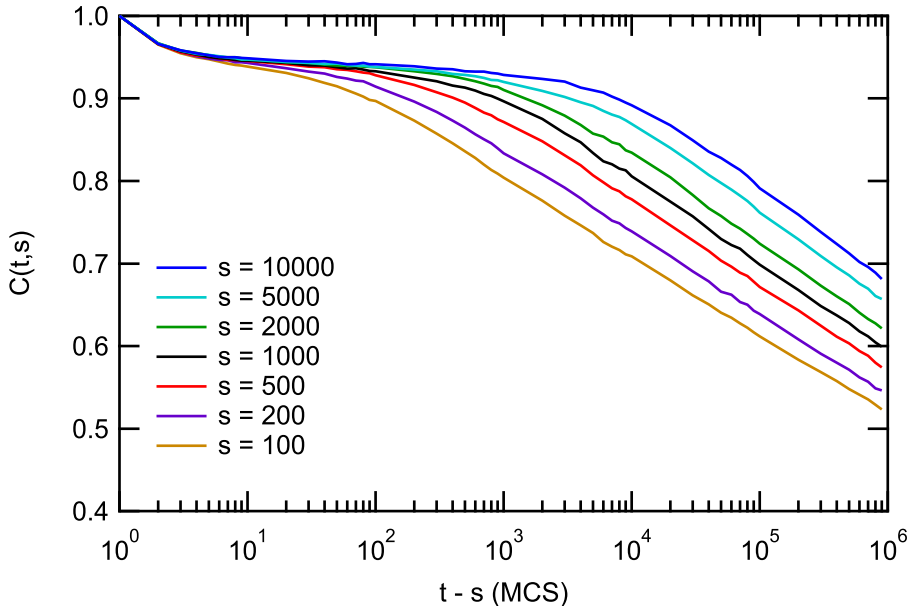

Figure 5.17: Two-time carrier density autocorrelation function for the Bose glass. $K = 0.4375$ and $T = 0.02$.

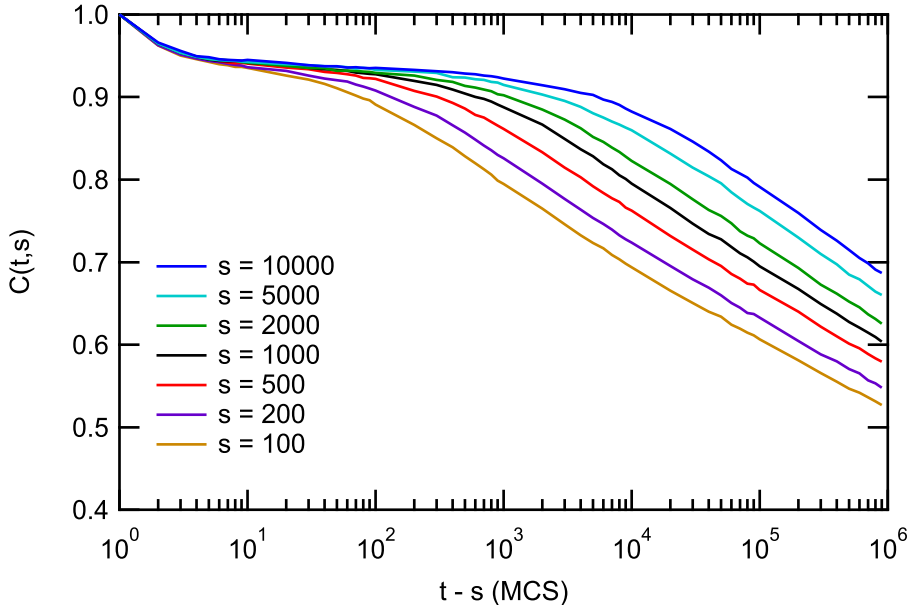

Figure 5.18: Two-time carrier density autocorrelation function for the Bose glass. $K = 0.40625$ and $T = 0.02$.

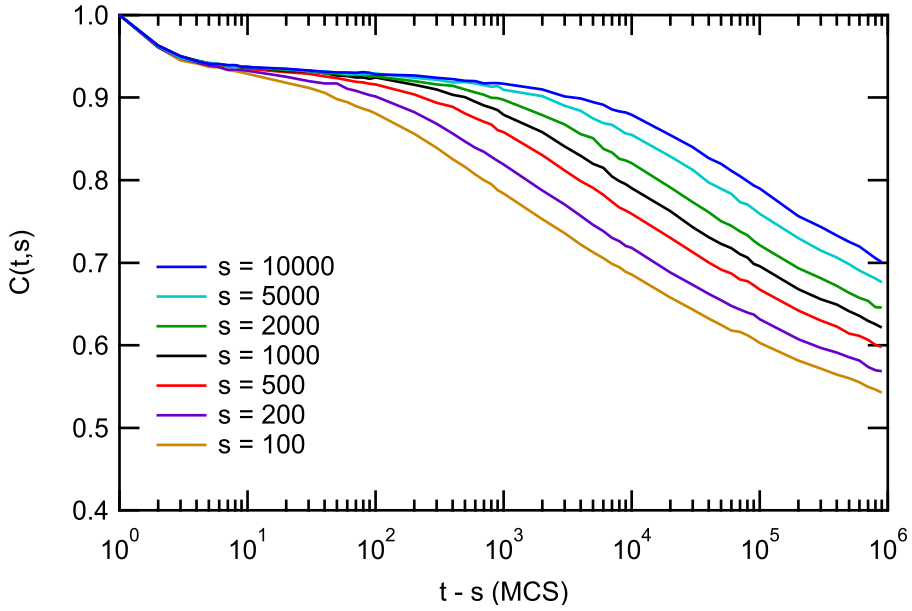

Figure 5.19: Two-time carrier density autocorrelation function for the Bose glass. $K = 0.375$ and $T = 0.02$.

5.2 Subaging Results

We found in §4.2.1 that the autocorrelation function could be scaled using a subaging analysis,

$$C_{age}(t, s) \approx F_C\left(t/s^{\mu}\right) . \tag{5.1}$$

I will first display all of the subaging scaling plots then I will discuss the values and trends on the subaging exponent. All two-dimensional Coulomb glass plots will have a system size of $L = 16$ ($N = 256$), three-dimensional Coulomb glass will have a system size of $L = 8$ ($N = 512$), and the Bose glass will have a system size of $L = 24$ ($N = 576$). The other

relevant system configurations will be provided in the captions.

5.2.1 2D Coulomb Glass

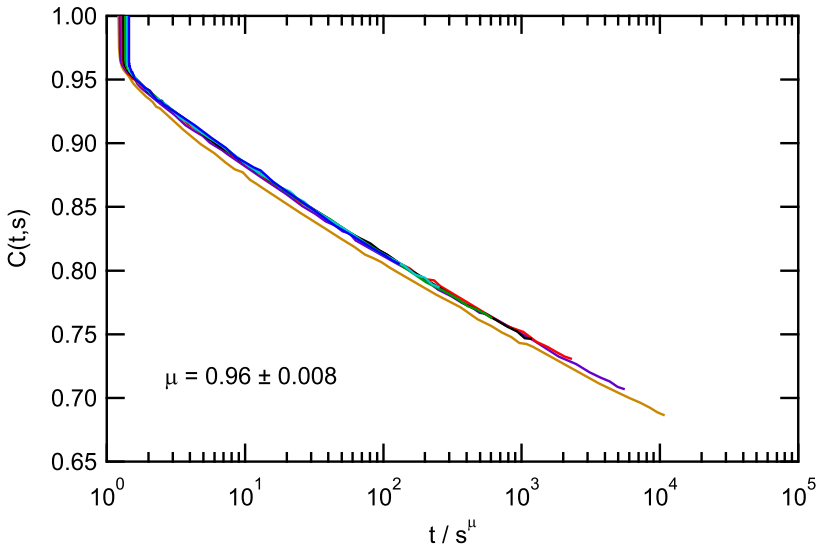

Figure 5.20: Subaging scaling plot for the two-dimensional Coulomb glass. $K = 0.5$ and $T = 0.01$.

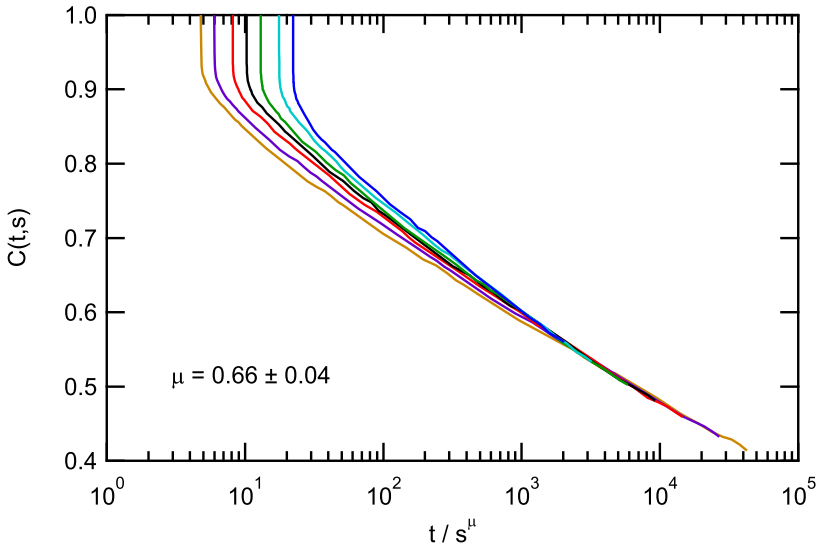

Figure 5.21: Subaging scaling plot for the two-dimensional Coulomb glass. $K = 0.5$ and $T = 0.02$.

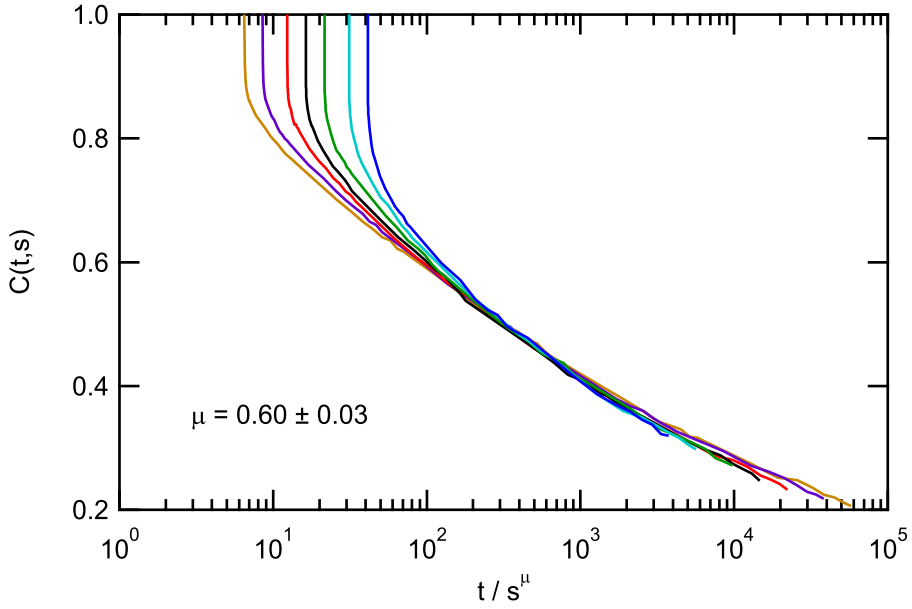

Figure 5.22: Subaging scaling plot for the two-dimensional Coulomb glass. $K = 0.5$ and $T = 0.03$.

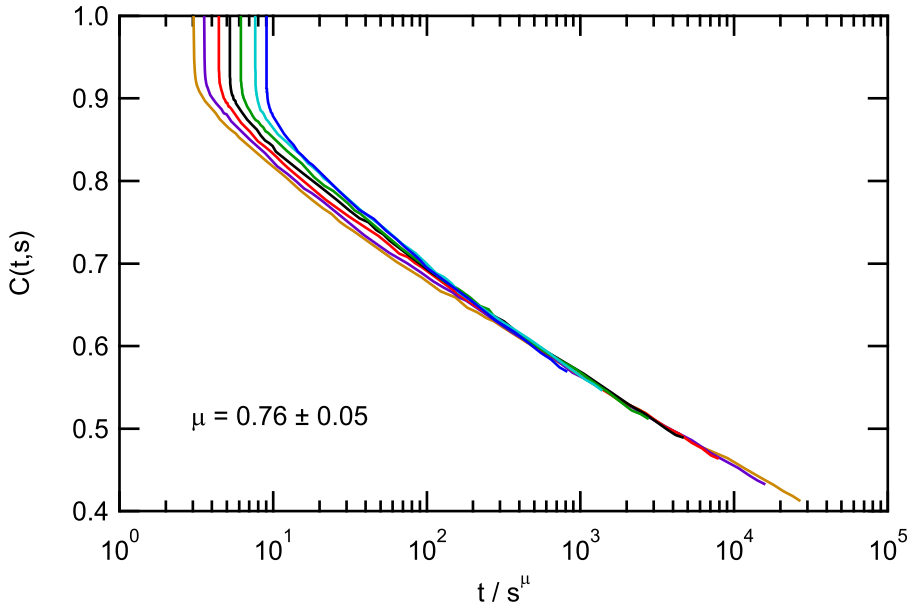

Figure 5.23: Subaging scaling plot for the two-dimensional Coulomb glass. $K = 0.46875$ and $T = 0.02$.

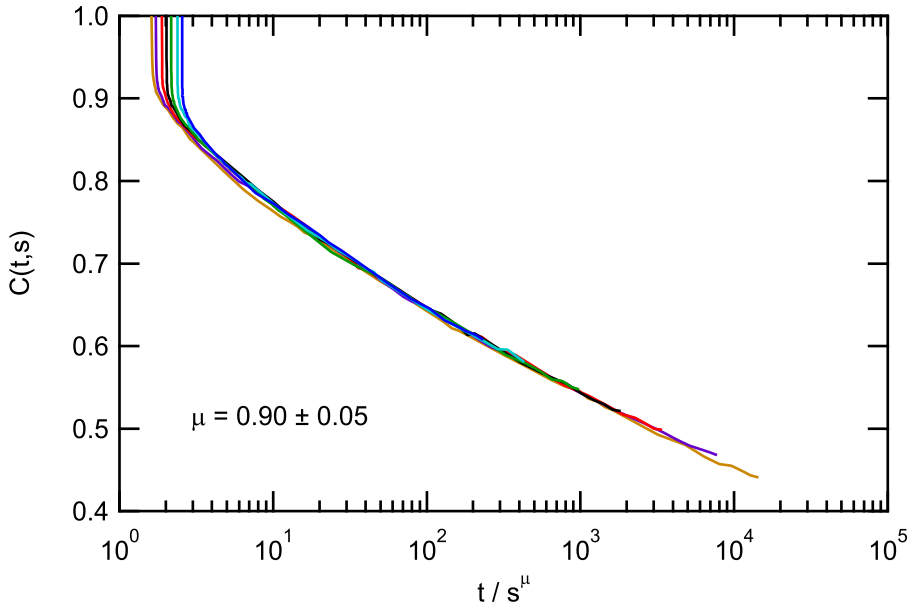

Figure 5.24: Subaging scaling plot for the two-dimensional Coulomb glass. $K = 0.4375$ and $T = 0.02$.

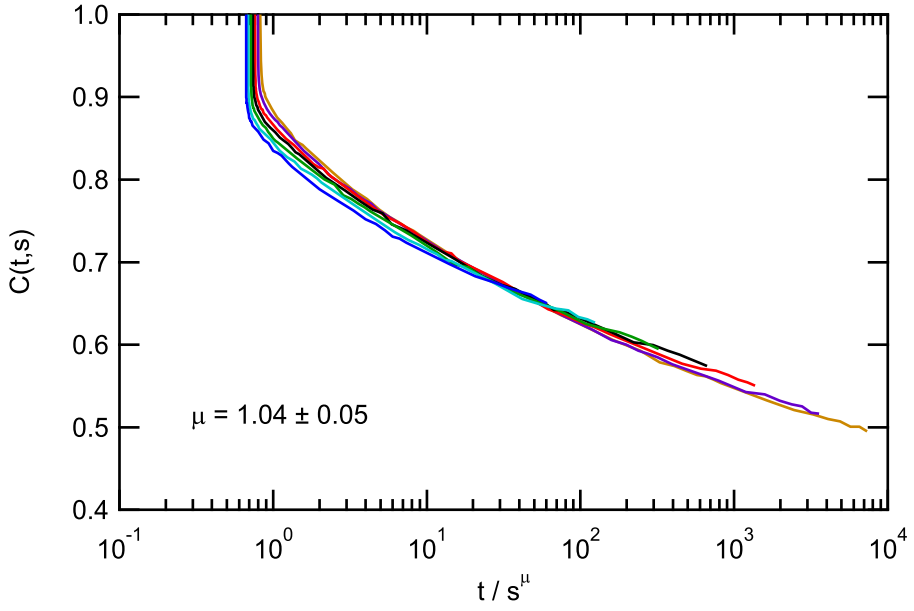

Figure 5.25: Subaging scaling plot for the two-dimensional Coulomb glass. $K = 0.40625$ and $T = 0.02$.

5.2.2 3D Coulomb Glass

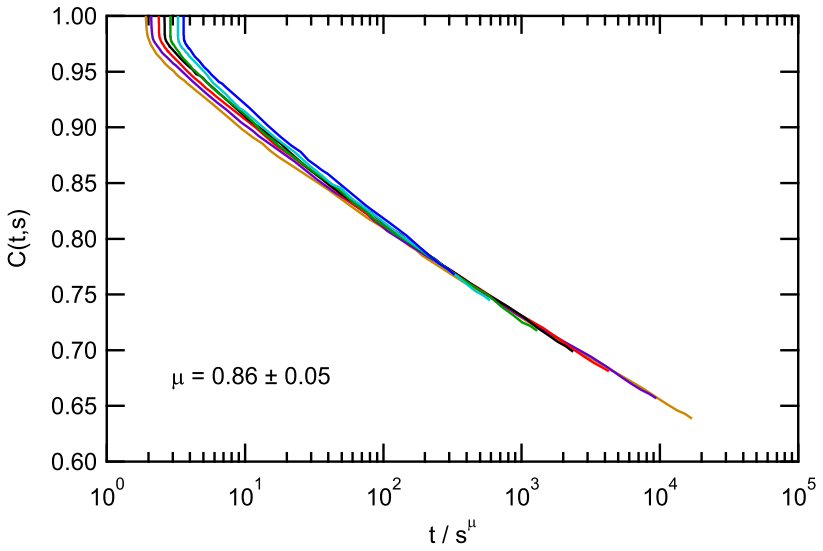

Figure 5.26: Subaging scaling plot for the three-dimensional Coulomb glass. $K = 0.5$ and $T = 0.01$.

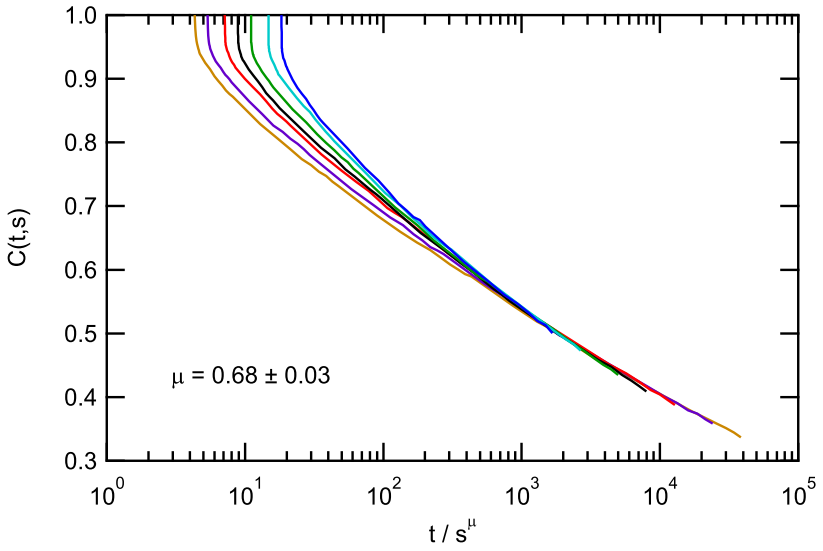

Figure 5.27: Subaging scaling plot for the three-dimensional Coulomb glass. $K = 0.5$ and $T = 0.02$.

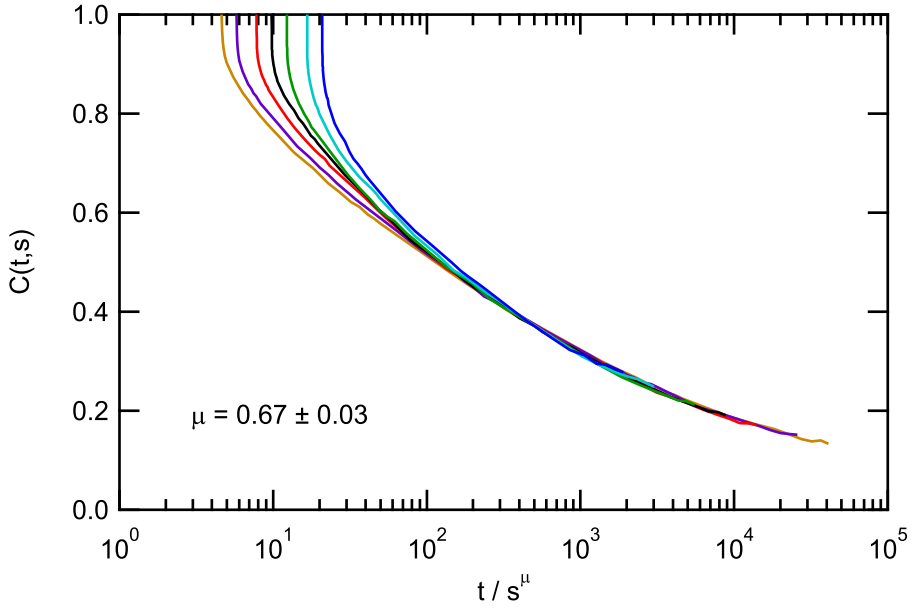

Figure 5.28: Subaging scaling plot for the three-dimensional Coulomb glass. $K = 0.5$ and $T = 0.03$.

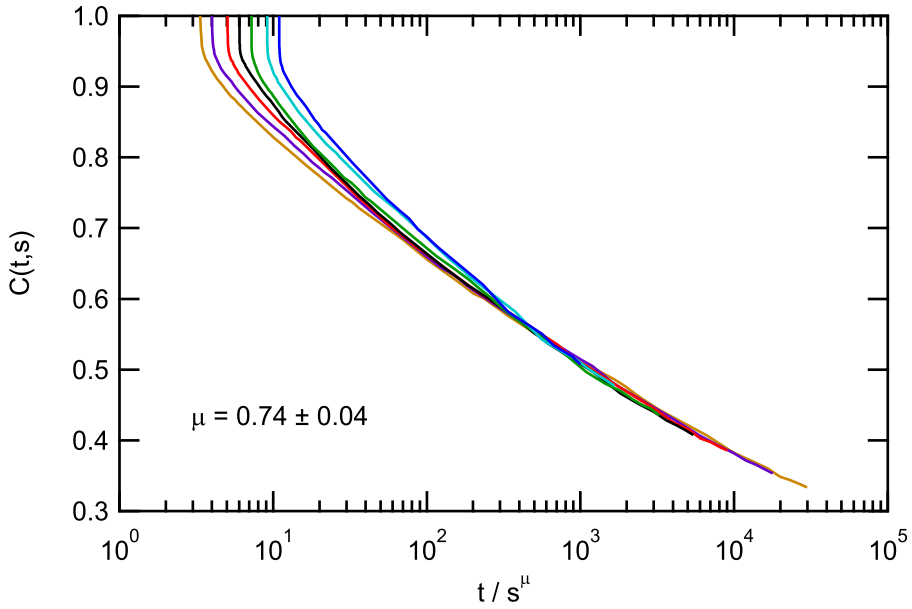

Figure 5.29: Subaging scaling plot for the three-dimensional Coulomb glass. $K = 0.46875$ and $T = 0.02$.

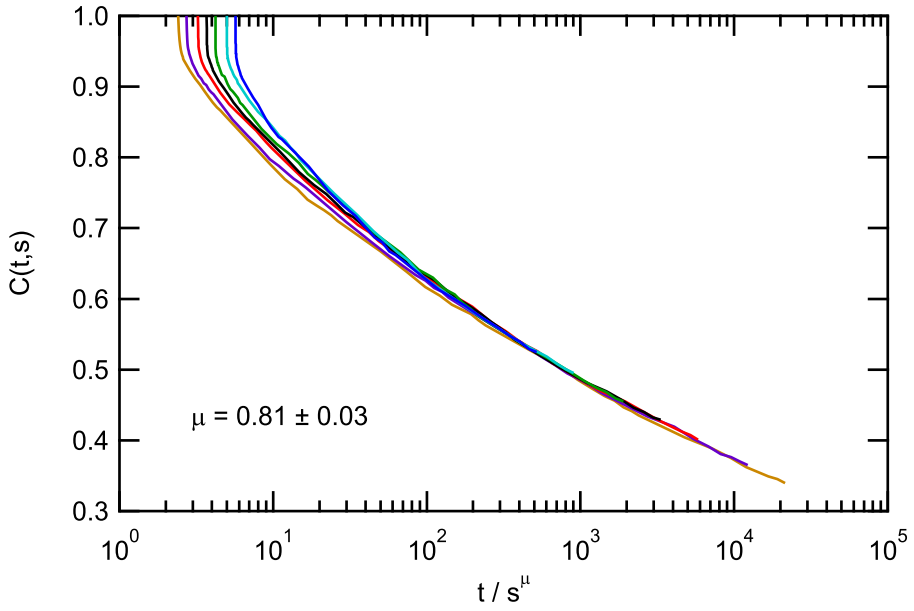

Figure 5.30: Subaging scaling plot for the three-dimensional Coulomb glass. $K = 0.4375$ and $T = 0.02$.

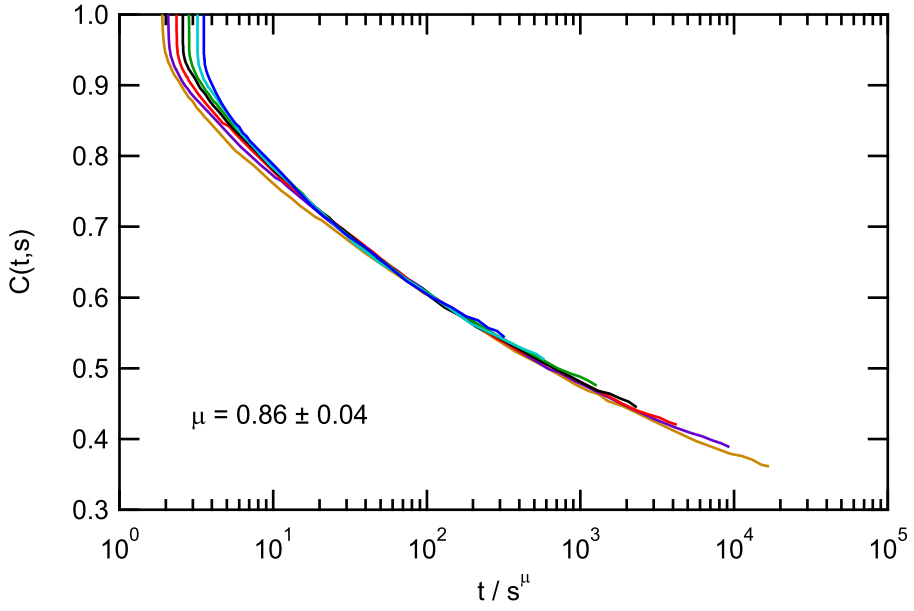

Figure 5.31: Subaging scaling plot for the three-dimensional Coulomb glass. $K = 0.40625$ and $T = 0.02$.

5.2.3 2D Bose Glass

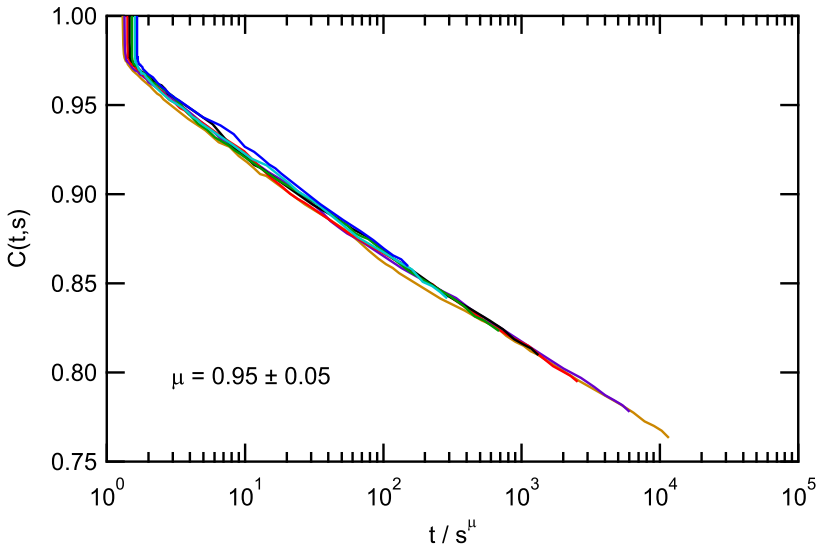

Figure 5.32: Subaging scaling plot for the Bose glass. $K = 0.5$ and $T = 0.01$.

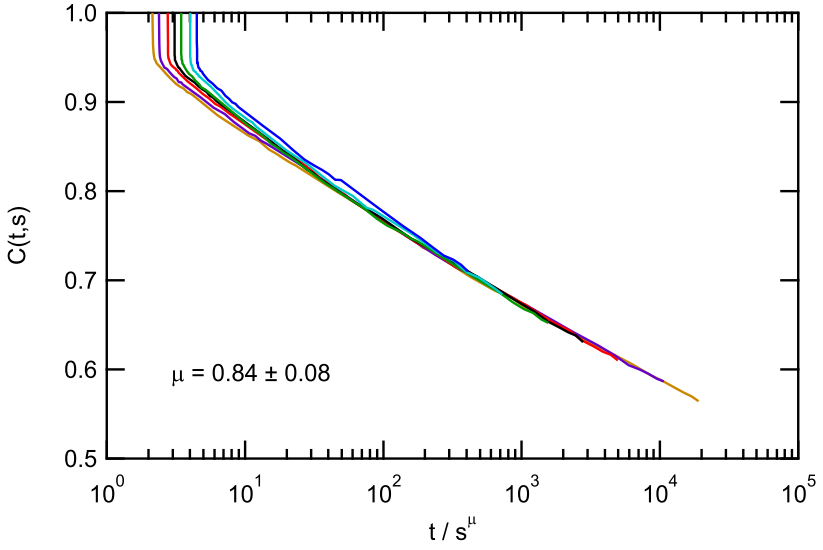

Figure 5.33: Subaging scaling plot for the Bose glass. $K = 0.5$ and $T = 0.02$.

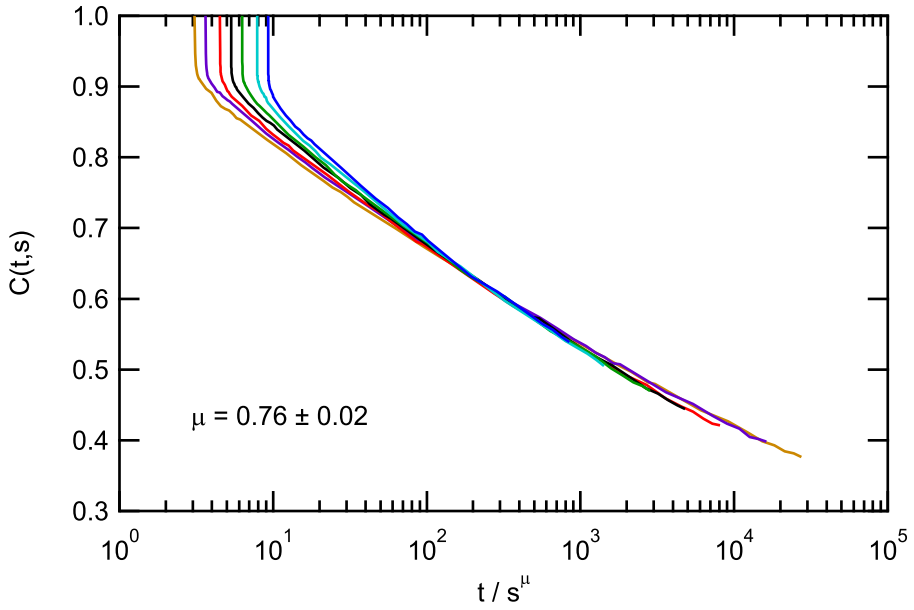

Figure 5.34: Subaging scaling plot for the Bose glass. $K = 0.5$ and $T = 0.03$.

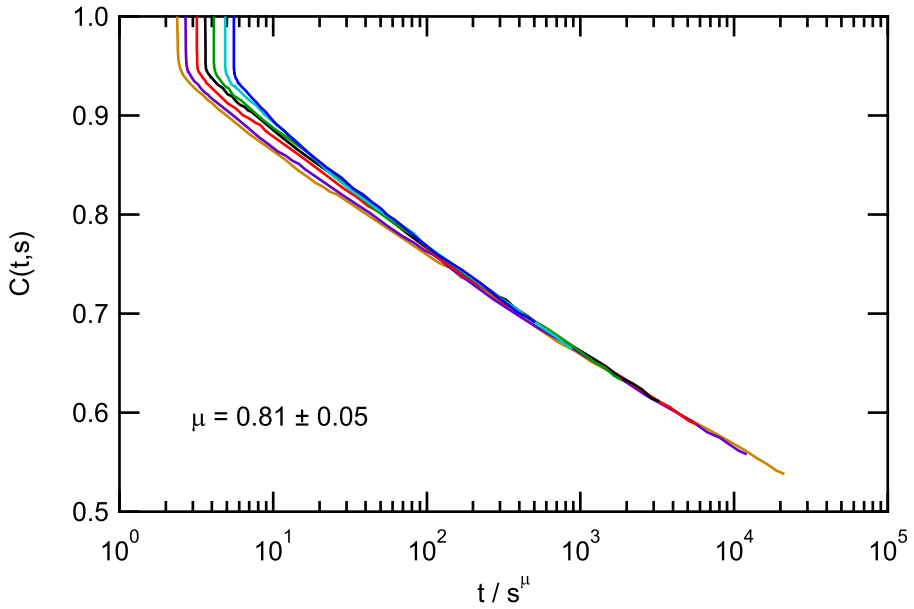

Figure 5.35: Subaging scaling plot for the Bose glass. $K = 0.46875$ and $T = 0.02$.

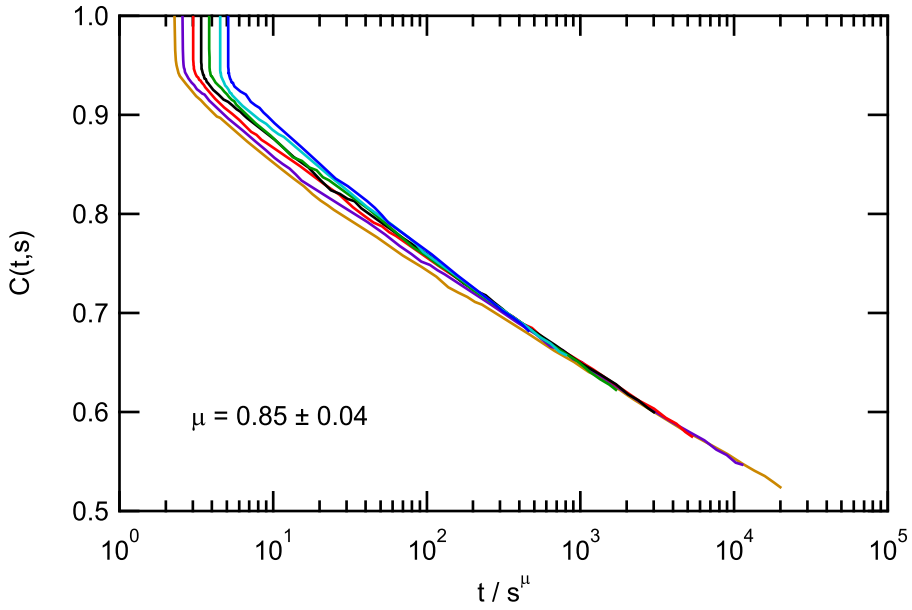

Figure 5.36: Subaging scaling plot for the Bose glass. $K = 0.4375$ and $T = 0.02$.

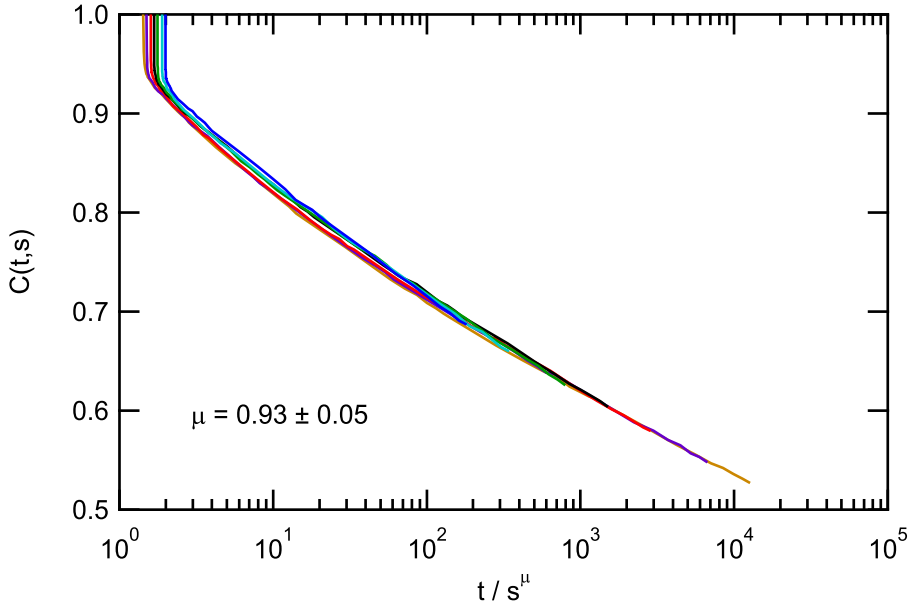

Figure 5.37: Subaging scaling plot for the Bose glass. $K = 0.40625$ and $T = 0.02$.

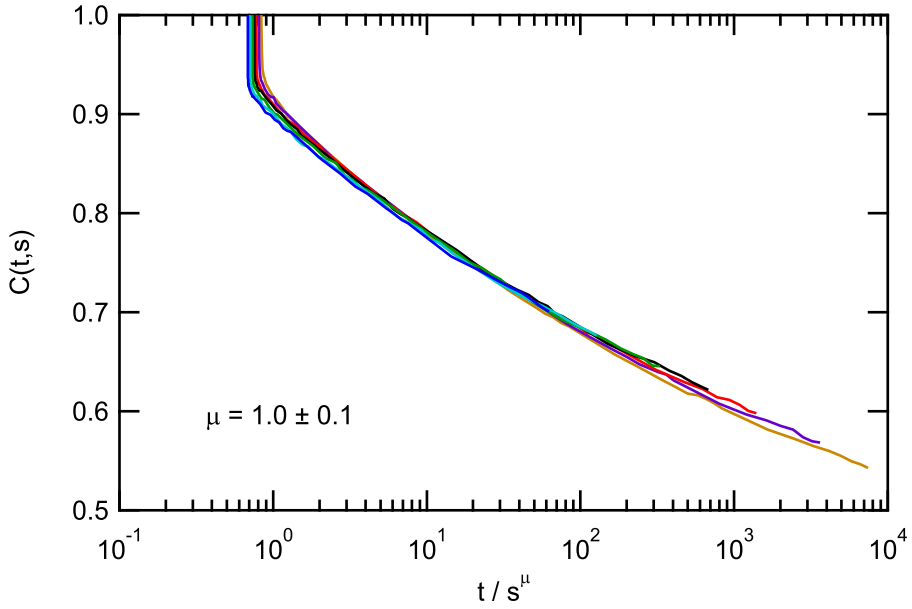

Figure 5.38: Subaging scaling plot for the Bose glass. $K = 0.375$ and $T = 0.02$.

5.2.4 Subaging Exponents

Figure 5.39 shows the values for μ that we obtained for various temperatures. As can be seen, all three models follow the same trend: as temperature increases, μ decreases. It is important to note that larger values of μ lead to slower relaxation. This means that, in our models, there is faster relaxation as temperature increases.

We also measured μ for different filling fractions (see Figure 5.40). The trend that occurs here is as the filling fraction approaches 0.5 (from either above or below), μ gets smaller. This leads to the conclusion that as the filling fraction approaches 0.5, the system undergoes faster relaxation.

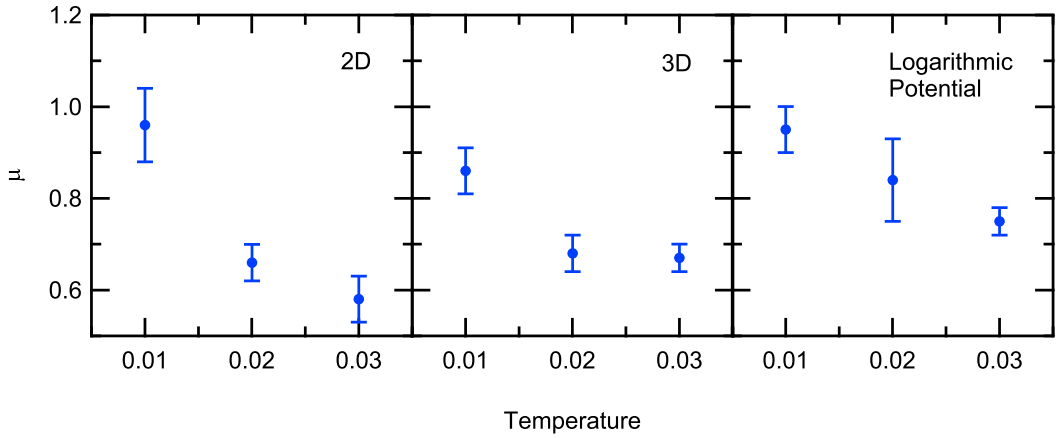

Figure 5.39: Values of subaging exponent μ for different temperatures in the 2D and 3D Coulomb potential as well as the logarithmic potential.

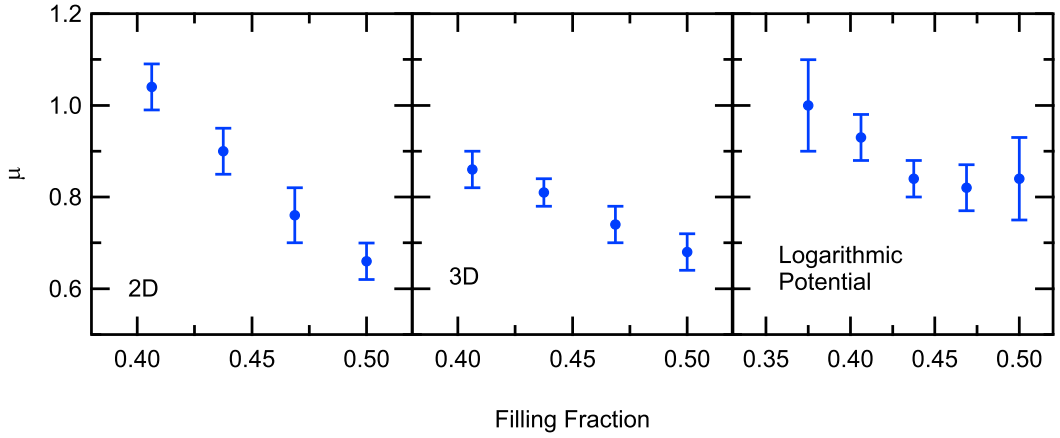

Figure 5.40: Values of subaging exponent μ for different filling fractions in the 2D and 3D Coulomb potential as well as the logarithmic potential.

5.3 Full-Aging Results

The full-aging scaling analysis detailed in §4.2.2 led to two scaling exponents: the full-aging exponent b given by

$$C(t,s) = s^{-b} f_C(t/s^{\mu}) \,, \tag{5.2}$$

(where $\mu = 1$) and the autocorrelation exponent λ_C/z given by

$$f_C(t/s) \sim (t/s)^{-\lambda_C/z} \,. \tag{5.3}$$

I will first display all of the full-aging scaling plots then I will discuss the values and trends on the full-aging exponents. All two-dimensional Coulomb glass plots will have a system size of $L = 16$ ($N = 256$), three-dimensional Coulomb glass will have a system size of $L = 8$ ($N = 512$), and the Bose glass will have a system size of $L = 24$ ($N = 576$). The other relevant system configurations will be provided in the captions.

5.3.1 2D Coulomb Glass

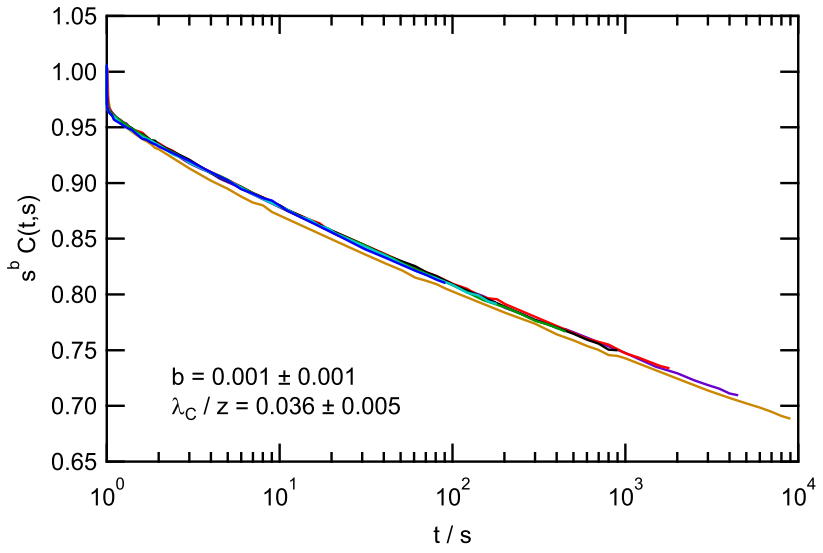

Figure 5.41: Full-aging scaling plot for the two-dimensional Coulomb glass. $K = 0.5$ and $T = 0.01$.

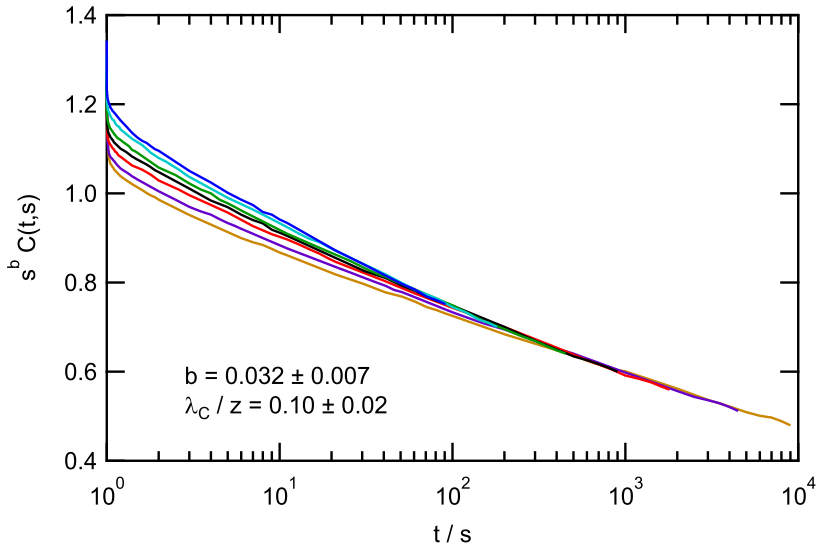

Figure 5.42: Full-aging scaling plot for the two-dimensional Coulomb glass. $K = 0.5$ and $T = 0.02$.

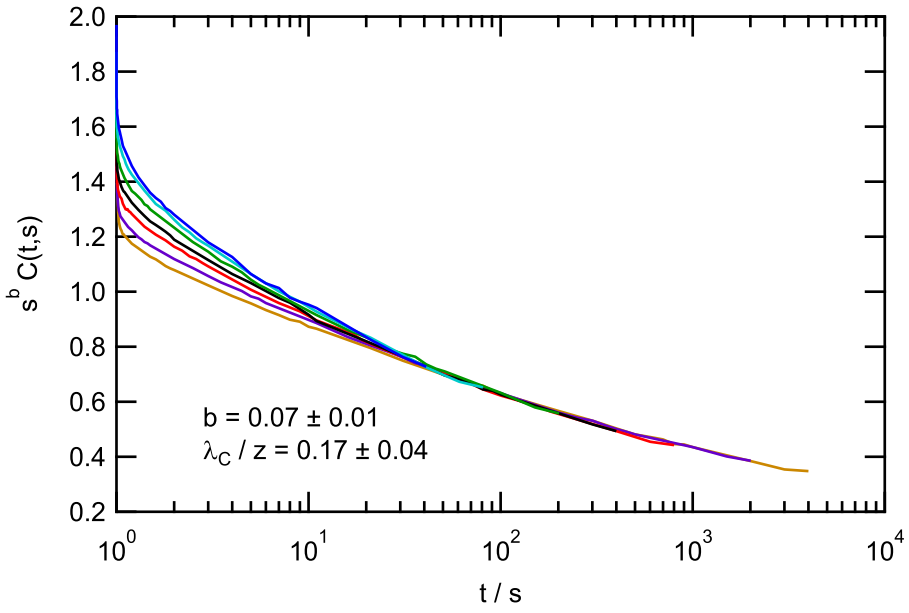

Figure 5.43: Full-aging scaling plot for the two-dimensional Coulomb glass. $K = 0.5$ and $T = 0.03$.

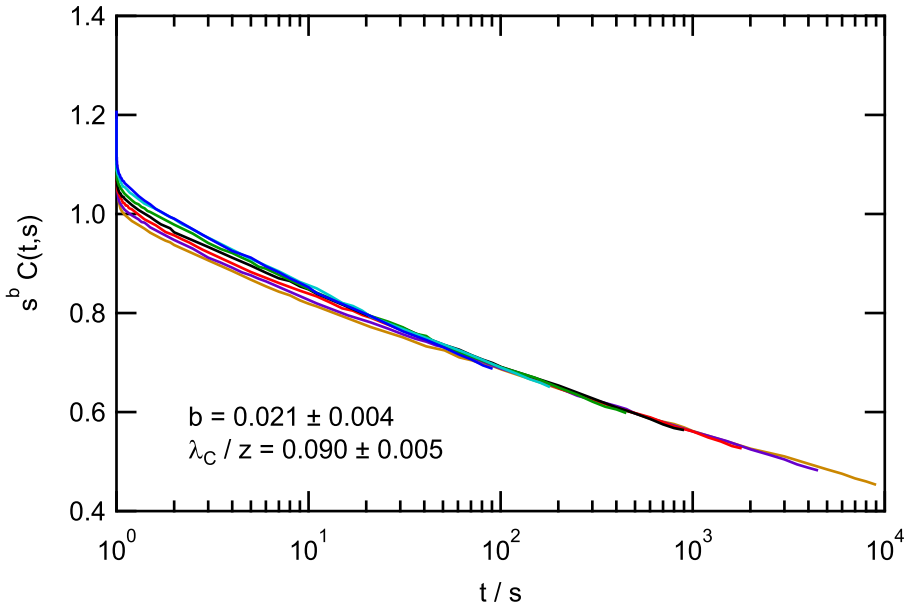

Figure 5.44: Full-aging scaling plot for the two-dimensional Coulomb glass. $K = 0.46875$ and $T = 0.02$.

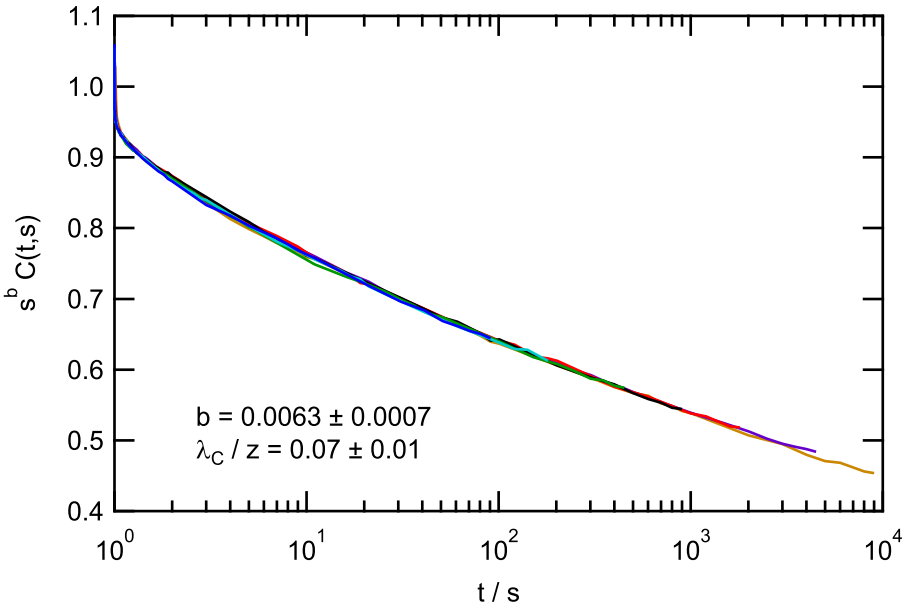

Figure 5.45: Full-aging scaling plot for the two-dimensional Coulomb glass. $K = 0.4375$ and $T = 0.02$.

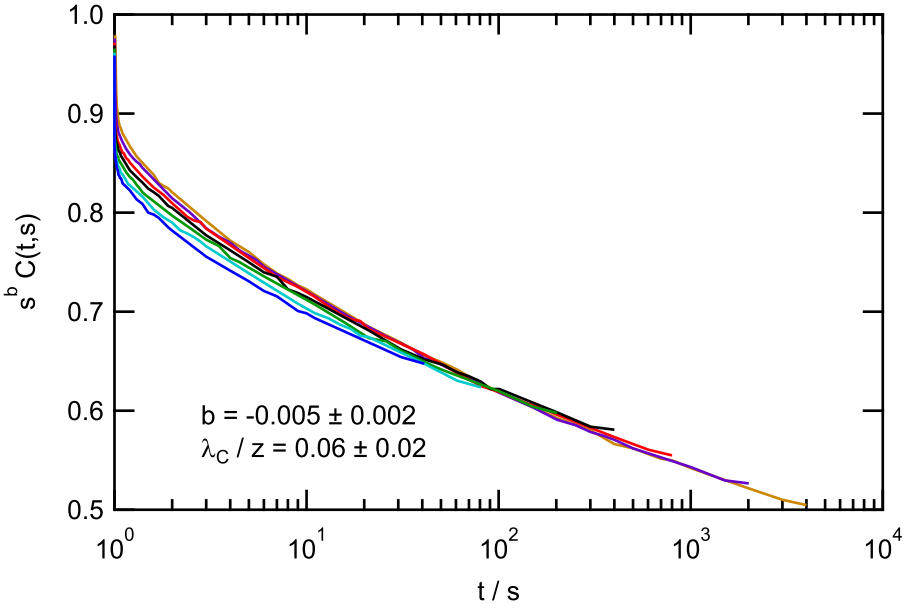

Figure 5.46: Full-aging scaling plot for the two-dimensional Coulomb glass. $K = 0.40625$ and $T = 0.02$.

5.3.2 3D Coulomb Glass

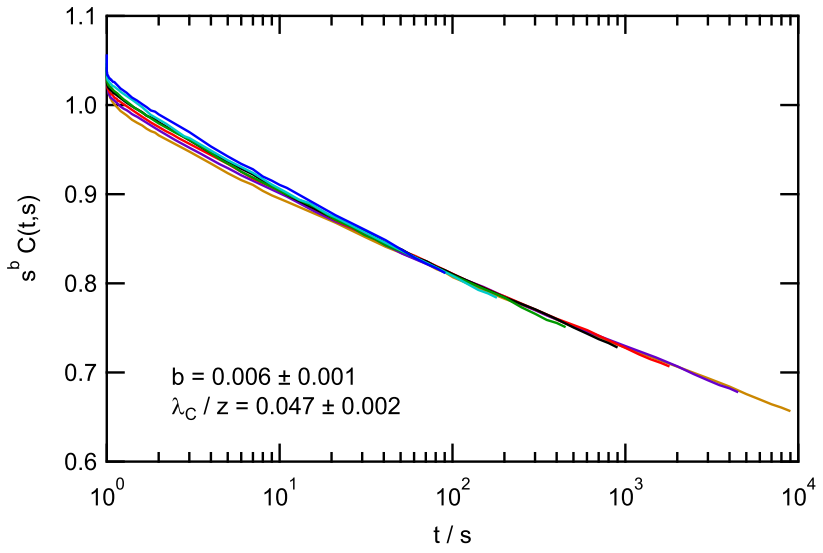

Figure 5.47: Full-aging scaling plot for the three-dimensional Coulomb glass. $K = 0.5$ and $T = 0.01$.

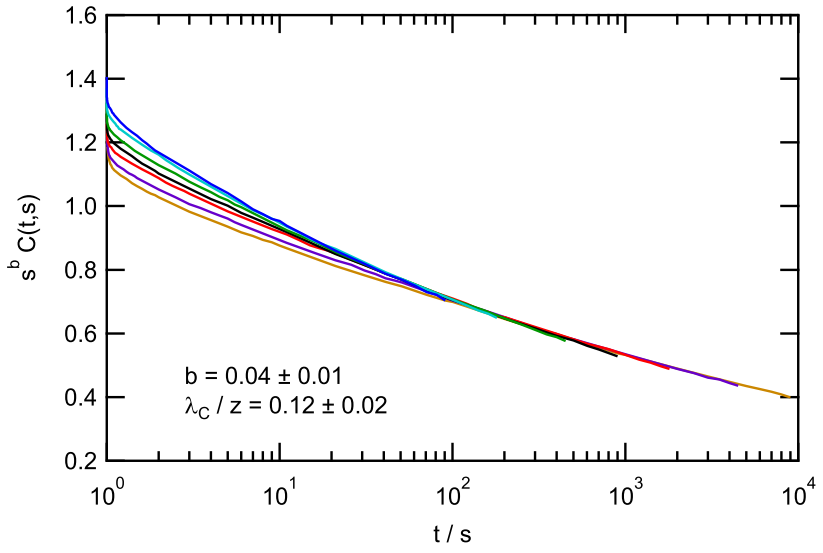

Figure 5.48: Full-aging scaling plot for the three-dimensional Coulomb glass. $K = 0.5$ and $T = 0.02$.

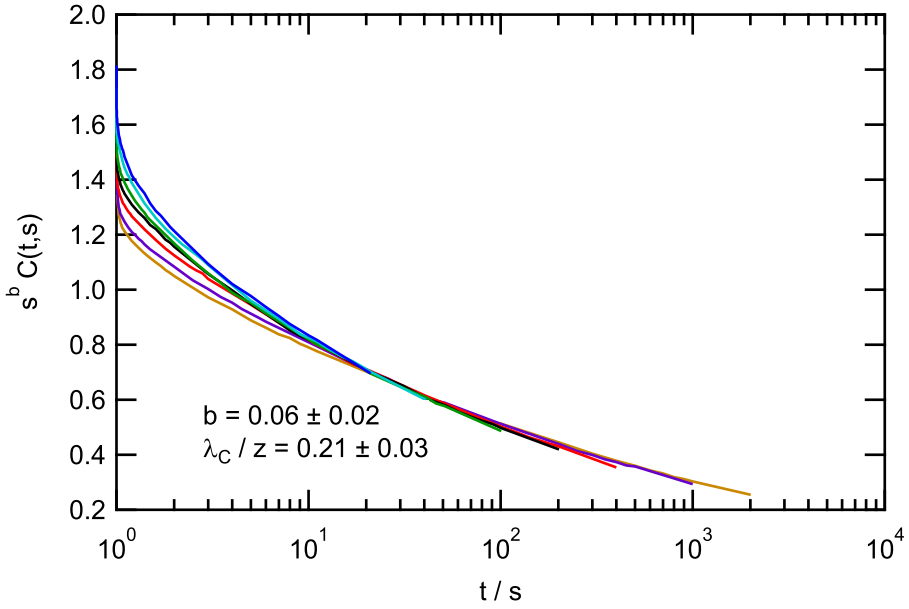

Figure 5.49: Full-aging scaling plot for the three-dimensional Coulomb glass. $K = 0.5$ and $T = 0.03$.

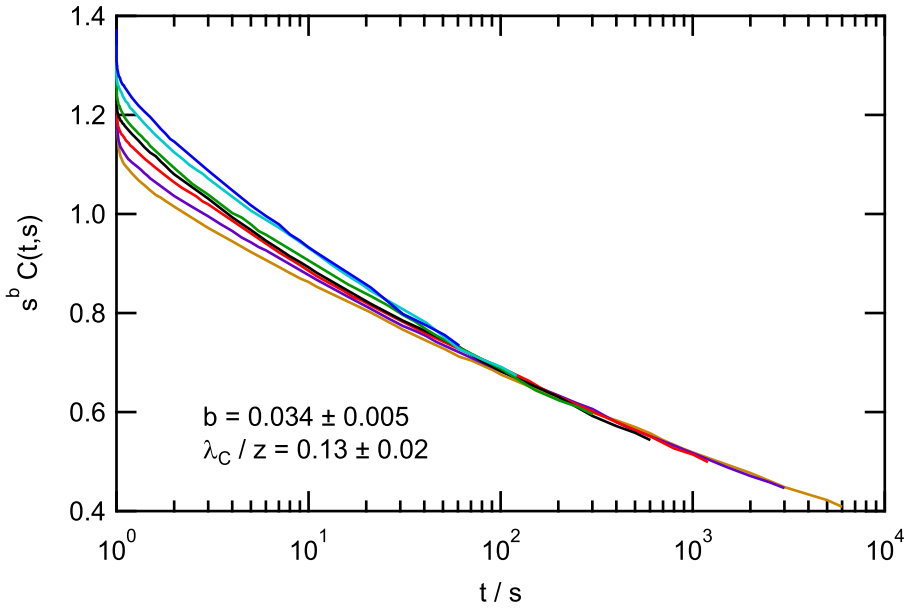

Figure 5.50: Full-aging scaling plot for the three-dimensional Coulomb glass. $K = 0.46875$ and $T = 0.02$.

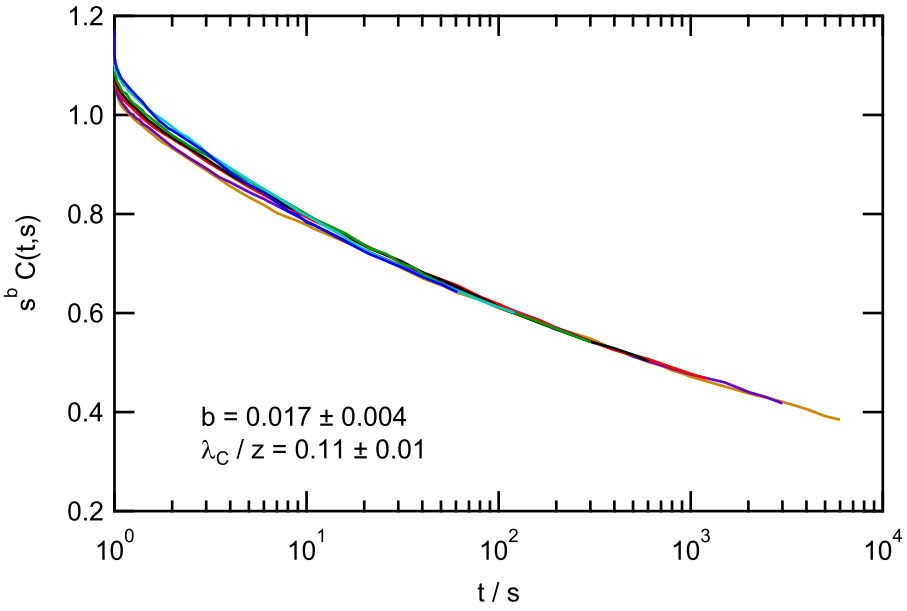

Figure 5.51: Full-aging scaling plot for the three-dimensional Coulomb glass. $K = 0.4375$ and $T = 0.02$.

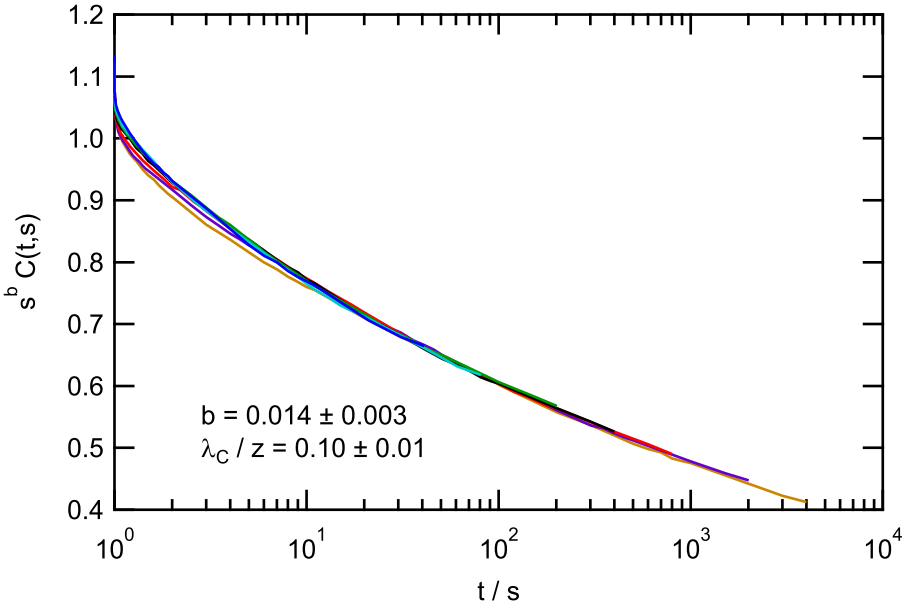

Figure 5.52: Full-aging scaling plot for the three-dimensional Coulomb glass. $K = 0.40625$ and $T = 0.02$.

5.3.3 2D Bose Glass

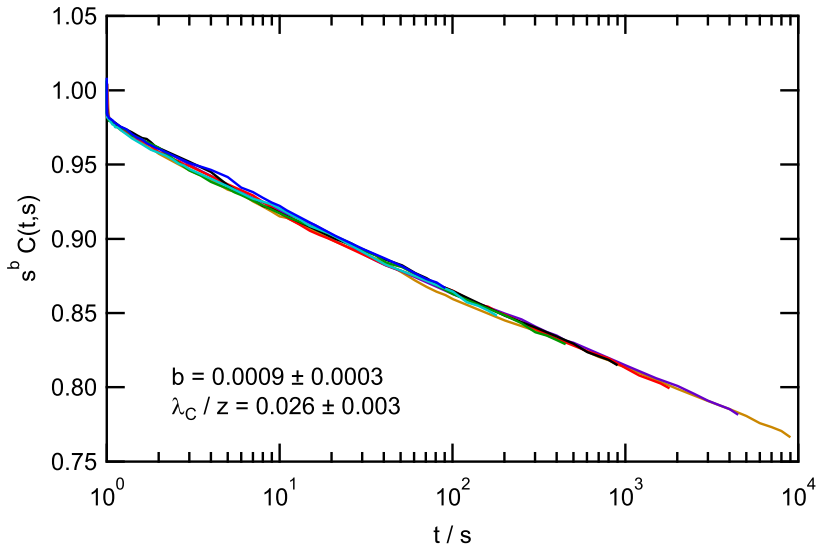

Figure 5.53: Full-aging scaling plot for the Bose glass. $K = 0.5$ and $T = 0.01$.

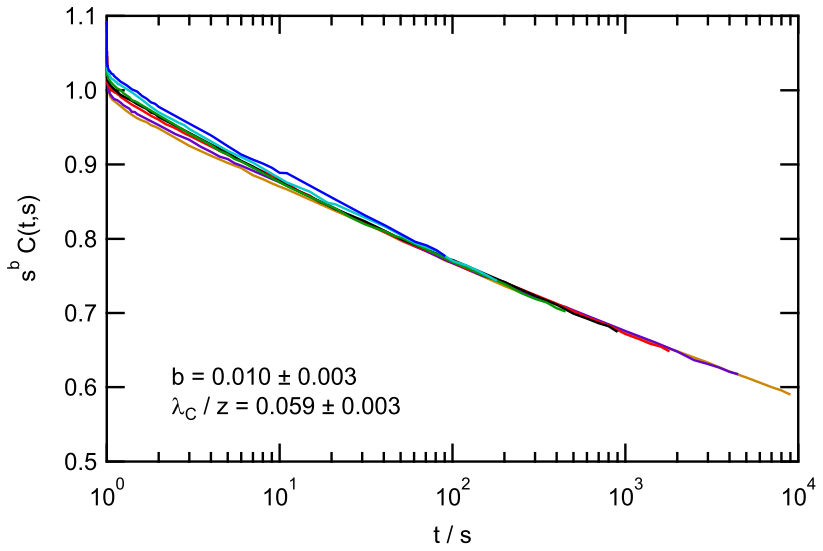

Figure 5.54: Full-aging scaling plot for the Bose glass. $K = 0.5$ and $T = 0.02$.

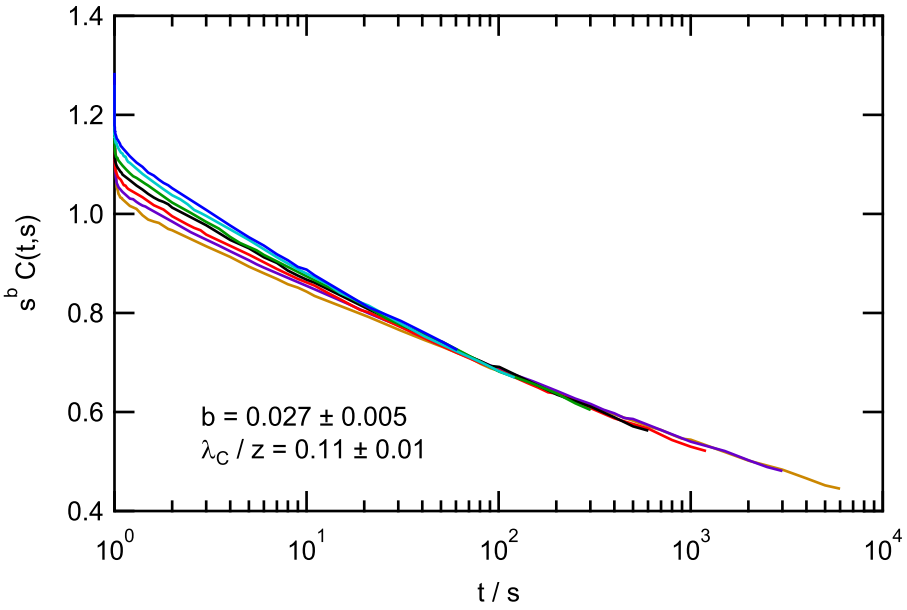

Figure 5.55: Full-aging scaling plot for the Bose glass. $K = 0.5$ and $T = 0.03$.

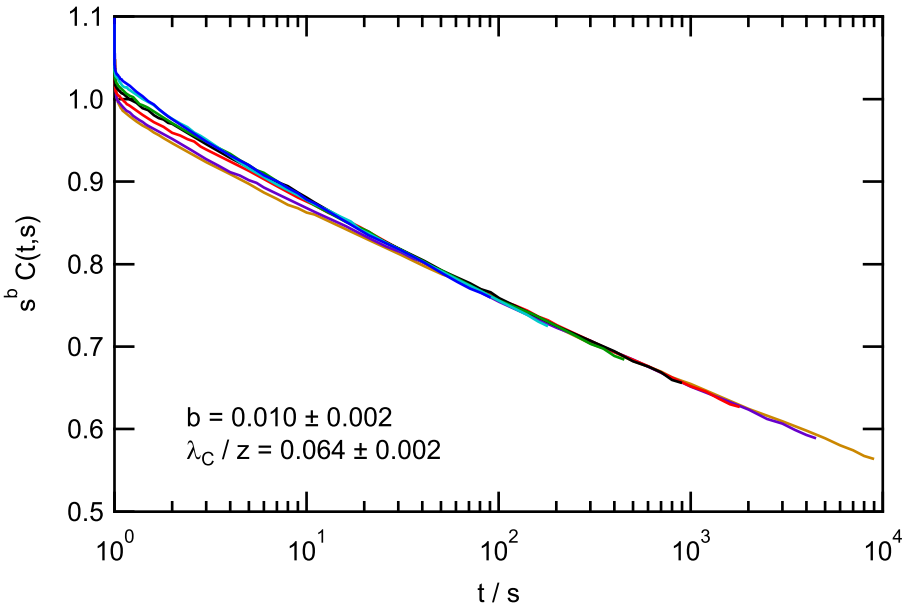

Figure 5.56: Full-aging scaling plot for the Bose glass. $K = 0.46875$ and $T = 0.02$.

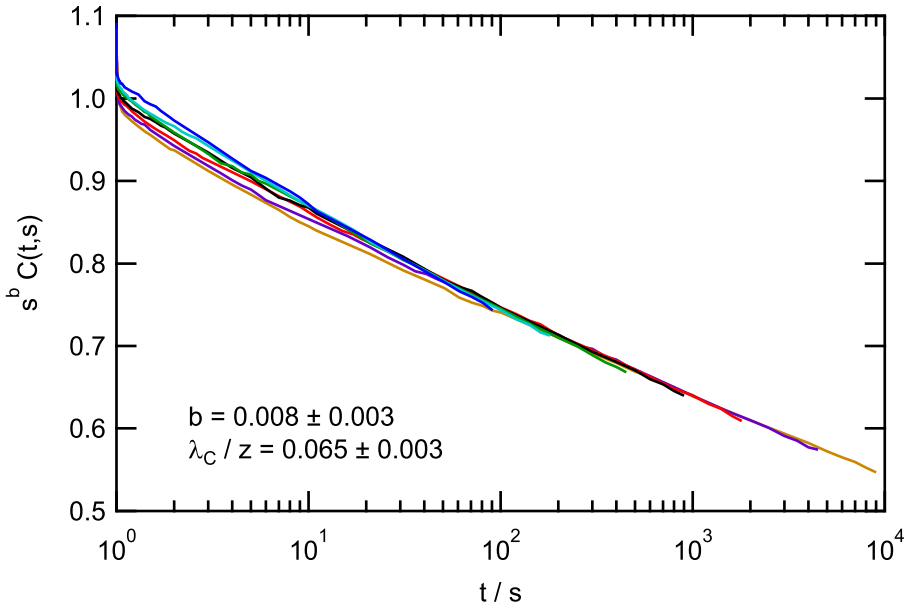

Figure 5.57: Full-aging scaling plot for the Bose glass. $K = 0.4375$ and $T = 0.02$.

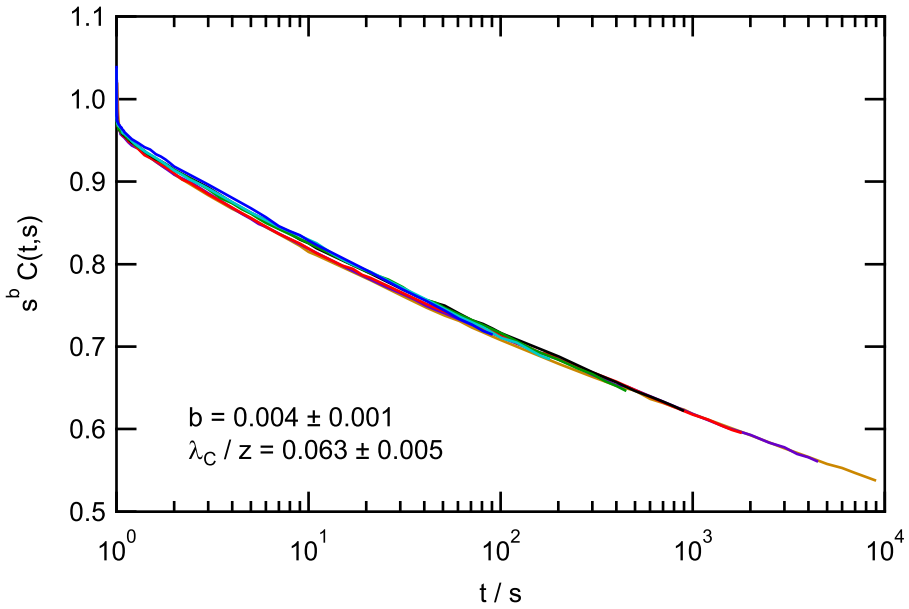

Figure 5.58: Full-aging scaling plot for the Bose glass. $K = 0.40625$ and $T = 0.02$.

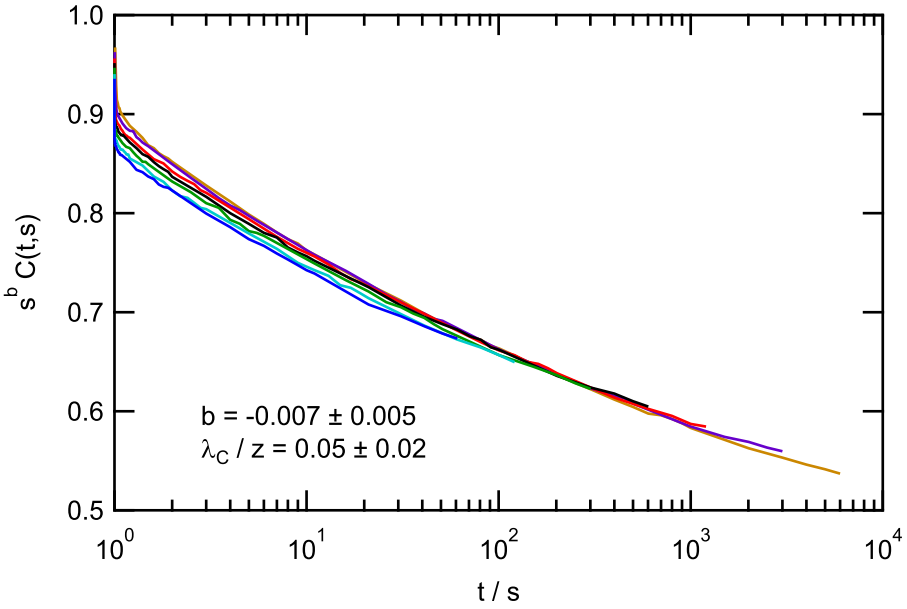

Figure 5.59: Full-aging scaling plot for the Bose glass. $K = 0.375$ and $T = 0.02$.

5.3.4 Full-Aging Exponents

The trend that these exponents follow is the opposite of μ, i.e: as b gets smaller, slower relaxation is observed. Figure 5.60 and Figure 5.61 show the values of b for various temperatures and filling fractions respectively. As expected, the trends show slower relaxation (smaller value of b) as temperature decreases. Slower relaxation is also observed as the filling fraction deviates away from 0.5.

The trends for the autocorrelation exponent λ_C/z are the same as the trends for b with one possible exception. Figure 5.62 shows the values of λ_C/z for various temperatures; and, as expected, we see slower relaxation at lower temperatures. The trends for various filling fractions (shown in Figure 5.63) are the same as b – namely, slower relaxation as filling fractions deviates away from 0.5 – with the possible exception in the case of the logarithmic

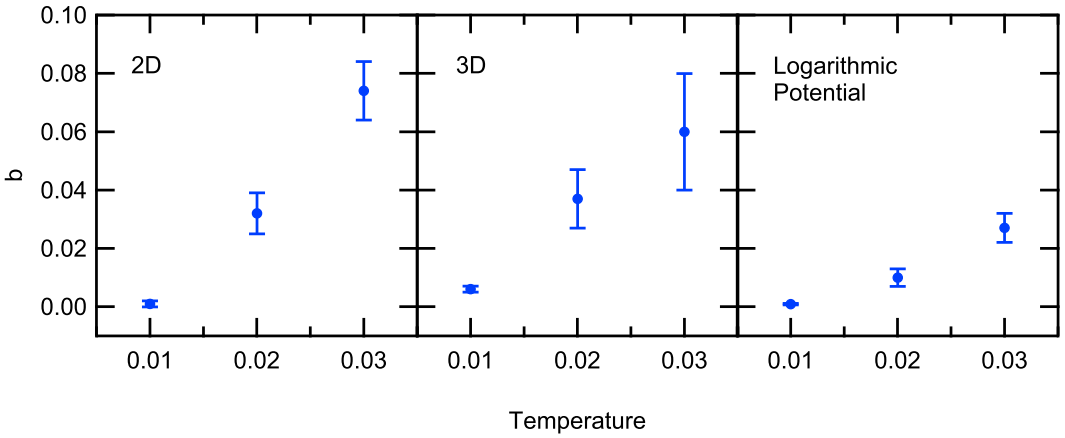

Figure 5.60: Values of full-aging exponent b for different temperatures in the 2D and 3D Coulomb potential as well as the logarithmic potential.

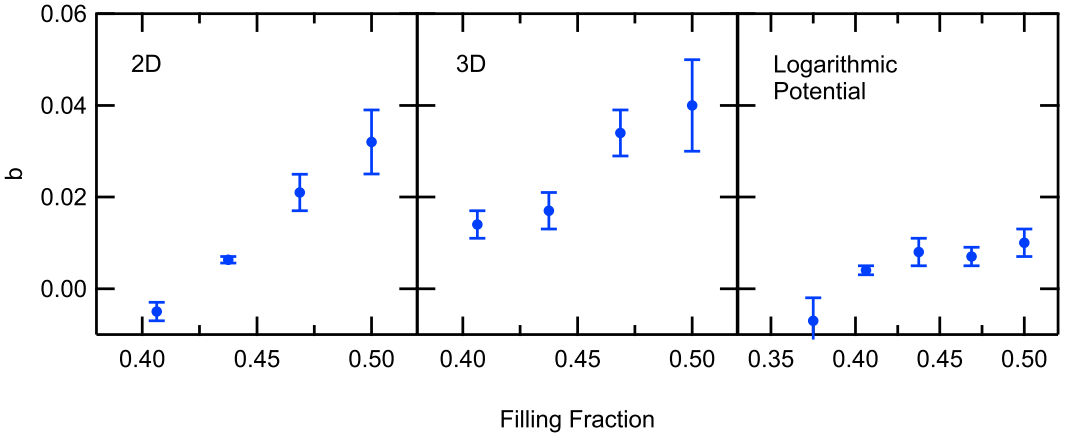

Figure 5.61: Values of full-aging exponent b for different filling fractions in the 2D and 3D Coulomb potential as well as the logarithmic potential.

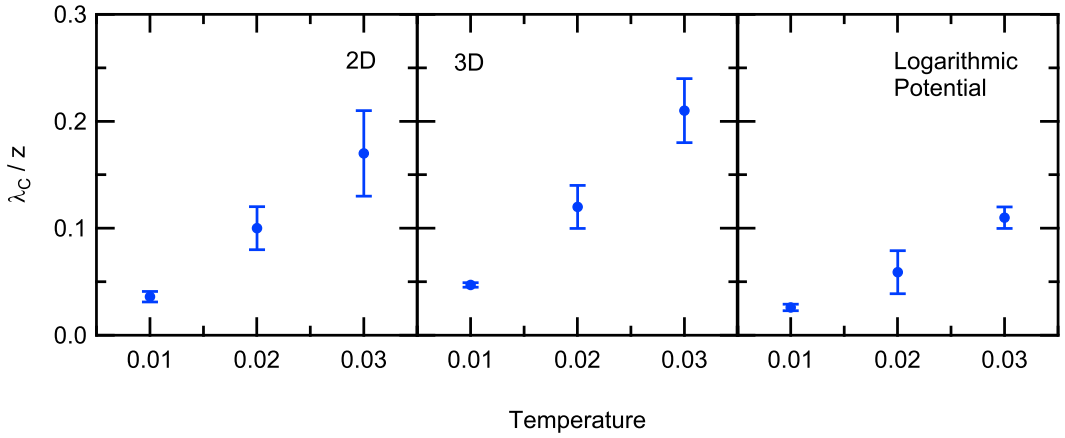

Figure 5.62: Values of autocorrelation exponent λ_C/z for different temperatures in the 2D and 3D Coulomb potential as well as the logarithmic potential.

potential. The same trend may apply; however, it cannot be determined.

5.4 Comparison of Scaling Methods

The first point that can be seen when comparing the scaling methods is that both show dependence on temperature and filling fraction. This means that the scaling exponents are not universal. As for temperature dependence, both methods tell the same story of slower relaxation with lower temperature (as expected). Likewise, for filling fraction dependence, both methods offer the same trend: slower relaxation as the filling fraction deviates away from 0.5. So, in essence, both scaling forms encapsulate the same physical trends. Thus, a subaging analysis is unnecessary and the system can be classified as a full-aging system.

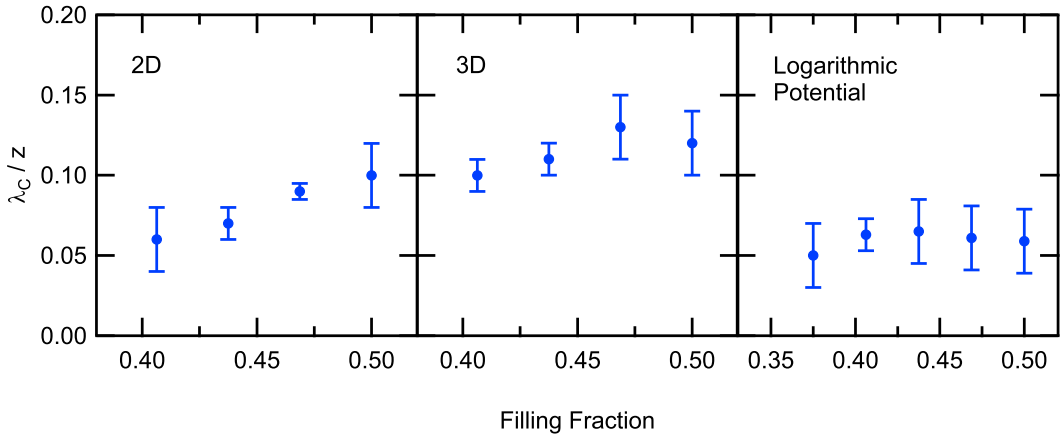

Figure 5.63: Values of autocorrelation exponent λ_C/z for different filling fractions in the 2D and 3D Coulomb potential as well as the logarithmic potential.

Chapter 6

Conclusion

By employing the Coulomb glass model (adapted to the Bose glass model via a logarithmic potential), we have investigated the density of states and nonequilibrium relaxation processes of the two- and three-dimensional Coulomb glass as well as the Bose glass via Monte Carlo simulations. Our particular model consisted of multiple localized pinning sites randomly located on a continuum occupied by a predetermined number of charge carriers. The interaction potential (either $1/r$ or the modified Bessel function), temperature, system size, and filling fraction were all varied in order to systematically measure the density of states and two-time carrier density autocorrelation function. This systematic approach allowed us to investigate the various scaling forms and whether or not the ensuing scaling exponents are universal. By varying the initial conditions of the systems in question, we also looked at how the physical properties of the systems altered the relaxation kinetics in the aging regime, which may lead to a method to characterize systems by distinguishing universal and

non-universal properties.

6.1 Results

When investigating the asymptotic behavior of the Coulomb gap, we found very little, if any dependence on temperature or filling fraction of the gap exponent. Our values disagreed with the mean field predictions; however, with the system sizes we employed, the power-law description of the density of states at least appeared to be a reasonable fit.

The speed of formation of the Coulomb gap appeared to have no dependence on temperature. In the three-dimensional model, the density of states underwent complete suppression, even at finite temperatures. This was not the case in two dimensions where the gap formation is much slower and our temperatures were probably too high for complete suppression to occur. However, in all cases, the gap formed remarkably fast (when compared to the very slow relaxation found by measuring the autocorrelation function).

A very broad gap was found in the density of states of the Bose glass system. The gap was also found to have very little dependence on temperature, probably due to the broadness and the temperatures not being large enough to have an impact. A power-law fit for the density of states seemed justifiable and led to comparatively large gap exponents which would suggest suppressed motion leading to very slow relaxation.

Through the measurement of the two-time carrier density autocorrelation function, we proposed two scaling forms – namely the subaging and full-aging scaling forms – to investigate

dynamical scaling and the aging phenomena of the systems. These scaling forms offered a total of three different scaling exponents to be measured. I detailed the polynomial interpolation method used in order to extract the values of these scaling exponents. This lead to a common trend: as either the temperature decreases or the filling fraction deviates more from half-filling, the exponents reflect slower relaxation kinetics. Thus, the scaling exponents are non-universal, as is the case for disordered magnetic systems [49].

When comparing the scaling forms, we found that both offer the same physical picture; thus, the inclusion of a subaging exponent $\mu \neq 1$ is unnecessary. The full-aging method encapsulates the same physical characteristics as the subaging method as well as being more firmly grounded on theoretical analysis. These results persist in both the Coulomb glass and the Bose glass systems.

6.2 Outlook

When comparing the interaction potentials ($1/r$ and the logarithmic potential), one sees that the logarithmic potential generally leads to slower relaxation. We did briefly explore $1/r^2$ as a means to describe the possible dependence on interaction potential for the scaling exponents; however, the system sizes required to produce the statistics necessary for comparison were simply too large. From the the data that we did gather, we found extremely slow relaxation in the $1/r^2$ potential case. Further investigation could lead to some very interesting dependence of the scaling exponents on the interaction potential. This could also lead to a better

understanding of the asymptotic behavior of the density of states. Different interaction potentials also lead to different gap widths allowing for an investigation in the relationship between gap width and the relaxation rates.

In an attempt to measure the time-dependence of the correlation length in the system, we looked at the spatial correlation function. What we found was that after just a few Monte Caro time steps, the spatial correlation function showed no measurable change. This needs to be explored more as the correlation length plays a very important role in the aging kinetics of the system. Looking at energy-energy correlations may prove useful in this pursuit. Also, the four-point autocorrelation function may provide useful results.

Given the computational power accessible to us, we were unable to probe low density systems. These configurations led to extremely slow relaxation as well as a plateau relaxation regime. It would be interesting to extend the run time of such systems to see if and when they relax out of this plateau regime. Do they still follow the same trends that the high density systems obey? These systems would likely need to be extended for a much longer simulation as well as a larger system size as finite size effects might play a larger role.

In an attempt to match the perturbations done in experiments [5, 6], we attempted to remove or add charge carriers into the system in addition to the temperature quench. The first issue that we had to solve with this is exactly how this was to be done. We attempted two ways: the first was to just remove/add in charge carriers randomly; the second method was by biasing the location of the removed/added charge carriers (take only from the left half of the simulation cell as an example). There was little difference in these two methods except

for very early times; however, further study would be needed to confirm this. The other issue was how exactly to measure the conductivity in the system. We tried to apply an electric field and then measure the current in the system; however, this proved very difficult. The system was very sensitive to the strength of the electric field and either produced no measurable current (as if the electric field was not even there) or a current so large that it had no dependence on temperature or filling fraction (the electric field dominated). A more thorough scan of the configuration space may lead to an appropriate "window" of values for the electric field. This is something that certainly needs to be explored further to better link our simulations with experimental data.

Bibliography

[1] Henkel, M. and Pleimling, M. *Nonequilibrium Phase Transitions, Volume 2: Ageing and Dynamical Scaling Far From Equilibrium.* Springer, New York, (2010).

[2] Efros, A. L. and Pollak, M. *Electron–Electron Interactions in Disordered Systems.* North-Holland, Amsterdam, (1985).

[3] Efros, A. L. and Shklovskii, B. I. *Journal of Physics C: Solid State Physics* **8**(4), L49 (1975).

[4] Shklovskii, B. I. and Efros, A. L. *Electronic Properties of Doped Semiconductors.* Springer, New York, (1984).

[5] Jaroszyński, J. and Popović, D. *Phys. Rev. Lett.* **99**(4), 046405 Jul (2007).

[6] Jaroszyński, J. and Popović, D. *Phys. Rev. Lett.* **99**(21), 216401 Nov (2007).

[7] Davies, J. H., Lee, P. A., and Rice, T. M. *Phys. Rev. Lett.* **49**(10), 758–761 Sep (1982).

[8] Grünewald, M., Pohlmann, B., Schweitzer, L., and Würtz, D. *Journal of Physics C: Solid State Physics* **15**(32), L1153 (1982).

[9] Xue, W. and Lee, P. A. *Phys. Rev. B* **38**(13), 9093–9098 Nov (1988).

[10] Möbius, A., Richter, M., and Drittler, B. *Phys. Rev. B* **45**(20), 11568–11579 May (1992).

[11] Grannan, E. R. and Yu, C. C. *Phys. Rev. Lett.* **71**(20), 3335–3338 Nov (1993).

[12] Menashe, D., Biham, O., Laikhtman, B. D., and Efros, A. L. *Phys. Rev. B* **64**(11), 115209 Aug (2001).

[13] Menashe, D., Biham, O., Laikhtman, B. D., and Efros, A. L. *EPL (Europhysics Letters)* **52**(1), 94 (2000).

[14] Surer, B., Katzgraber, H. G., Zimanyi, G. T., Allgood, B. A., and Blatter, G. *Phys. Rev. Lett.* **102**(6), 067205 Feb (2009).

[15] Pérez-Garrido, A., Ortuño, M., Díaz-Sánchez, A., and Cuevas, E. *Phys. Rev. B* **59**(8), 5328–5332 Feb (1999).

[16] Yu, C. C. *Phys. Rev. Lett.* **82**(20), 4074–4077 May (1999).

[17] Díaz-Sánchez, A. and Pérez-Garrido, A. *Eur. Phys. J. B* **24**, 483 (2001).

[18] Tsigankov, D. N., Pazy, E., Laikhtman, B. D., and Efros, A. L. *Phys. Rev. B* **68**(18), 184205 Nov (2003).

[19] Grempel, D. R. *EPL (Europhysics Letters)* **66**(6), 854 (2004).

[20] Kolton, A. B., Grempel, D. R., and Domínguez, D. *Phys. Rev. B* **71**(2), 024206 Jan (2005).

[21] Amir, A., Oreg, Y., and Imry, Y. *Phys. Rev. Lett.* **103**(12), 126403 Sep (2009).

[22] Amir, A., Oreg, Y., and Imry, Y. *Phys. Rev. B* **77**(16), 165207 Apr (2008).

[23] Amir, A., Oreg, Y., and Imry, Y. *Annu. Rev. Condens. Matter Phys.* **2**, 235–62 (2011).

[24] Amir, A., Oreg, Y., and Imry, Y. *Phys. Rev. B* **80**, 245214 (2009).

[25] Mott, N. *Proc. Camb. Phil. Soc.* **32**, 281 (1949).

[26] Mott, N. *Proc. Phys. Soc.* **A62**, 416 (1956).

[27] Anderson, P. *Phys. Rev.* **109**, 1492 (1958).

[28] Nelson, D. R. and Vinokur, V. M. *Phys. Rev. B* **48**(17), 13060–13097 Nov (1993).

[29] Nelson, D. R. and Vinokur, V. M. *Phys. Rev. Lett* **68**, 2398 (1992).

[30] Täuber, U. C., Dai, H., Nelson, D. R., and Lieber, C. M. *Phys. Rev. Lett.* **74**(25), 5132–5135 Jun (1995).

[31] Täuber, U. C. and Nelson, D. R. *Phys. Rev. B* **52**(22), 16106–16124 Dec (1995).

[32] Du, X., Li, G., Greenblatt, M., and Shuk, P. *Nature* **3**, 111 (2007).

[33] Pollak, M. *J. Non-Cryst Solids* **11**(1), 1 (1972).

[34] Butko, V. Y., DiTusa, J. F., and Adams, P. W. *Phys. Rev. Lett.* **84**(7), 1543 Feb (2000).

[35] Massey, J. G. and Lee, M. *Phys. Rev. Lett.* **75**(23), 4266–4269 Dec (1995).

[36] Struik, L. C. E. *Physical aging in amorphous polymers and other materials.* Elsevier, Amsterdam, (1978).

[37] Götze, W. and Sjogren, L. *Reports on Progress in Physics* **55**(3), 241 (1992).

[38] Debenedetti, P. G. and Stillinger, F. H. *Nature* **410**, 259 (2001).

[39] Godrèche, C. and Luck, J. M. *Journal of Physics A: Mathematical and General* **33**(6), 1151 (2000).

[40] Lippiello, E. and Zannetti, M. *Phys. Rev. E* **61**(4), 3369–3374 Apr (2000).

[41] Janssen, H. K., Schaub, B., and Schmittmann, B. *Z. Phys. B* **73**, 539 (1989).

[42] Calabrese, P. and Gambassi, A. *Journal of Physics A: Mathematical and General* **38**(18), R133 (2005).

[43] Coniglio, A. and Zannetti, M. *Phys. Rev. B* **42**(10), 6873–6876 Oct (1990).

[44] Biroli, G. *Journal of Statistical Mechanics: Theory and Experiment* **2005**(05), P05014 (2005).

[45] Cannas, S. A., Stariolo, D. A., and Tamarit, F. A. *Physica A* **294**(3-4), 362 (2001).

[46] Baumann, F., Dutta, S. B., and Henkel, M. *Journal of Physics A: Mathematical and Theoretical* **40**(27), 7389 (2007).

[47] Dutta, S. B. *Journal of Physics A: Mathematical and Theoretical* **41**(39), 395002 (2008).

[48] Bhattacharjee, S. M. and Seno, F. *Journal of Physics A: Mathematical and General* **34**(33), 6375 (2001).

[49] Henkel, M. and Pleimling, M. *Phys. Rev. B* **78**(22), 224419 Dec (2008).